

MODELING AND PROCESS OPTIMIZATION OF WATER JET GUIDED
LASER MICRO HOLE DRILLING ON NICKEL-BASED AEROSPACE
ALLOYS

A THESIS SUBMITTED TO
THE GRADUATE SCHOOL OF NATURAL AND APPLIED SCIENCES
OF
MIDDLE EAST TECHNICAL UNIVERSITY

BY
LEVENT SUBAŞI

IN PARTIAL FULFILLMENT OF THE REQUIREMENTS
FOR
THE DEGREE OF DOCTOR OF PHILOSOPHY
IN
MECHANICAL ENGINEERING

SEPTEMBER 2022

Approval of the thesis:

**MODELING AND PROCESS OPTIMIZATION OF WATER JET GUIDED
LASER MICRO HOLE DRILLING ON NICKEL-BASED AEROSPACE
ALLOYS**

submitted by **LEVENT SUBAŞI** in partial fulfillment of the requirements for the degree of **Doctor of Philosophy** in **Mechanical Engineering**, **Middle East Technical University** by,

Prof. Dr. Halil Kalıpçılar
Dean, Graduate School of **Natural and Applied Sciences**

Prof. Dr. M. A. Sahir Arıkan
Head of the Department, **Mechanical Engineering**

Prof. Dr. Mustafa İlhan Gökler
Supervisor, **Mechanical Engineering, METU**

Assoc. Prof. Dr. Ulaş Yaman
Co-Supervisor, **Mechanical Engineering, METU**

Examining Committee Members:

Prof. Dr. Melik Dölen
Mechanical Engineering, METU

Prof. Dr. Mustafa İlhan Gökler
Mechanical Engineering, METU

Prof. Dr. Gözde Bozdağı Akar
Electrical and Electronic Engineering, METU

Prof. Dr. Can Çoğun
Mechatronics Engineering, Cankaya University

Prof. Dr. Oğuzhan Yılmaz
Mechanical Engineering, Gazi University

Date: 09.09.2022

I hereby declare that all information in this document has been obtained and presented in accordance with academic rules and ethical conduct. I also declare that, as required by these rules and conduct, I have fully cited and referenced all material and results that are not original to this work.

Name Last name : Levent Subaşı

Signature :

ABSTRACT

MODELING AND PROCESS OPTIMIZATION OF WATER JET GUIDED LASER MICRO HOLE DRILLING ON NICKEL-BASED AEROSPACE ALLOYS

Subaşı, Levent

Doctor of Philosophy, Mechanical Engineering

Supervisor : Prof. Dr. Mustafa İlhan Gökler

Co-Supervisor: Assoc. Prof. Dr. Ulaş Yaman

September 2022, 196 pages

Special aerospace alloys are used for the manufacturing of turbine blades in gas turbines and micro cooling holes are drilled on them to increase their thermal resistance. Water Jet Guided Laser (WJGL) is a novel technology that can be used to drill these holes. WJGL process overcomes the adverse effects of conventional laser drilling, but the physics of this process is very complex. Determining the proper machining parameters to achieve acceptable process time and quality is worth to be studied. In this study, the material removal mechanism of this process has been investigated, and process time and quality optimization studies have been realized. A simplified and holistic model has been developed based on statistical analysis, machine learning, and experimental studies for drilling nickel-based aerospace alloys, such as Inconel 625, Inconel 718, and CMSX-4. Additionally, real-time process monitoring solutions have been obtained. For these purposes, image processing by using a mono camera and acoustic sensing by using an optical microphone have been realized in order to measure the effective cutting length, the laser power in water, and machining conditions. The effects of hole geometries on

machining efficiency have been studied and some recommendations are proposed as well.

Keywords: Water jet Guided Laser, Micro Hole Drilling, Artificial Neural Network, Image Processing, Acoustic Sensing

ÖZ

SU JETİ KILAVUZLU LAZER MİKRO DELİK DELME İŞLEMİNİN NİKEL ESASLI HAVACILIK ALAŞIMLARI İÇİN MODELLENMESİ VE OPTİMİZASYONU

Subaşı, Levent
Doktora, Makina Mühendisliği
Tez Yöneticisi: Prof. Dr. Mustafa İlhan Gökler
Ortak Tez Yöneticisi: Doç. Dr. Ulaş Yaman

Eylül 2022, 196 sayfa

Gaz türbinlerinde kullanılan türbin kanatlarının imalatında özel havacılık alaşımları kullanılmakta ve ısı dirençlerini arttırmak için üzerlerine mikro soğutma delikleri açılmaktadır. Su jeti kılavuzlu lazer, bu delikleri delmek için kullanılabilecek yeni bir teknolojidir. Söz konusu işlem, geleneksel lazer delmenin olumsuz etkilerinin üstesinden gelmektedir, fakat işlemin fiziği çok karmaşıktır. Kabul edilebilir işlem süresi ve kalite sonuçları elde etmek için uygun işleme parametrelerinin belirlenmesi, üzerinde çalışılmaya değer bir konudur. Bu çalışmada, su jeti kılavuzlu lazer işleminin malzeme kaldırma mekanizması araştırılmış, işlem süresi ve kalite optimizasyonu çalışmaları gerçekleştirilmiştir. Inconel 625, Inconel 718 ve CMSX-4 gibi nikel bazlı havacılık alaşımlarının delinmesi için istatistiksel analiz, makine öğrenimi ve deneysel çalışmalara dayalı olarak basitleştirilmiş ve bütünsel bir model geliştirilmiştir. Ayrıca gerçek zamanlı süreç izleme çözümleri elde edilmiştir. Bu amaçlarla etkin kesme uzunluğunu, sudaki lazer gücünü ve işleme koşullarını ölçmek için mono kamera ile görüntü işleme ve optik mikrofon ile akustik algılama

gerçekleştirilmiştir. Delik geometrilerinin işleme verimliliği üzerindeki etkileri incelenmiş ve bazı öneriler sunulmuştur.

Anahtar Kelimeler: Su Jeti Kılavuzlu Lazer, Mikro Delik Delme, Yapay Sinir Ağı, Görüntü İşleme, Akustik Algılama

Dedicated to my family

ACKNOWLEDGMENTS

I would like to express my deepest gratitude to my supervisor Prof. Dr. Mustafa İlhan Gökler and co-supervisor Assoc. Prof. Dr. Ulaş Yaman for their guidance, advice, criticism, encouragements and insight throughout the research. They have spent valuable time to help me develop the study, and definitely, this thesis would not be possible without their support.

I would also like to thank Prof. Dr. Melik Dölen and Prof. Dr. Gözde Bozdağı Akar for their suggestions and comments throughout the assessment period. Their approach and criticism kept me on track and encouraged me to stay focused on the details.

I am grateful for the technical assistance of colleagues from TEI and SYNOVA SA. My discussions with them led to new ideas that I could not have thought of on my own.

The journey of a PhD study is not only technical, but psychological as well. I would like to thank to my family for their psychological support at hard times. I am grateful for their patience.

This work is supported by The Scientific and Technological Research Council of Turkey (TÜBİTAK) Directorate of Science Fellowships and Grant Programmes (BİDEB) 2211-A [grant number 1649B031804554].

TABLE OF CONTENTS

ABSTRACT.....	v
ÖZ	vii
ACKNOWLEDGMENTS	x
TABLE OF CONTENTS.....	xi
LIST OF TABLES	xvi
LIST OF FIGURES	xviii
LIST OF ABBREVIATIONS	xxiii
LIST OF SYMBOLS	xxv
CHAPTERS	
1 INTRODUCTION	1
1.1 Motivation and Scope of the Study.....	2
1.2 Organization of the Thesis	3
2 WATER JET GUIDED LASER TECHNOLOGY.....	5
2.1 Machine Controller	6
2.2 Water Jet System.....	7
2.3 Laser System.....	7
2.4 Process Window for Machine Parameters	9
2.5 Effective Cutting Length.....	11
2.6 Drilling Strategy.....	12

3	LITERATURE SURVEY ON LASER BEAM MACHINING AND WATER JET GUIDED LASER DRILLING	15
3.1	Studies on Conventional Dry Laser Drilling	15
3.1.1	Modeling Studies	16
3.1.2	Experimental Studies	21
3.2	Studies on WJGL Drilling	27
4	MATERIAL REMOVAL MECHANISM OF LASER BEAM MACHINING AND WATER JET GUIDED LASER PROCESS	31
4.1	Conventional Laser Material Removal Mechanism	31
4.1.1	What is Laser?	31
4.1.2	How is a Laser Beam Formed?	33
4.1.3	Laser Pulse Generation	35
4.1.4	Laser-Material Interaction – Absorption	36
4.1.5	Laser-Material Interaction – Reflectivity	39
4.1.6	Laser Power Density	41
4.1.7	Material Removal Model	42
4.1.8	Vaporization Mechanism	43
4.1.9	Plasma Effect	44
4.1.10	Energy Balance	46
4.1.11	Effect of Auxiliary Gas	47
4.1.12	Quality Issues	48
4.1.13	Summary	50
4.2	Water Jet Guided Laser Material Removal Mechanism	51
4.2.1	WJGL Laser Properties	52

4.2.2	Water Jet Properties	53
4.2.3	Effect of Gas	61
4.2.4	Laser-Water Jet Coupling	63
4.2.5	Laser Propagation in the Water Jet.....	67
4.2.6	Raman Scattering	68
4.2.7	Laser Power Attenuation in the Water Jet	69
4.2.8	Laser Breakup	71
4.2.9	WJGL Material Interaction	75
4.2.10	WJGL Quality Review	79
4.2.11	WJGL Machining Efficiency	80
4.2.12	Summary	82
4.3	Closure	83
5	WATER JET GUIDED LASER PARAMETERS AND EXPERIMENTAL DETERMINATION OF THEIR EFFECTS ON PROCESS TIME AND QUALITY	85
5.1	Experimental Studies on WJGL Process Time and Quality	86
5.2	Instruments used in Experimental Studies	97
6	GENERAL STRUCTURE OF PROCESS MODELING OF WATER JET GUIDED LASER.....	99
6.1	General Structure of Process Modeling of Water Jet Guided Laser	100
6.2	Modeling for Prediction of the Laser Power, the Pulse Width, the Effective Cutting Length, and the Laser Power in the Water Jet.....	102
6.2.1	Data Collection for Prediction of the Laser Power, the Pulse Width, the Effective Cutting Length, and the Laser Power in the Water Jet.....	103

6.2.2	Artificial Neural Network Method for Prediction of the Laser Power, the Pulse Width, and the Effective Cutting Length	104
6.2.3	Statistical Analyses for Prediction of the Laser Power, the Pulse Width, the Effective Cutting Length, and the Laser Power in the Water Jet	107
6.3	Laser Ablation Mechanism for WJGL	111
6.4	Experiments for Determining the Process Efficiency	114
6.5	Prediction of Material Removal Using the Developed Model	127
6.6	Closure.....	128
7	EXPERIMENTAL STUDIES FOR REAL-TIME MEASUREMENT OF THE LASER BEAM CHARACTERISTICS	129
7.1	Measurement Methods for Measuring the Laser Beam Characteristics	130
7.1.1	Image sensor – Setup and Application	132
7.1.2	Acoustic Sensor – Setup and Application	132
7.2	Experiments for Measuring the Laser Beam Characteristics	137
7.2.1	Image Processing.....	138
7.2.2	Acoustic Analysis.....	141
7.3	Closure.....	148
8	INVESTIGATION OF EFFECTS OF THE HOLE GEOMETRY ON MACHINING BEHAVIOUR	151
8.1	Optical Microphone.....	152
8.2	Details of the Experiments and Measurements	154
8.2.1	Drilling Experiments	154
8.2.2	Acoustic Measurements.....	156
8.3	Results of the Drilling Experiments	158
8.3.1	Process Limits	158

8.3.2	Drilling Efficiency	160
8.3.3	Hole Morphology	162
8.3.4	Acoustic Analysis	164
8.4	Closure	171
9	CONCLUSIONS AND FUTURE WORK	173
9.1	Conclusions	173
9.2	Main Contributions of the Study	175
9.3	Future Work	175
	REFERENCES	177
	APPENDICES	
A.	Nominal Compositions of the Alloys	189
B.	Python Code for Image Processing	191
	CURRICULUM VITAE	195

LIST OF TABLES

Table 2.1 Machine Parameters.....	9
Table 3.1 Significant Factor Effects on Quality Characteristics [44]	25
Table 4.1 Laser Parameters.....	53
Table 5.1 Factors and Levels	87
Table 5.2 Modified Taguchi L-16 Orthogonal Table	87
Table 5.3 Results of the Experiments	89
Table 5.4 Main (Average) Effects of Factors for Process Time in Terms of <i>SNR</i> ..	91
Table 5.5 Main (Average) Effects of Factors for Taper Angle in Terms of <i>SNR</i> ...	91
Table 5.6 Overall Evaluation Criterion (<i>OEC</i>) Description	92
Table 5.7 <i>OEC</i> Scores.....	92
Table 5.8 Main (Average) Effects of Factors for <i>OEC</i> in Terms of <i>SNR</i>	93
Table 5.9 ANOVA Analysis	93
Table 5.10 Estimation of Performance for the Optimal Condition.....	94
Table 5.11 Confirming Predicted Results.....	95
Table 5.12 Types of Measurement Instruments and Their Use	97
Table 6.1 Input Levels for Measuring the Laser Parameters (Power & Pulse Width)	103
Table 6.2 Input Levels for Measuring the Effective Cutting Length.....	103
Table 6.3 Selected Hyper-parameters for the ANN Models.....	107
Table 6.4 Material Properties.....	112
Table 6.5 Factors and Levels for the Experiments	115
Table 6.6 Modified Taguchi L-27 Orthogonal Table	116
Table 6.7 Factor Effects – H: High Effect, M: Medium Effect, L: Low Effect ...	119
Table 6.8 Factors and Levels for the Experiment	121
Table 6.9 Trial Conditions for the Experiment.....	122
Table 6.10 Factor Effects – H: High Effect, M: Medium Effect, L: Low Effect .	122

Table 6.11 Change of Factors in order to Increase the <i>MRR</i> , <i>MRP</i> , and Efficiency	123
Table 7.1 Design of experiment	137
Table 7.2 ANOVA table for the average image brightness	139
Table 7.3 ANOVA table for the average sound amplitude between 200-600 (kHz)	143
Table 8.1 Design of experiment	155
Table 8.2 List of parameters and their values	156
Table 8.3 Coefficients of Equation (8.1) for different hole diameter values	161
Table 8.4 Calculated efficiency values based on the acoustic analysis for several hole diameters and number of cycles	171
Table A.1 Nominal Compositions of the Alloys	189
Table B.1 Python code for image processing.....	191

LIST OF FIGURES

Figure 2.1. Working Principle of WJGL	5
Figure 2.2. Machine Block Diagram	6
Figure 2.3. Schematic Representation of the Laser System	8
Figure 2.4. Example for 10 (kHz) frequency and 300 (ns) pulse width	9
Figure 2.5. Design Space for the Laser Parameters.....	11
Figure 2.6. Effective Cutting Length.....	12
Figure 2.7. Spiral Toolpath.....	13
Figure 3.1. Laser Hole Drilling Methods [7].....	16
Figure 3.2. The Distribution of Thermal Stress After Five Pulses [20]	20
Figure 3.3. <i>Back-Wall Damage</i> Problem.....	26
Figure 3.4. Representation of the Surfaces after (a) EDM (b) LMJ Drilling [69]..	27
Figure 3.5. Schematic of Droplet Assisted Laser Micromachining Setup [86].....	30
Figure 4.1. Propagation of light [89]	32
Figure 4.2. Comparison of ordinary light and laser beam	33
Figure 4.3. Inside a laser device [90].....	34
Figure 4.4. Change in photon population [91].....	36
Figure 4.5. Laser beam interaction on the material surface [90]	36
Figure 4.6. Different effects of laser beam absorption on the surface [90]	37
Figure 4.7. Laser-material interaction [100].....	39
Figure 4.8. Reflectivity as a function of wavelength for several metals [93].....	40
Figure 4.9. Different laser-material interaction regimes [90].....	41
Figure 4.10. Classification of laser assisted fabrication [90]	42
Figure 4.11. Material removal [92]	43
Figure 4.12. Effect of a single pulse [93]	45
Figure 4.13. Critical density vs radiation wavelength [95]	46
Figure 4.14. Recast and HAZ	49
Figure 4.15. Working principle of WJGL	51

Figure 4.16. <i>Vena contracta</i> effect [109]	54
Figure 4.17. Formation of the hydraulic flip [105]	56
Figure 4.18. Different flow conditions [105]	57
Figure 4.19. Stable jet length vs Pressure [108].....	57
Figure 4.20. Jet breakup length [103]	58
Figure 4.21. Jet breakup length vs Mean jet velocity [111].....	59
Figure 4.22. Gas-water jet interface [105]	61
Figure 4.23. Jet surrounded by helium stream [113]	62
Figure 4.24. Depth vs Stand-off distance [113]	63
Figure 4.25. Laser-water jet coupling [111]	63
Figure 4.26. Optical absorption spectrum of water [106]	64
Figure 4.27. Water jet acceptance angle for the laser beam [115].....	65
Figure 4.28. Nozzle damage [114].....	66
Figure 4.29. Misalignment problem [109]	66
Figure 4.30. The relation of coupling offset error and coupling efficiency [116] .	67
Figure 4.31. Laser beam profile in the water jet [112, 117].....	68
Figure 4.32. Spontaneous Raman Scattering [118].....	69
Figure 4.33. Stimulated Raman Scattering [118].....	69
Figure 4.34. Red color shift [4]	70
Figure 4.35. Energy vs Length [116]	70
Figure 4.36. Transmission vs Peak intensity [4]	71
Figure 4.37. Laser breakup [119].....	72
Figure 4.38. Raman scattering in the water jet [109].....	72
Figure 4.39. Shadowgraph images of the water jet [109]	73
Figure 4.40. Jet diameter vs jet abscissa [109].....	73
Figure 4.41. Breakup point [111].....	74
Figure 4.42. Angle of the scattered beam [111].....	75
Figure 4.43. Impingement of the water jet [105]	76
Figure 4.44. Ablation process [105].....	77
Figure 4.45. Continuous alteration of heating and cooling [105]	78

Figure 4.46. Water jet & laser interaction on the surface [68]	78
Figure 4.47. Water splashing direction [121]	80
Figure 4.48. The process drowns after certain depth [114]	82
Figure 5.1. Cause and Effect Fish-Bone Diagram of WJGL Process.....	85
Figure 5.2. Drilled Specimen.....	88
Figure 5.3. Response Plots for Process Time	90
Figure 5.4. Response Plots for Taper Angle.....	90
Figure 5.5. Peak Intensity vs. Process Time	96
Figure 6.1. General flowchart of WJGL process modeling.....	101
Figure 6.2. General process modeling methodologies	102
Figure 6.3. An Example of a Feed Forward Network	105
Figure 6.4. Examples of Good Fit and Overfitted Models on the Same Data.....	106
Figure 6.5. How the Early Stop Command Works.....	106
Figure 6.6. Response Plot for Power	108
Figure 6.7. Response Plot for Pulse Width.....	108
Figure 6.8. Response Plot for Effective Cutting Length	109
Figure 6.9. Power Variation Plot.....	110
Figure 6.10. Thermally Penetrated Volume from a Laser Pulse	113
Figure 6.11. a) The setup, b) An instance from machining	117
Figure 6.12. a) Inconel 625, b) CMSX-4.....	118
Figure 6.13. Plots of Efficiency.....	119
Figure 6.14. Plots of Laser Factors vs. Efficiency.....	123
Figure 6.15. MRP_{th}/V_{th} vs. MRP	124
Figure 6.16. Measured Efficiency vs. Estimated Efficiency for Linear Regression	125
Figure 6.17. Measured Efficiency vs. Estimated Efficiency for Nonlinear Regression	126
Figure 7.1. Effective cutting length	130
Figure 7.2. Camera setup	132
Figure 7.3. Working principle of the optical microphone	133

Figure 7.4. Acoustic sensor setup	135
Figure 7.5. Preliminary acoustic measurement [just the water jet is on first-200 (bar), then gas flow is turned on-1 (l/min), and then laser is turned on-80%-2.00 (μs)-10 (kHz)]	136
Figure 7.6. Images for different command values [water pressure is 200 (bar), gas flow is 1 (l/min), RF-off time is 2.00 (μs), and frequency is 10 (kHz)]	138
Figure 7.7. Average pixel brightness vs. measured laser power in water (outliers are grouped)	140
Figure 7.8. Images for different laser parameters [water pressure is 200 (bar), gas flow is 1 (l/min), and the selected area is where the average brightness of the pixel values are calculated]	140
Figure 7.9. PSD comparison of different conditions.....	142
Figure 7.10. PSD plots a) Water pressure comparison [gas flow is 1 (l/min), command is 80%, RF-off time is 2.00 (μs), and frequency is 10 (kHz)], b) Gas flow comparison [water pressure is 200 (bar), command is 80%, RF-off time is 2.00 (μs), and frequency is 10 (kHz)]	144
Figure 7.11. PSD plots a) Command comparison [water pressure is 200 (bar), gas flow is 1 (l/min), RF-off time is 2.00 (μs), and frequency is 10 (kHz)], b) RF-off time comparison [water pressure is 200 (bar), gas flow is 1 (l/min), command is 80%, and frequency is 20 (kHz)], c) Laser frequency comparison [water pressure is 200 (bar), gas flow is 1 (l/min), command is 80%, and RF-off time is 2.00 (μs)]	146
Figure 7.12. Average sound amplitude in a.u. in the 200–600 (kHz) range vs measured laser power in water.....	147
Figure 8.1. Working principal of the optical microphone.....	153
Figure 8.2. Photo of the drilled samples	155
Figure 8.3. Acoustic measurement setup	157
Figure 8.4. CT cross-section image of Ø0.4 (mm) hole from 1 to 17 cycles.....	159
Figure 8.5. Hole depth vs. number of cycles for different hole diameter values .	159
Figure 8.6. Change of hole morphology during drilling	163
Figure 8.7. Spiral toolpath going outward for Ø0.4 mm and 0.05 mm stepover .	164

Figure 8.8. PSD plot comparison for laser off and on conditions	165
Figure 8.9. PSD comparison between Ø0.2 (mm) and Ø0.4 (mm) holes, 1 st cycles	166
Figure 8.10. PSD comparison between the 1 st and the 10 th cycles for Ø0.4 (mm) hole	166
Figure 8.11. Calculating the average sound amplitude for each cycle from the energy curve with a sliding window. Example plot is for Ø0.4 (mm), from 10 th to 20 th cycle.....	167
Figure 8.12. Average sound amplitudes depending on the hole diameter and the number of cycles. The amplitude values are scaled by log function.....	168
Figure 8.13. Energy curve at 200 (kHz) for Ø0.4 (mm) and 20 th spiral cycle, showing the threshold value and cycle start-end	170
Figure B.1. A screenshot from the working code	193

LIST OF ABBREVIATIONS

ANN	Artificial Neural Network
ANOVA	Analysis of Variance
CNC	Computer Numerical Control
CT	X-ray Computed Tomography
DDR	Depth-to-Diameter Ratio
DOE	Design of Experiment
E	Electric Field
EDM	Electrical Discharge Machining
FEM	Finite Element Method
GA	Genetic Algorithm
GRA	Grey Relational Analysis
H	Magnetic Field
HAZ	Heat Affected Zone
LBM	Laser Beam Machining
LMJ	Laser Micro Jet
MLP	Multi-Layer Perceptron
MRP	Material Removal per Pulse
MRR	Material Removal Rate
MSD	Mean Square Deviation
Nd:YAG	Neodymium-doped Yttrium Aluminum Garnet

NA	Numerical Aperture
OEC	Overall Evaluation Criteria
PCA	Principal Component Analysis
PSD	Power Spectral Density
Q	Quality Factor
R^2	Coefficient of Determination
RF	Radio Frequency
RMSprop	Moving Average of Squared Gradients
Rq	Root-mean-square Surface Roughness
RSM	Response Surface Methodology
S	Standard Error of Regression
SNR	Signal-to-Noise Ratio
SS	Stainless Steel
STFT	Short-time Fourier transform
tanh	Hyperbolic Tangent
TBC	Thermal Barrier Coating
WJGL	Water Jet Guided Laser

LIST OF SYMBOLS

a	Number of pixels
A	Water jet cross-section area (μm^2)
c	Speed of Light (m/s)
C_p	Specific heat [$\text{J}/(\text{g}\cdot\text{K})$]
D	Laser beam diameter (mm)
D_b	Diameter of the hole at the bottom side (mm)
D_j	Water jet diameter (mm)
D_{nozzle}	Diameter of the nozzle
D_t	Diameter of the hole at the top side (mm)
d	Hole depth (mm)
d_v	Depth of material removal per laser pulse (mm)
E_{las}	Energy of the incoming laser beam (J)
E_p	Pulse energy (mJ)
E_s	Energy that reaches the surface (J)
f	Frequency (kHz)
F	Feed rate (mm/min)
F_{imp}	Impact force (N)
h	Planck's constant (Js)
I_p	Power density (GW/cm^2)
K	Nozzle loss coefficient
k	Thermal penetration depth coefficient
ℓ	Effective cutting length (mm)
L	Length of the water jet chamber (mm)
L_b	Stable water jet length (mm)

L_f	Melting energy (J/g)
L_v	Vaporization energy (J/g)
M	Slope coefficient
MRP	Material removal per pulse (mm ³) - measured
MRP_{th}	Maximum material removal per pulse (mm ³) - theoretical
MRR	Material removal rate (g/s)
n	Number of repetitions
p	Average pixel brightness value
P	Average laser power (W)
P'	Laser power in the water jet (W)
P_p	Peak power (kW)
R	Reflectivity
r_{jet}	Radius of the water jet (mm)
t	Process time (s)
t_b	Time required for a disturbance in jet radius to grow (s)
T_a	Taper angle (°)
T_0	Room temperature (K)
T_v	Vaporization temperature (K)
U	Speed of the water jet (mm/s)
V_{th}	Thermally affected volume (mm ³)
w_i	Weight of each characteristic
x	Total spiral toolpath length per hole (mm)
y	Real value of the data
y_0	Target value
y_a	Sample average value
y_i	Measured reading (observed result)

y_{imax}	Worst readings of each characteristic
y_{imin}	Best readings of each characteristic
y'	Normalized data
z'	Normalized standoff distance
α	Thermal diffusivity (mm ² /s)
β	Contraction coefficient
β_{max}	Frequency of most rapidly growing disturbance (Hz)
ΔH	Total vaporization enthalpy per mass (J/g)
$\Delta H'$	Total vaporization enthalpy per volume (J/mm ³)
Δm	Mass change of the workpiece (g)
ΔP	Pressure difference (N/mm ²)
δ_0	Amplitude of the initial disturbance
δ_{th}	Thermal penetration depth (mm)
η	Efficiency
η_p	Process efficiency
θ_{max}	Acceptance angle of the water jet (°)
λ	Wavelength (m)
μ	Mean value of the data
ρ	Density (g/mm ³)
σ	Standard deviation
σ_w	Surface tension of water (N/mm)
τ	Optical loss coefficient
τ_p	Pulse width (ns)
φ	Laser fluence (J/mm ²)
φ_{th}	Threshold fluence (J/mm ²)

CHAPTER 1

INTRODUCTION

The components used in gas turbines work at high temperatures. In order to endure the harsh conditions and increase durability, parts are made of special aerospace materials, such as nickel-based alloys and micro holes are drilled on them to help with cooling. These materials are hard and the diameter of the holes are small. Thus, non-traditional manufacturing methods are preferred, such as Electrical Discharge Machining (EDM) or Laser Beam Machining (LBM), to drill the parts. As described in Chapter 2, Water Jet Guided Laser (WJGL) is a novel manufacturing technology that overcomes the adverse effects of conventional laser drilling. In this hybrid process, the laser beam is guided through a thin cylindrical water jet, and the pressurized water provides focusing, cooling, and cleaning on the machining region.

Literature survey on conventional dry laser drilling and WJGL drilling is given in Chapter 3. The reviewed literature shows that the following topics are important:

- Determination of the critical process parameters
- Determination of the effects of certain laser parameters on specific materials
- Optimization of the process time and quality
- Modeling and simulation studies on material removal and quality

The machine parameters, material properties, and hole geometry need to be correlated to the process time and quality for the WJGL micro hole drilling process. However, research on the WJGL technology is highly limited.

As described in Chapter 4, the physics of the material removal in WJGL is highly complex due to scattering and reflection losses at the surface, with heat diffusion causing phase change, melting, and/or vaporization. Thus, determining the proper machining parameters to achieve acceptable process time and quality is worth to be studied. A material removal model for WJGL micro hole drilling of nickel-based

aerospace alloys has not been encountered in the literature. Additionally, on the particular WJGL machine used in this study, a real-time process monitoring about the machine parameters and machining conditions, is not available.

1.1 Motivation and Scope of the Study

As discussed above, very limited research study is available for WJGL and there are several missing points for this process. These have caused motivation to conduct a research study, which would contribute to the science and technology by modeling and optimization of the process parameters for micro hole drilling of nickel-based aerospace alloys.

A methodology is required and should be developed which shows the parameters need to be set, their levels and their order for efficient and good quality micro hole drilling by WJGL. The new approach would eliminate the need of going through a trial & error cycle on the particular machine. It would be possible to predict the process time for a given material and micro hole geometry. Real-time process monitoring solutions are needed as well.

In order to achieve these, a systematic approach and evaluation of the technology should be performed. WJGL drilling of different nickel-based alloys, such as Inconel 625, Inconel 718, and CMSX-4, which are commonly used in aerospace industry and micro hole geometries should be studied. Different methodologies including machine learning, statistical modeling, and mathematical modeling can be used, together with experimental studies.

The scope of the study is modeling and process optimization of WJGL micro hole drilling on nickel-based aerospace alloys, for the purpose of contributing about the needs described in the above paragraphs.

1.2 Organization of the Thesis

The motivation behind the study is discussed and the scope of the study is presented in Chapter 1. WJGL technology is described in detail in Chapter 2. Literature survey on laser drilling and water jet guided laser machining is provided in Chapter 3. Chapter 4 focuses on the material removal mechanism for conventional laser machining and water jet guided laser machining. In Chapter 5, investigation of effects of machining parameters and an experimental study in terms of cycle time and hole quality for hole drilling are presented. In Chapter 6, a holistic and simplified process model for the water jet guided laser process is introduced and material removal of the process is modeled. Two different real-time measurement methods, which are image processing and acoustic sensing, to find out the laser beam characteristics in the water jet are introduced in Chapter 7. Effects of the hole geometry on the machining behaviour in terms of process limits, material removal rate, machining efficiency, and the quality is discussed in Chapter 8. In Chapter 9, the conclusions and main contributions of this study are presented and recommendations about future work are provided.

CHAPTER 2

WATER JET GUIDED LASER TECHNOLOGY¹

In the WJGL system, the laser beam is focused on a water jet nozzle so that the laser energy can be carried by total internal reflection within the pressurized jet. The working principle of the technology is shown in Figure 2.1. The physics of the material removal process is highly complex. The laser radiation heats up the machining area, whereas pressurized water flow cools down the surface at the same time. There are optical absorption, heat transfer, and material phase transformation mechanisms at the laser-material interface that should be considered. Furthermore, the laser beam might be blocked for some cases due to the water jet splashing back from the machined cavity or the evaporated material plume from the surface decreasing machining efficiency. There are many considerations and adjustable variables in the process, which affect the Material Removal Rate (MRR) and the quality of the cuts. This chapter briefly introduces the technology, the machining parameters and some important considerations about the process.

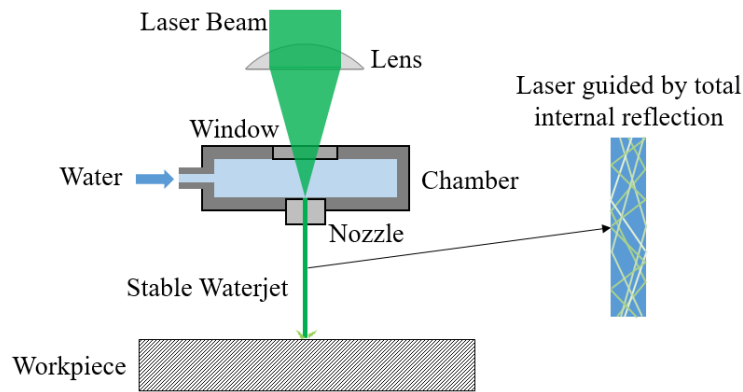


Figure 2.1. Working Principle of WJGL

¹ This chapter is based on [135], which is a published work of the author

2.1 Machine Controller

The laser and all of the auxiliary equipment are integrated onto a 5-axis Computer Numerical Control (CNC) machine. The block diagram of the system can be seen in Figure 2.2. The machine can be operated by either manual input or an automated script. The input is introduced to the machine via an interface. Following that, a computer unit processes the input and sends signal to the controllers of the subsystems. Laser controller allows distinct values to be set to obtain different laser parameters. Water and gas supplies can be turned on and be adjusted by automated pressure and flow control valves, respectively. Mitsubishi CNC controller is used on the machine to control the axes. The output from the subsystems combine on a physical machining unit, which is used to perform the machining operation, and the workpiece. Machining unit moves in X and Z axes, while the workpiece can be manipulated in B, C, and Y axes, simultaneously.

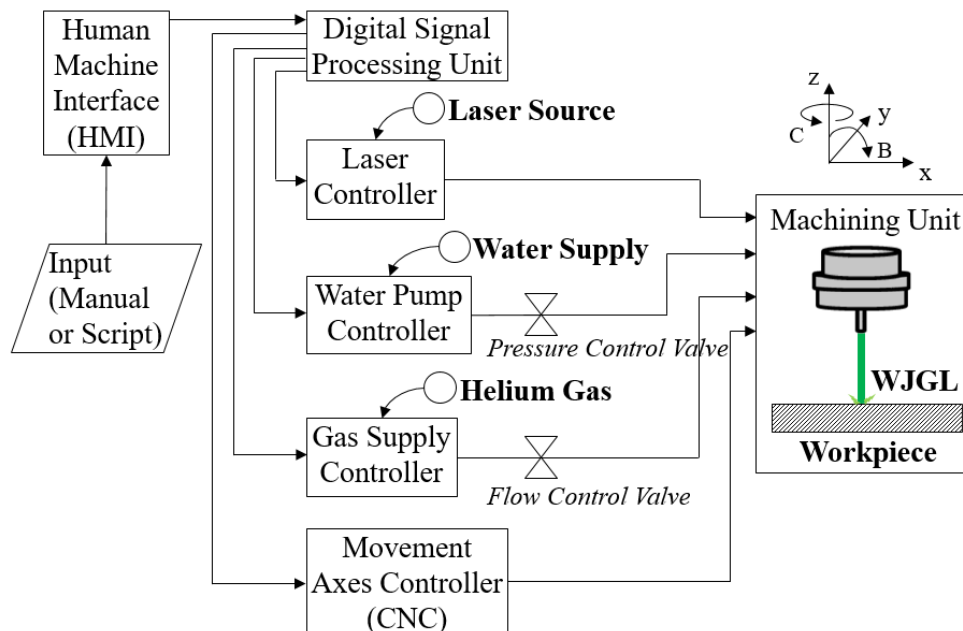


Figure 2.2. Machine Block Diagram

2.2 Water Jet System

The water jet system consists of a high pressure water pump and gas flow controller. The water used in the process is purified by reverse osmosis method to a specific level of conductivity so that it can be used as a dielectric waveguide for the laser beam. In order to stabilize the water jet, helium is used as an assist gas. It is possible to adjust the water pressure and gas flow, separately. Water jet nozzles are generally made of diamond or sapphire, and the diameters are ranging between 40 (μm) to 60 (μm) for micro drilling purposes.

2.3 Laser System

The laser used in the system is a diode-pumped solid state Neodymium-doped Yttrium Aluminum Garnet (Nd:YAG) type, operating at 1064 (nm) wavelength. A harmonic separator transforms the wavelength to 532 (nm) green light. This wavelength is specifically chosen for the process since absorption of laser power is very low in water [1] and absorptivity by metals is better [2]. A q-switcher transforms the continuous wave to nanosecond pulses. Nanosecond pulse widths provide a good trade-off between productivity and quality for micro drilling. The repetition rate of the laser is in (kHz) range. Average laser power is 100 (W). The schematic representation of the laser system can be seen in Figure 2.3.

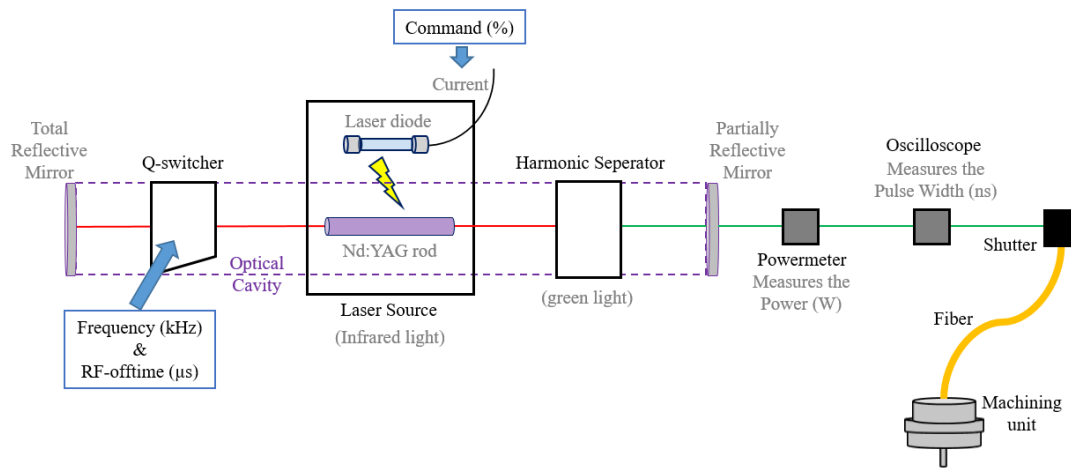


Figure 2.3. Schematic Representation of the Laser System

The frequency is an adjustable input to the system. However, it is not possible to set the power and pulse width variables directly. The power is indirectly controlled by a command value, which sets the current of the laser diode. Similarly, pulse width can be determined by setting another input called the radio frequency (RF) off time. The RF-off time defines the time during which the Q-switch becomes transparent and let the cavity lasing so that the energy stored in the rod is released. These three major laser parameters interdependently affect the average output power and pulse width. Thus, there is a need to measure the power and pulse width of the produced laser beam using an internal powermeter and oscilloscope. The relation of the obtained laser parameters (power, frequency, and pulse width) on a time scale can be seen in Figure 2.4.

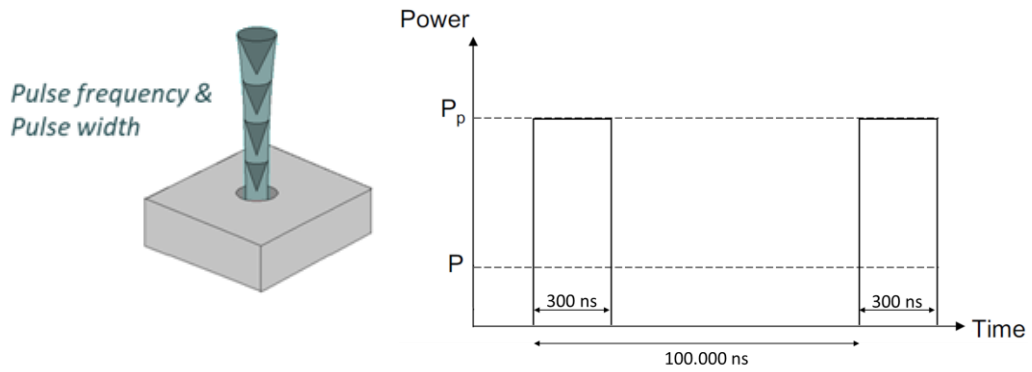


Figure 2.4. Example for 10 (kHz) frequency and 300 (ns) pulse width

Following that, the laser beam is conveyed to the nozzle with a fiber and to the workpiece with water, which are both dielectric waveguides. The beam profile in the water is a *top-hat* profile. Dispersion effect (change of pulse width) is negligible since the distance is only a few meters. However, attenuation (change of power) is not negligible. There is always loss of power due the optical components (fiber, lenses, glasses, water, etc.) used in the system, as well as non-linear laser interactions in the water jet. Thus, the laser power employed on the workpiece is not directly controllable. It can only be measured using an external waterproof powermeter.

2.4 Process Window for Machine Parameters

The solid range of the adjustable parameters via the machine interface are given in Table 2.1. The limits are the machine constraints.

Table 2.1 Machine Parameters

Command (%)	48.5 – 82.5
RF – off time (μ s)	0.02 – 8.00
Frequency (kHz)	6 – 60
Water pressure (bar)	50 – 500
Gas flow (l/min)	0.1 – 2.0

Similarly, there is a power density constraint for the machine. The damage threshold of the water jet nozzle is approximately 1 (GW/cm²). This limit should not be exceeded. Thus, the laser parameters have to be chosen accordingly, meaning that the process window for the laser parameters are decided by the power density constraint. In order to calculate the power density, I_p , on the nozzle depending on the laser parameters, series of equations shown below can be used [3].

$$E_p = P/f \quad (2.1)$$

$$P_p = E_p/\tau_p \quad (2.2)$$

$$I_p = P_p/A \quad (2.3)$$

where, E_p is the pulse energy, P is the average laser power, f is the frequency, P_p is the peak power, τ_p is the pulse width, and A is the water jet cross-section area. The area is calculated by using the diameter of the nozzle and multiplying it by a contraction factor, which shows the ratio of the water jet diameter compared to the nozzle diameter. Similarly, the power should be calculated by taking into consideration the transmission loss factor in the optical system until reaching the water jet nozzle. Measurements show that these factors are approximately 0.83 and 0.75, respectively. Following that, using Equation (2.1), Equation (2.2), and Equation (2.3), taking the nozzle diameter as 50 (μm), using the related factors and the unit conversions, below equation is obtained for the power density.

$$I_p = \frac{55.475P}{f\tau_p} \quad (2.4)$$

The power density (or peak intensity) is a compact value including all of the laser parameters. In order to stay below the damage threshold, power should be selected lower or frequency and pulse width should be selected higher. Taking I_p as the nozzle damage threshold of 1 (GW/cm²), the three unknowns in Equation (2.4) define a surface, as can be seen in Figure 2.5. Above the surface is the safe region, where WJGL can be operated.

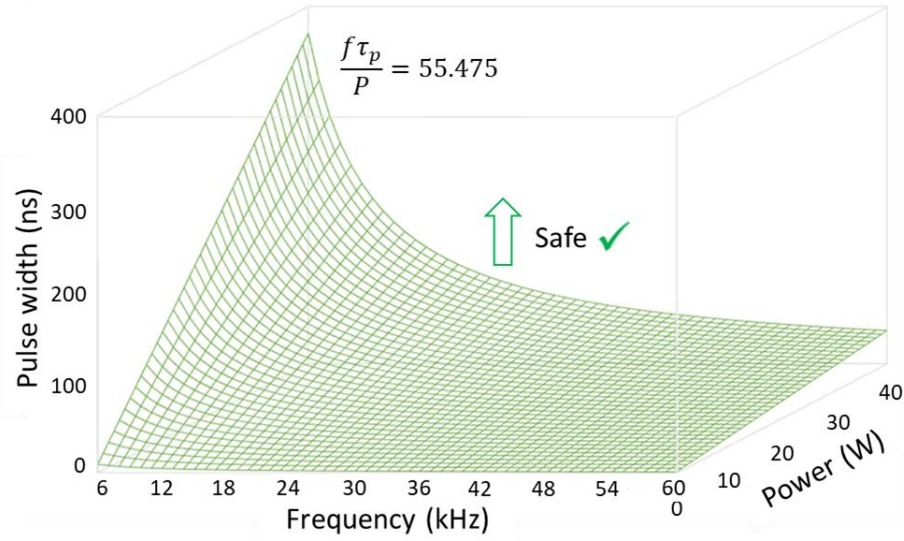


Figure 2.5. Design Space for the Laser Parameters

2.5 Effective Cutting Length

On the WJGL system, as the laser beam leaves the nozzle, a phenomenon called Raman scattering is observed within the dielectric water jet. The laser beam encapsulated within the jet is visible to some extent and that visible portion is the effective cutting length, as shown in Figure 8. The laser light breaks up and leaves the jet at the end of this length. The laser power decreases gradually along the length due to losses by nonlinear effects [4] and diminishes drastically at the end, generally below the material removal threshold for most metal alloys. Thus, machining stops beyond the effective cutting length.

The effective cutting length can be altered by adjusting laser and water jet parameters. It is important to know about the length before performing drilling so that the standoff distance for the nozzle can be adjusted accordingly. If the standoff distance is too high, there will not be enough laser energy reaching the surface of the workpiece. If it is too low, there will be a risk of back-wall damage on the machined parts, which is a critical issue especially for drilling hollow turbine blades, as can be

seen in Figure 2.6. WJGL, just like other laser systems, cannot prevent the laser beam reaching beyond the other side of the hole after breaking through the material.

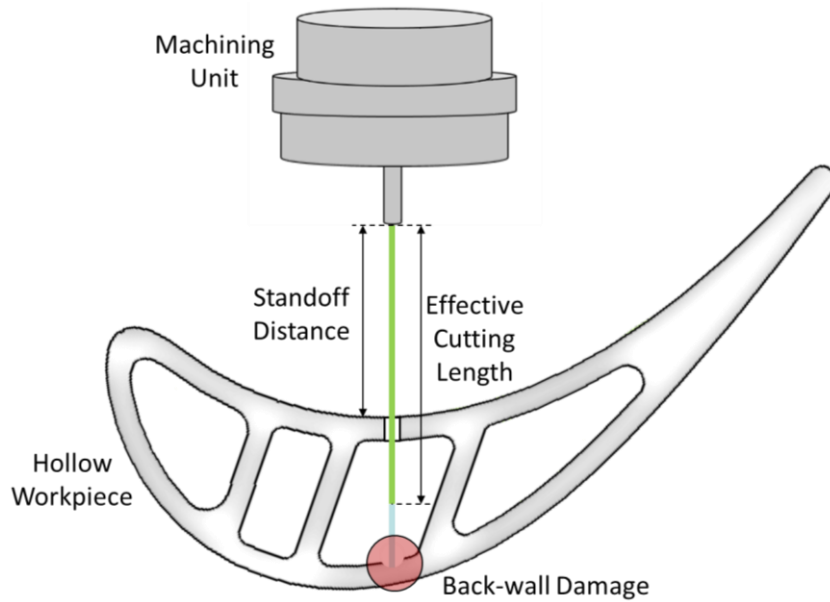


Figure 2.6. Effective Cutting Length

2.6 Drilling Strategy

On the WJGL system, the water jet splash back from the surface might become an issue while machining. The reflection of pressurized water from the machining area might block the laser beam and decrease the machining efficiency. This is especially more considerable when the diameters of the drilled holes are small, as the water jet is redirected along the walls of the cavity and exits from the hole entry with high velocity. Consequently, the jet entering the cavity needs to penetrate against a counter flow. In practice, this effect is mitigated by using a water jet diameter smaller than the desired hole diameter, and by moving the water jet in spiral motion, as shown in Figure 2.7.

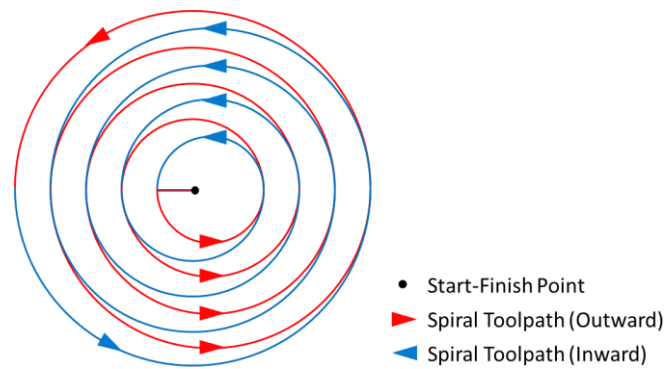


Figure 2.7. Spiral Toolpath

Spiral drilling is different than the conventional methods used, such as percussion or trepanning drilling. The spiral toolpath removes the material inside the cavity layer by layer, which is useful for avoiding undesirable artifacts on the perimeter of the holes and increasing quality, such as roundness and taper [5,6]. The toolpath works in the X-Y plane, and can be parametrically adjusted by defining the diameter and the size of the spiral step. Since the laser beam can focus on a small spot, which is as wide as the water jet diameter, it is also possible to apply different toolpath strategies for machining different shapes of micro holes.

CHAPTER 3

LITERATURE SURVEY ON LASER BEAM MACHINING AND WATER JET GUIDED LASER DRILLING

In this chapter, the literature behind the related areas of the thesis is investigated in a categorized manner. The reviewed literature shows the important topics to be covered in the thesis study.

3.1 Studies on Conventional Dry Laser Drilling

There are many studies on laser processing for different materials and geometries. In order to focus on the related research, this section is contracted to include only the studies on aerospace alloys and thoroughly cut micro holes. Other materials (such as ceramics, copper, glass, silicon, etc.) and other geometries (such as nano holes, large holes, blind holes, pockets, grooves, etc.) are not considered.

There are a variety of laser types that are used for micro hole drilling of aerospace alloys, such as Nd:YAG lasers, fiber lasers, or Carbon Dioxide (CO₂) lasers, all at different wavelengths. The lasers have pulse widths varying between femtoseconds (fs) to milliseconds (ms) range. The materials that are used differ and some studies inspect the coating on the parts. A variety of hole diameters and depths are considered. The techniques used for hole drilling are mostly percussion or trepan drilling. Figure 3.1 shows different types of drilling. There are many studies on modeling, simulation, and optimization of laser drilling in the literature. Some of them are purely experimental, while the others include some kind of mechanistic, numeric, or statistical models.

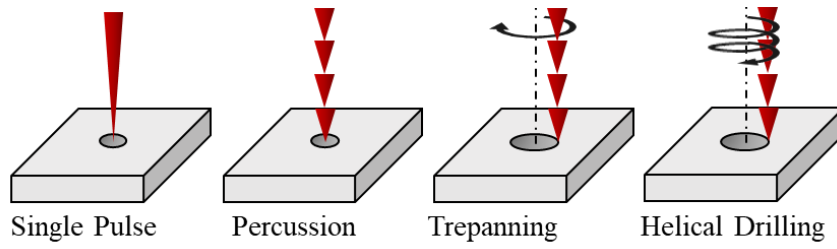


Figure 3.1. Laser Hole Drilling Methods [7]

3.1.1 Modeling Studies

In one of the earliest studies, Yilbas [8] observed the affecting parameters for laser drilling of sheet metals. The relations between inputs and outputs were analyzed. The effects of each input on the outputs were described. It was found that the laser energy has a strong influence on all geometric features of the hole, such as dimensions, taper and recast layer. Furthermore, there is a linear dependence on the responses. Interactions between the factors also came out to be significant. Similarly, Forget et al. [9] performed Nd:YAG laser drilling tests on ceramic coated Nickel-based Hastelloy X plates with percussion method. A simple thermal modeling with an energy-matter balance was also developed and tested with experiments. The effects of pulse length, frequency, and power intensity on hole depth and diameter were investigated. The model was useful for predicting the MRR and thus optimizing the input parameters for percussion drilling.

Yilbas et al. [10, 11] focused on the heating mechanism of the laser, including absorption and evaporation. Steady state evaporation was assumed. Both conduction and convection effects were taken into account. Experimental work was conducted with a pulsed Nd:YAG laser on Titanium, Nickel, and Stainless Steel (SS) samples. It was found that the temperature below the surface could be more than the temperature at the surface during drilling. In addition, the plasma formed over the surface had an effect on the power intensity of the laser beam. The absorption coefficients based on the distance were computed. Another study is related to thermal stress modeling for trepan drilling of Titanium alloys [12]. An FEM model was

developed, which could predict the temperature and stress fields in the cutting region. Experiments were performed to check the temperature predictions. The residual stress developed at the vicinity of the cut surface was measured, as well. Since the thermal diffusivity of the alloy was low, the resulting Heat Affected Zone (HAZ) was narrow. Because of the annealing effect, temperature decay was found to be gradual in the area where the cutting ends. The maximum value of von Mises stress was lower in this area. However, the stress was higher inside the hole. The reason was stated as the thermal expansion effect during heating and contraction of the work piece during cooling. The maximum value of von Mises stress occurred at the mid-thickness of the work piece. It was found to be possible to increase the quality of the holes with the cutting parameters that caused lower stress levels around the hole edges.

Sibalija et al. [13] presented a different approach for determining the optimum laser parameters for Nd:YAG laser drilling. Different quality characteristics of the holes were taken into account. A hybrid design strategy was developed using two approaches based on the experimental data. Principal Component Analysis (PCA) was used as a first step to separate the responses, followed by Grey Relational Analysis (GRA), in order to form a performance measure. Artificial Neural Network (ANN) was used as the second approach, in order to find the optimal parameters and model the relation between the parameters and the performance measure. Genetic Algorithm (GA) method was also used to search for the optimum parameters. The experiments to obtain the dataset were performed on a sheet of Nimonic 263 super alloy. A limited number of dataset were obtained from the experiments. No assumptions about the process, parameters, or responses were defined in the design. Thus, the method was found to be suitable for a practical application and also applicable to other processes. Similarly, Yilbas [14] performed a parametric study to observe the quality of the drilling process. The hole quality was measured depending on the laser parameters and the material properties. A statistical approach was used to find out the significant factors. Experimental work was conducted with a pulsed Nd:YAG laser on Titanium, Nickel, and SS samples. The workpiece thickness was

found to be the most important factor affecting the quality. The other most important factors were focus setting and pulse energy. The mean hole diameter was increased by the pulse energy. It was observed that the optimum value of the focus differs for each material. Mishra and Yadava [15] created a numeric and statistical model for percussion drilling and then used it for optimization. A hybrid methodology was developed to predict quality and MRR for drilling. FEM and ANN models were used for this purpose. FEM model included the thermal, optical, and phase change properties of the material. Experiments were performed for validation of the thermal model in terms of hole taper. The results were used to obtain a dataset for training and testing of the ANN model. Verification experiments were performed on Nickel-based Inconel 718 sheets using an Nd:YAG laser. Using PCA together with GRA, an optimization of the process was performed. The ANN was used to predict the quality and MRR results of the process. The results showed that an increase of pulse width and peak power also increases the taper, HAZ, and MRR. Frequency variable was the major controllable input, which significantly affected the quality results. Good quality holes were obtained by using the optimum process parameters. A reduction of taper and HAZ, and an increase of MRR was obtained.

Ganesh et al. [16] proposed an axisymmetric (2D) model for laser drilling in metals. A computer simulation of the process was developed with some assumptions in the physical model, in order to simplify the process. The melt area was treated as a deformable surface. Gas dynamics model was used to calculate the pressure and temperature on the melt area, whose vaporization kinetics were discussed. The re-solidification of the melt area was modeled, as well. Simulations were done with different laser intensity profiles. It was found that the recast layer forms between the pulses and highly affect the hole formation. The effect of vaporization came out to be less. The experiments were conducted on Nickel-based Hastelloy X material. The results of the tests agreed with the model. Horn et al. [17] studied both percussion and trepanning drilling on TBC coated Nickel-based CMSX-4 alloy with different angles and with different assist gases. A Finite Element Model (FEM) was developed to visualize the numerical solution of the 2D moving boundary and heat conduction.

It was found that the melt front velocity for percussion drilling depends on the power intensity and on the beam diameter. Greater melt front velocities were achieved with a larger beam diameter. Using large pulse widths, more melt was produced than can be expelled, which caused insufficient melt removal from the area. The melt front velocity while using Argon as assist gas was found to be five times higher than using Oxygen. For the trepanning method, the melt thickness showed dependence on the gas pressure and the thickness of the sample. A higher pressure was needed to remove the melted material from the hole as it got deeper. It was also found that the same hole drilling parameters are valid for both layers (coating and alloy). Sezer et al. [18] carried out Three Dimensional (3D) numerical simulation of laser beam heating. The model predicted a higher heat transfer rate at hole entrance and exit. This calculation implied larger HAZ and smaller recast. The experiments were performed on TBC coated Nickel-based Nimonic 263 alloy at different drilling angles. It was found that HAZ and recast layers get thicker for smaller drilling angles to the surface. Also, larger HAZ was measured, as predicted by the model, at the hole entrance and exit.

Arrizubieta et al. [19] used a fiber laser and percussion drilling method to understand the hole formation mechanism on SS material. The hole diameter and hole shape were characterized by changing the pulse number. For each laser pulse, the removed material volume was calculated. The evolution of the hole geometry for the each laser pulse was obtained. A numerical model was developed as well, which can predict the resulting hole geometry for different pulse numbers. The model took into account the vaporization effect. The model helped with determining the significant process parameters. The results showed that the MRR decreases for each consecutive pulse. This was because the laser beam defocused while the hole became deeper. Furthermore, the model demonstrated that vaporization of the material is the main mechanism determining the formation of the holes in the laser percussion drilling process. Wang et al. [20] performed a computational study on hole evolution in Nd:YAG laser drilling of TBC coated Nickel-based Inconel 718. The developed FEM model, involving thermo-mechanical coupled analysis, predicted the thermal

stress distribution and crack formation. A visualized stress distribution is provided in Figure 3.2. A relation between number of pulses and hole depth was also established. The inputs to the model were material properties, laser power, and pulse width. It was found that using higher peak power intensity speeds up the laser drilling process. When lower laser peak power was used, no drilling effect was obtained. The results showed that the thermal stress at the machining region is responsible for the crack formation.

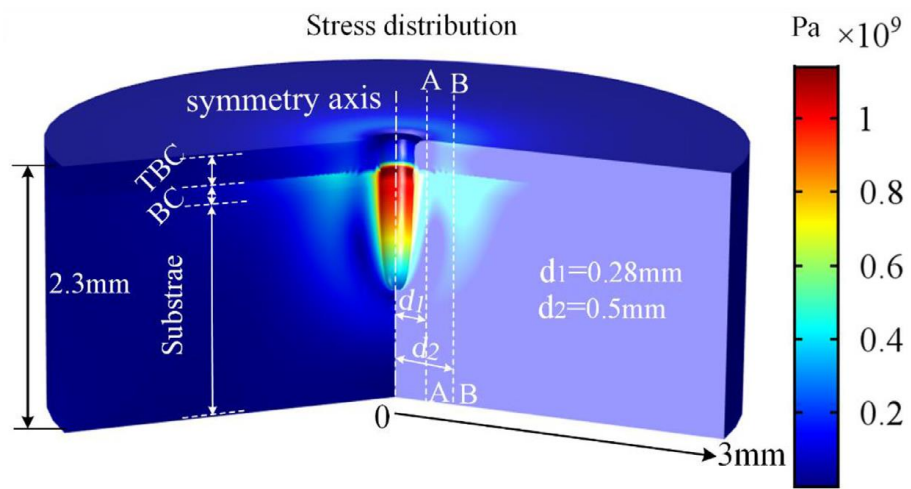


Figure 3.2. The Distribution of Thermal Stress After Five Pulses [20]

Afrasiabi et al. [21] developed a mesh free method for MRR prediction in laser drilling. Laser was described as an external heat source and a static beam with a Gaussian intensity distribution was assumed. Following that, the transient state heat transfer problem was solved. Validation experiments were performed using a single-pulse laser on a SS workpiece. The numerical procedure performed in the study was a 2D approach. As a result, the penetration depth was predicted. However, the model did not consider many aspects of the process, such as the molten material, assist gas used, ejected particles, pulsed lasers, and recast layer.

3.1.2 Experimental Studies

Tam et al. [22] performed process time optimization of Nd:YAG laser percussion drilling on Nickel-based Inconel 718 material using the Taguchi method. 1 (mm) holes were drilled on 25 (mm) thick coupons. Five different input factors were used. It was revealed that drilling time was significantly affected by pulse energy, pulse width, pulse shape, and the interaction between the factors. The optimum levels of the factors were also determined. Chen et al. [23] performed an experimental study on three different aerospace alloys using pulsed lasers. Laser wavelength, power, and pulse width parameters were found to be the dominant factors that affect the quality. Recast layer and crack formation decreased with high peak power and short pulse width. Wu et al. [24, 25] studied drilling of Nickel-based Inconel 718 material by high intensity pulsed ultraviolet laser. Experiments were conducted with different wavelengths. Shorter laser wavelength caused less recast layers and micro cracks. However, slower drilling speed was observed. In order to increase the quality and speed, a multi step drilling methodology was proposed. Holes were drilled by the 1064 (nm) laser and 266 (nm) laser consecutively to reduce the recast layer. Corcoran et al. [26] studied percussion drilling of TBC coated Nickel-based Rene 80 aerospace material with Taguchi Design of Experiment (DOE). The significant parameters effecting the hole diameter, recast layer, and micro cracks were found out. It was found that shorter pulse width and higher gas pressure reduces micro cracks. Recast layer was reduced by lower pulse energy. Bandyopadhyay et al. [27, 28] focused on dimensions and metallurgical characteristics of Nd:YAG laser percussion drilled holes in aerospace alloys. Hole diameter, taper, spatter, recast layer, and HAZ characteristics were measured. The hole quality was significantly influenced by the type of material, thickness, laser pulse frequency, and pulse energy. Higher values of frequency and pulse energy were found to cause less taper and recast layer. Ghoreishi et al. [29, 30] studied taper angle and circularity in laser percussion drilling of SS material. Laser peak power, frequency, pulse width, number of pulses, gas pressure, and focal plane positions were adjusted for the purpose of optimization.

The Response Surface Methodology (RSM) was used to analyze the effects of the process variables. Higher focal distance, peak power, number of pulses, assist gas pressure together with moderate pulse width increased the hole quality in terms of taper and circularity. It was found that the frequency variable did not affect the taper. Leigh et al. [31] investigated the effects of process parameters on the metallurgy and geometry of laser percussion drilled holes on Nickel-based CMSX-4 alloy. The controllable factors were chosen to be the number of pulses, assist gas pressure, nozzle standoff distance and focal plane position. RSM was used to develop the models. It was found that the recast layer is minimized for a zero focal plane position and high pulse number. In addition, taper was found to be affected by gas flow, especially the standoff distance. Biswas et al. [32, 33] performed micro drilling experiments with a nanosecond pulsed Nd:YAG laser on Gamma-Titanium Aluminide material. Lamp current, frequency, gas pressure, and thickness were the input variables. Hole diameter at entry, circularity at exit, and hole taper were considered as the response variables. RSM have been used. It was found that the inputs could be adjusted for achieving better results by using the RSM model. Lamp current was the most significant factor effecting all the responses. Optimum results were obtained at moderate values of lamp current and higher levels of frequency, pressure, and sample thickness. Chatterjee et al. [34] performed drilling experiments on SS material using pulsed Nd:YAG laser. The effects of laser process parameters on the quality characteristics, such as spatter area and HAZ were analyzed. Laser energy, frequency, pulse width, and gas pressure were the input parameters. The most significant factors affecting the spatter area were laser energy and pulse width. Likewise, laser energy and frequency were the significant factors affecting HAZ. Lower spatter and HAZ were obtained at lower laser energy and pulse width and higher values of assist gas pressure.

VanderWert et al. [35] used trepan drilling on three different TBC coated aerospace alloys. Holes of diameter 0.5 ± 0.025 (mm) were obtained both by percussion and trepanning methods. Recast layer, micro cracks, and burrs were also observed or measured. It was found that assisting gas type, nozzle type, and gas pressure have

significant effects on process time and quality. Das and Pollock [36] performed experiments with a femtosecond laser on TBC coated Nickel-based CMSX-4 alloy using trepan drilling method. The surface quality of the holes were good and a certain degree of taper was observed. Femtosecond laser drilling process did not cause any other quality issues, such as recast layer or micro cracking. However, the machining time was too much [38 minutes for 1.5 (mm) thickness] per hole. Therefore, femtosecond lasers do not seem feasible for turbine blade cooling hole drilling. Antar et al. [37] compared EDM drilling to fiber laser trepan drilling. The tests were performed on Nickel-based Inconel 718 material. A full factorial DOE was designed to determine the optimum operating parameters for each process. Suitable process window for EDM and laser hole drilling process was identified. Drilling speed, recast layer, and taper was the response variables. Laser input parameters were power, frequency and feed. EDM results were superior in terms of recast layer, geometric accuracy, and taper, especially for thicker samples. Laser drilling, on the other hand, came out be faster than EDM drilling. Fan et al. [38] developed a multi stage method to drill TBC coated Nickel-based Inconel 718 material. In the first stage, the coating was removed with trepan drilling. Following that, percussion was applied to drill the hole. Finally, trepan drilling was used again to improve the hole quality. It was reported that recast layer and micro cracks decreased with this method. Morar et al. [39] studied the low cycle corrosion fatigue performance of the laser drilled Nickel-based CMSX-4 material. The correlation between trepanning speed of laser and recast layer was established. As the trepanning speed was increased, the recast layer thickness was also increased. Thus, a reduction in corrosion fatigue life was observed. Marimuthu et al. [40] performed drilling experiments with trepanning method on Nickel-based Nimonic alloy of 5 mm thickness. The hole diameter was 0.75 (mm). The factors taken into account were pulse energy, pulse width, frequency, assist gas type, gas pressure, and feed. It was found that using lower peak power and higher average power increased the hole quality, in terms of taper, recast layer and surface integrity. Parthiban et al. [41] optimized parameters for drilling of a TBC coated Nickel-based super alloy with a galvo scanner system. Inclination angle,

number of passes and scan speed were the input variables. Crack density and surface roughness of the holes were measured. Taguchi based DOE was used. The inclination angle and number of passes were the significant factors, which improved the surface integrity. Scanning speed had no considerable effect on the results.

Uchtmann et al. [42] used a hybrid approach, where they first sent millisecond (ms) pulses to the surface for fast drilling and then ultra-short pulses to clean up the HAZ. A spiral toolpath was used for drilling. Gruner et al. [43] used femtosecond laser pulses and percussion method to drill SS material. Pulse energy, fluence, frequency, and pulse number were changed to see the effects on hole diameter, circularity, taper, HAZ, and recast layer. First, the amount of pulses were determined for each thickness. Following that, other parameters were optimized for quality.

In their review study, Dubey and Yadava [44] summarized in a table the relation between the variation of parameters and quality characteristics, as shown in Table 3.1. It was stated that the material thickness is the most significant factor for most of the quality characteristics, such as HAZ, taper, and recast layer.

Table 3.1 Significant Factor Effects on Quality Characteristics [44]

Quality Characteristics	Significant Factors	Variation of Factors to Keep Minimum Value of Quality Characteristics
HAZ	Beam Energy	Low
	Feed Rate	High
	Pulse Duration	High
	Pulse Frequency	Moderate
	Gas Pressure	More
	Material Thickness	Low
Taper	Beam Energy	Low
	Feed Rate	High
	Pulse Frequency	Low
	Pulse Duration	High
	Material Thickness	More
	Focus Position	Above the Work Surface
Surface Roughness	Beam Energy	Moderate
	Feed Rate	Moderate
	Pulse Frequency	Moderate
	Gas Type	Inert
	Gas Pressure	Moderate
Recast Layer	Beam Energy	High
	Pulse Duration	Low
	Gas Pressure	High
	Material Thickness	Low
	Focus Position	Above the Work Surface
Dross Adherence	Gas Type	Inert
	Gas Pressure	High
	Beam Energy	High
	Feed Rate	High
	Pulse Frequency	Low
Micro-cracks	Beam Energy	High
	Pulse Width	Low
	Gas Pressure	High
	Gas Type	Inert

There are some studies in the literature, dedicated to identify or prevent spatter. Low et al. [45-49] performed tests on Nickel-based Nimonic 263 alloy. The effects of the process parameters on spatter deposition in percussion drilling were the focus of the studies. The characteristics of spatter under different assist gas types and process conditions were found out. The diffusion/bonding of the spatter to the substrate

surface was also measured. Finally, a special type of coating to prevent the spattering issue was suggested.

In closed form part geometries like the turbine blades, laser drilling creates the risk of *back-wall damage*. Figure 3.3 shows a simplified sketch of the problem. In the literature, there are patents that describe methods to protect the back-wall [50-53]. However, they all involve some kind of a blocking material to be placed inside the parts, which is difficult to remove later on. There are also studies that involve different kinds of *breakthrough detection*. It is possible to stop the drilling process once the hole is completed and therefore the back-wall is protected. Sheng and Chryssolouris [54] used acoustic sensing to detect breakthrough during through hole drilling. Tunna et al. [55] used a photodiode acting as a breakthrough detector. Sanikommu et al. [56] used a reflector material and a photo sensor. Moslehpour et al. [57] used a pressure sensor. Ho et al. [58, 59] used a coaxial camera system and machine vision approach. Even though they all had successful results, neither of these studies involved experiments on closed part geometries.

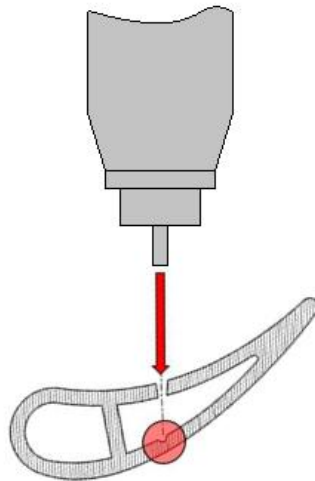


Figure 3.3. *Back-Wall Damage Problem*

3.2 Studies on WJGL Drilling

Taylor [60] showed in 1972 that a jet of a transparent liquid could entrap a light beam and act as an optical fiber. Based on this principle, Richerzhagen [61] invented a method and apparatus for machining material with a liquid-guided laser beam, later known as the Water Jet Guided Laser (WJGL) or Laser Micro Jet (LMJ).

There are only a limited number of studies in the literature on WJGL processing so far. Since it has been a patented technology provided only by a single company for many years, academic research is currently very limited. Most of the studies are related with dicing [62], grooving [63], cutting [64-67], and micro machining [68]. Drilling examples are less and only focus on the quality aspects.

Rashed et al. [69] performed drilling on SS fuel injector nozzles. The hole diameters were 180 (μm) and workpiece thickness was 300 (μm). A spiral toolpath was used. Surface integrity results were compared with EDM drilling. Figure 3.4 shows the 3D representation of the machined surfaces. R_q values measured from the hole surfaces were 450 (nm) and 150 (nm) for EDM and WJGL process. It was concluded that WJGL drilling is an alternative to EDM drilling, when repeatability and surface quality was concerned.

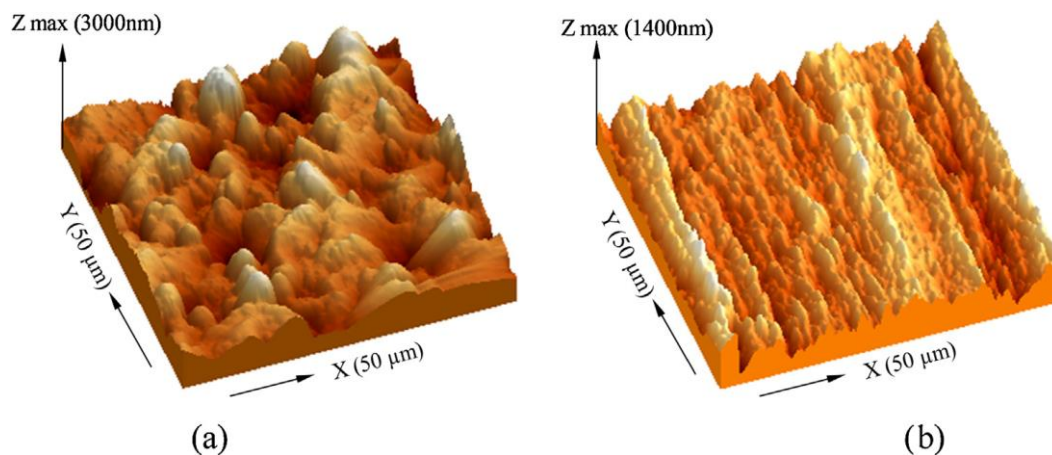


Figure 3.4. Representation of the Surfaces after (a) EDM (b) LMJ Drilling [69]

Gurav et al. [70] compared WJGL drilling quality results to conventional dry laser and EDM drilling on an aerospace Nickel-based super alloy, CMSX-4. Many holes less than 1 (mm) diameter were drilled for the experiments. Drilling was carried out in trepanning mode. The drilled holes were evaluated in geometric, surface quality, and metallurgical aspects. Consequently, WJGL drilled holes showed much improved quality. Circular and straight holes were obtained with no micro cracks and less recast layer with high surface finish. The holes were also without burrs or spatter. It was concluded that the process could be utilized to machine the cooling holes on turbine blades. As the HAZ was also found to be less with this process, the fatigue life of the parts can be improved.

The material removal mechanism was not properly addressed for the aforementioned studies. Nevertheless, there are some modeling studies dedicated to WJGL grooving and cutting, in which predictions are made for depth of material removal. Li et al. [71] presented a model for WJGL grooving of silicon, in which laser energy, water jet cooling effect, and melting of silicon are taken into account. The model was validated by comparing simulations with the experimental results. The shape and the width of the groove cross-section was successfully predicted for specific cutting speeds. It was also found that the maximum depth is reached with the first pulses of the laser and the depth of the groove is not steady especially for higher speeds. Yang et al. [72] came up with a numerical model estimating the temperature field on the cutting area for WJGL micromachining. It was stated that the temperature field of WJGL is less than the traditional dry LBM. Both conduction and convection heat transfer were considered and removed material volume was calculated. Validation experiments were performed on steel and silicon samples. It was concluded that the developed model is satisfied, but parameter optimization is needed for different materials. Adelman et al. [73] did an experimental study on WJGL cutting, showing the effect of using different process parameters on the cutting depth for different materials. It was found that the cutting depth increases with higher laser power and lower frequency. It was also observed that there is a dimensional depth limit for the

WJGL cutting and the material removal rate (MRR) decreases as it gets deeper into the slit, independent of the workpiece material. Diboine et al. [68] performed WJGL pocketing experiments on aerospace nickel alloys. A semi-empirical model was developed using energy balance approximation and 1D thermal diffusion. Prediction of depth per layer was done and validated by further experiments. Accumulation effect of water was reported to adversely affect the material removal as the toolpath got closer to the walls.

There are some studies in the literature, which takes advantage of the cooling effect of water, but in a different way. Either the water is used as an assisting flow on the workpiece surface or the workpiece is dipped completely into water.

Kruusing [74, 75], in his two review articles, pointed out advantages and disadvantages of processing with water assisted lasers. It was concluded that the quality is better due to cleaning, cooling, and smaller focal spot size. However, it was also stated that light absorption by the water and the mist in the process cause power loss and slower processing.

Water immersed (or underwater) laser drilling was experimentally studied by Tsai & Li [76], Iwatani et al. [77], and Chen et al. [78]. The materials and the target hole geometries were different for all the papers. However, they all concluded that the quality characteristics of the holes (micro cracks, HAZ, taper, and surface quality) got better with underwater laser drilling.

In some of the studies, water immersion technique is used together with ultrasonic assistance, where the ultrasonic waves are applied from above the surface using an ultrasonic horn. Liu et al. [79] stated that this method might generate better cleaning and cooling effects. Less debris deposition around the holes were observed. In another study by the same author [80], the effect of ultrasonic assistance on different materials were tested. It was found that the MRR is higher when compared to the results without ultrasonic assistance. Wang et al. [81], Shi et al. [82], Xia et al. [83], and Wang et al. [84] investigated the quality of different hole sizes on Nickel-based

super alloy GH4037. They measured circularity, surface quality, spattering, recast layer, HAZ, oxidation, taper, and hardness, and found superior results.

Kaakkunen et al. [85] used a sprayed thin water layer in the ablation region. Deep holes using a femtosecond laser were drilled in a silicon material with this method. It was found that the holes could be drilled faster and with the better quality. The water removed the debris and caused more efficient pulse energy transition into material compared to the ambient air.

Lopez et al. [86] proposed a water droplet assistance method as shown in Figure 3.5. An impulse shock pressure was obtained by injecting liquid micro-droplets at specific frequencies during drilling. The pressure was generated when the droplet was suddenly heated by laser. An explosive vaporization effect was obtained. Tungsten Carbide substrate was drilled with a nanosecond pulsed Nd:YAG laser. The results suggested that the impulse shock pressure could result in an increase in MRR and reduction in the spatter when compared to dry laser drilling. Taper was also minimized.

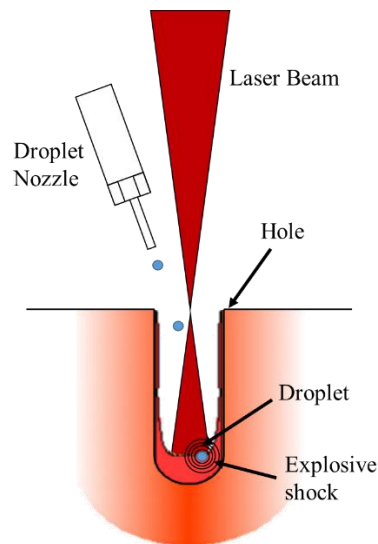


Figure 3.5. Schematic of Droplet Assisted Laser Micromachining Setup [86]

CHAPTER 4

MATERIAL REMOVAL MECHANISM OF LASER BEAM MACHINING AND WATER JET GUIDED LASER PROCESS

This chapter consists of two main parts. First, material removal mechanism for conventional laser machining is presented. Laser working principles, laser-material interaction theory and some important mechanisms are presented. Following that, the mechanisms involved in the WJGL process are elaborated. Emphasis is given on the water jet formation, laser-water jet interaction, and the material removal efficiency.

4.1 Conventional Laser Material Removal Mechanism

LBM is a widely used process for cutting and drilling materials. It is a thermal process, which utilizes light to heat up and remove material from the surface of a workpiece. The process will be explained in an orderly manner.

4.1.1 What is Laser?

Light is an electromagnetic radiation. It has an electric field (E) and a magnetic field (H). It propagates in waves, as shown in Figure 4.1. For each wavelength, there is a characteristic frequency. The relation is as follows: [87, 88]

$$\lambda = c/f \quad (4.1)$$

where λ is wavelength (m), c is the speed of light in vacuum (m/s), and f is the frequency (Hz).

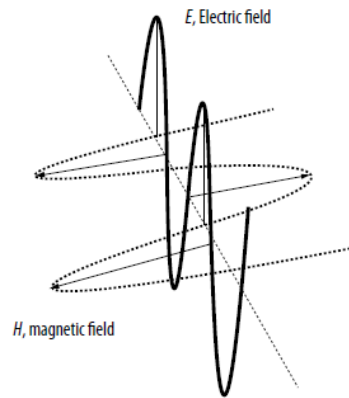


Figure 4.1. Propagation of light [89]

A laser device is an optical device used to change the properties of light.

A laser beam is distinguished from normal light by the following features: [87, 88]

- Parallel: It can move forward without scattering over a long distance.
- Monochromatic: Same wavelength.
- Coherent: Emitted waves are all in phase.

The difference between ordinary light and laser beam can be seen in Figure 4.2.

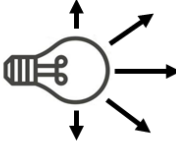

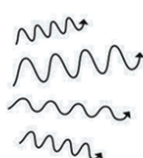

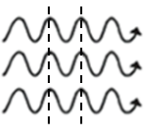
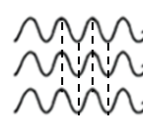
	Directivity	Monochromaticity	Coherence
Ordinary Light	 Light bulb	 Many different wavelengths	 Waves are not in phase
Laser Beam	 Laser	 Only one wavelength	 Waves run parallel to one another

Figure 4.2. Comparison of ordinary light and laser beam

4.1.2 How is a Laser Beam Formed?

The laser assembly consists of 3 different components, as seen in Figure 4.3 (a):

1. Active medium: Required to amplify the light. Solid, liquid, gas any material can be chosen. CO₂ and Nd:YAG (Neodymium doped Yttrium Aluminium Garnet crystal - Y₃Al₅O₁₂) are the most used materials. It determines the wavelength of light [89].
2. Pumping source: Required to excite the active medium. Lamp, diode, or electric current can be used. The laser power to be obtained is directly proportional to the pumping power [89].
3. Optical resonator: Required to provide optical feedback. It consists of two mirrors, one fully reflective and the other semi-transparent, placed opposite each other and parallel. It ensures that the laser beam is parallel and the usable beam emerges [89].

In order to use the resulting beam in material processing, additional equipment such as lenses, prisms, mirrors, fibers, cooling units for transmission, and focusing are also needed [90].

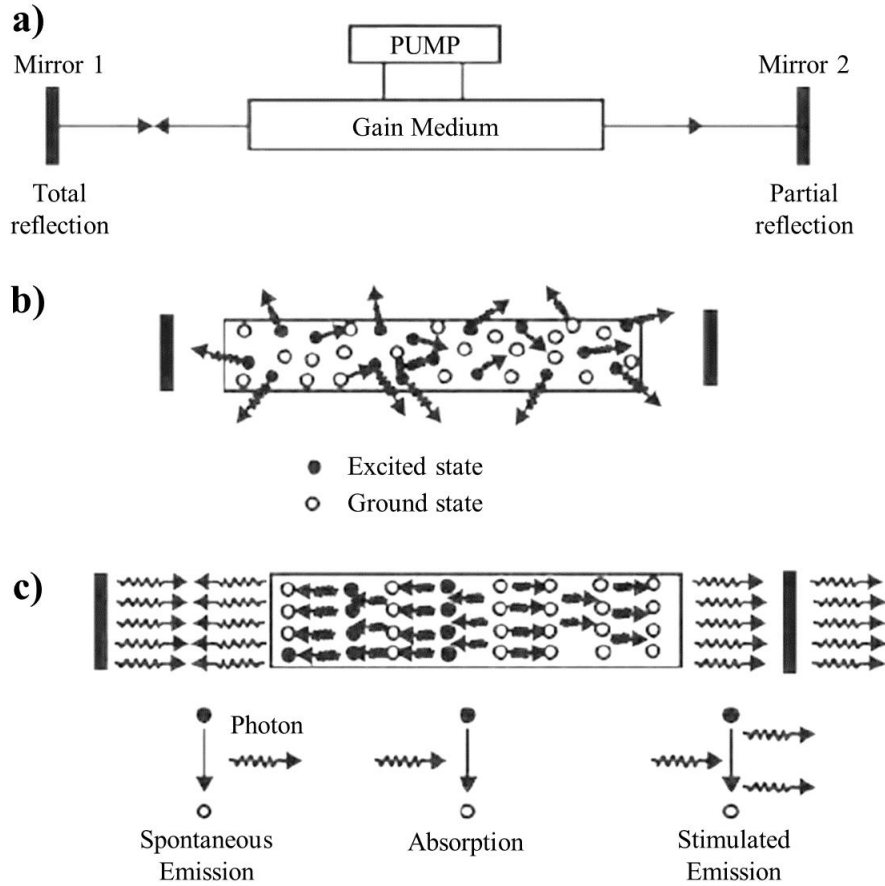


Figure 4.3. Inside a laser device [90]

According to the principle of quantum mechanics, when an atom is energized, it jumps to the upper energy level (E_2), but returns to its normal state spontaneously and momentarily (E_1). Meanwhile, it emits a photon with frequency f :

$$f = (E_2 - E_1)/h \quad (4.2)$$

where h is the Planck's constant [$6.62607004 \times 10^{-34}$ (Js)].

These oscillating photons also cause other atoms to jump to the upper energy level and release photons, as can be seen in Figure 4.3 (b). Photons that go back and forth on the same axis with opposing mirrors cause more photon oscillations with more collisions in a chain reaction. In each cycle, some of the photons leave the medium as a laser beam from the semi-permeable mirror, as can be seen in Figure 4.3 (c) [90].

4.1.3 Laser Pulse Generation

Q-switching is a method used to obtain nanosecond (ns) laser pulses. The power value obtained from the laser is limited by the threshold value of the photon population in the medium. One of the ways to increase power is to change the quality factor (Q), which determines the losses of the optical resonator ($Q = \text{accumulated energy} / \text{lost energy}$) [90, 91].

If the optical resonator is deliberately blocked, the reflected radiation from the mirror is blocked, the losses increase, and thus the Q factor decreases ($Q \approx 1$). Since energy pumping continues, but there is no output, the energy accumulated in the environment increases. As soon as the blockage is removed, laser oscillation starts again and the Q factor increases ($Q \gg 1$). Because the photon population is much larger than the normal threshold, the increased energy density results in a short-duration but high-power pulse. The duration of the pulse is much shorter than the blockage period, during which the photon population increases. During the pulse, the photon population is completely reset, as can be seen in Figure 4.4 [90, 91].

Physically, the Q-switch assembly is a cover that can be controlled to open and close depending on time and is placed between the mirrors [90, 91].

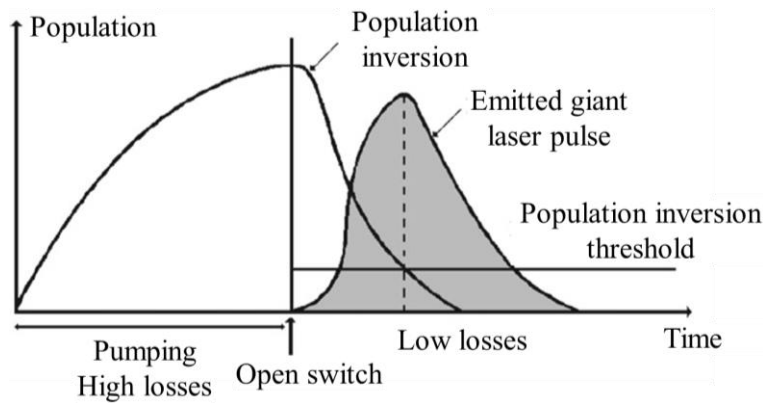


Figure 4.4. Change in photon population [91]

4.1.4 Laser-Material Interaction – Absorption

When the laser beam hits the material surface, some of it is reflected and/or scattered, while the rest penetrates the material, as can be seen in Figure 4.5. A part of the light that penetrates the material is absorbed and some is transmitted. The optical transmission depth of the nanosecond laser is negligible in non-transparent opaque materials, such as metal. It is assumed that there is only surface interaction. The absorbed energy heats the material, increasing its temperature. Depending on the energy density and interaction time of the laser, the material can heat up, melt, vaporize, or form plasma, as can be seen in Figure 4.6 [88, 90].

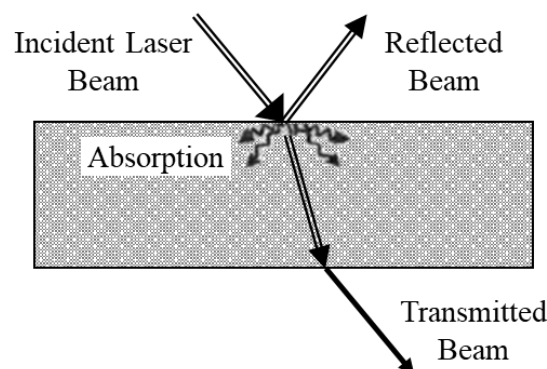


Figure 4.5. Laser beam interaction on the material surface [90]

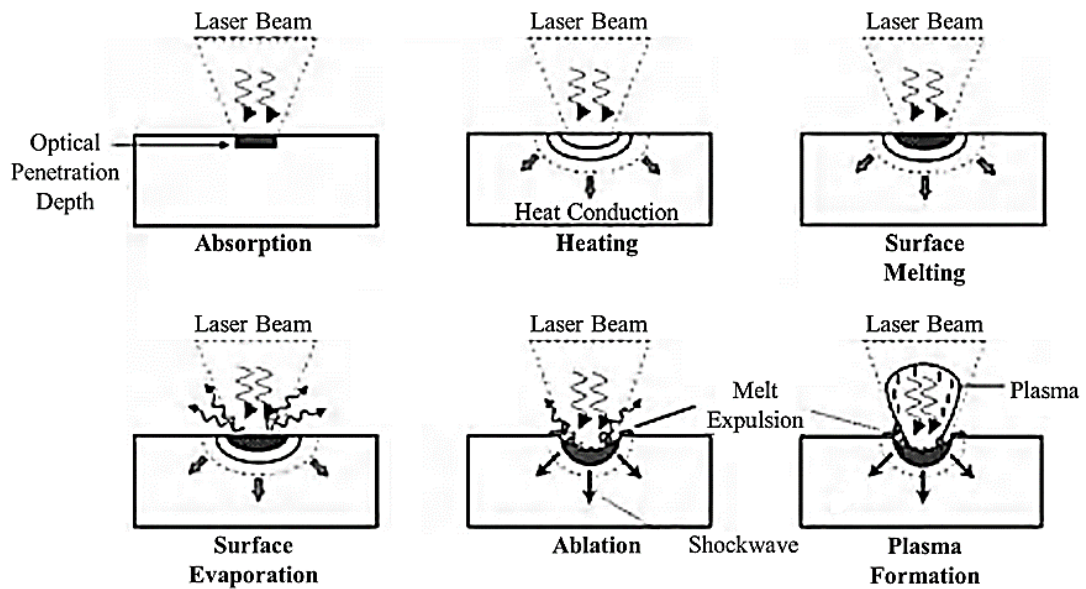


Figure 4.6. Different effects of laser beam absorption on the surface [90]

The energy levels of free or bound electrons determine the absorption property of materials. When we look at the atomic structure of the material, there are electrons in the free state on the surface or in the bound state in the atoms. These electrons contain a large amount of potential energy levels ready to jump. In order for the beam of the laser to interact with the material, the energy of the photon must be equal to or greater than the energy level of the electrons of the material. The electric field (E) of the photon is too low to affect the nucleus of the atom. Therefore, it interacts with free or bound electrons. When the laser beam reaches the surface, the photons collide with the electrons. This interaction between light and material is not yet thermal [92-94].

If the photon and electron vibrations are in resonance (the photon's frequency is the same as the electrons' natural frequency), energy is transferred, the free electrons are accelerated, and the photon's energy is converted into the electron's kinetic energy (the inverse Bremsstrahlung effect). The energy level of the electrons in the atom

risers up to the conduction band (upper orbitals). But the interaction of free electrons is more. In this way, energy is absorbed [87, 92, 95].

Electrons excited in this way have to transfer their excess energy somehow and return to the equilibrium state. The heat spreads from the surface into the material. The heat conduction mechanism is the same as conventional thermal conduction. Excited electrons transmit vibration by colliding with lattice phonons and other electrons, or return to their orbitals and emit radiation (spontaneous emission). The free time of the electrons before they collide with each other in the conductive medium is $\sim 10^{-13}$ (s). Thermal equilibrium is established very quickly [92, 94, 95].

Laser energy interacts only on the surface of metal materials, it cannot pass under the surface [$10^{-4} - 10^{-5}$ (mm)]. That is, the thermal transmission depth is much greater than the optical absorption depth [88, 93, 94].

The thermal conduction depth (δ_{th}) can be represented by the 1D thermal diffusion formula:

$$\delta_{th} = k\sqrt{\alpha\tau_p} \quad (4.3)$$

where k is a coefficient {given as 1 [89, 96], 2 [90,91,93,95,97,98], or 2.36 [99] in different studies}, α is the thermal diffusivity (mm^2/s), which is a material property found by dividing the thermal conductivity by the density and specific heat, and τ_p is the pulse width.

If enough energy is absorbed, since the vibration of the molecules will be high, the residual mechanical strength is lost and the material melts. At higher temperatures, the molecular bonds become looser due to vibration and evaporation occurs (material is removed from the surface). At even higher temperatures, the steam continues to absorb energy and electrons can break away from atoms, forming plasma, as can be seen in Figure 4.7 [100].

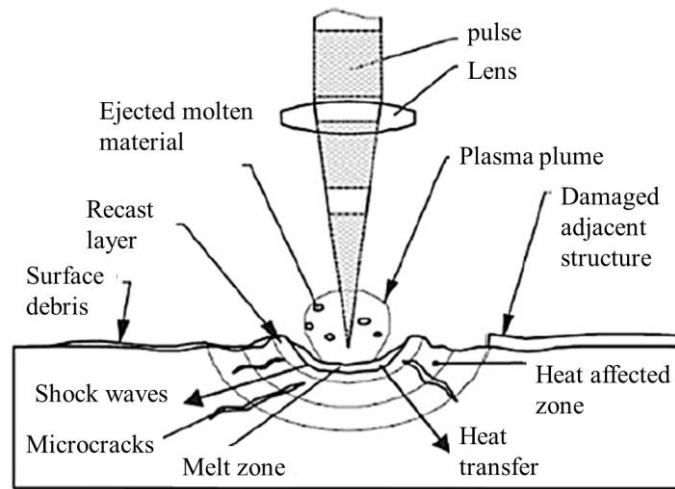


Figure 4.7. Laser-material interaction [100]

Despite its thermal properties, the laser acts much differently than a normal heat source. This is because the laser-induced temperature rise is very localized in space and time. The temperature level of 10000 (K) can be reached in a very small volume defined with the laser focus. Thanks to short pulse times, a heating rate of 10^{15} (K/s) can be achieved. Chemical reaction time remains much slower [97].

4.1.5 Laser-Material Interaction – Reflectivity

An important factor for laser application is surface reflectivity. This value is an optical property of the material and is different for each material. Its value ranges from 0-1 and has no units [92, 93].

The more the vibrational frequencies of the electrons in the material resonate with the frequency of the incoming laser, the more the laser beam is absorbed and transmitted as heat. However, if there is no resonance between the light and the free electrons on the surface, the frequency of the incident light forces them to vibrate in phase and thus the electrons emit light. The electric field is 180° out of phase. The light wave propagates in the direction opposite to the incident light [87].

According to Bass [92], Ion [94] and Svelto [95], the following properties determine the reflectivity value:

- Material composition
- Laser wavelength
- Surface roughness
- Oxidation
- Temperature
- Laser power density
- Laser impact angle on the surface

Reflectivity change as a function of laser wavelength can be seen in Figure 4.8.

In metals, there is less than 10% change in reflectivity value during phase change (solid-liquid). For this reason, the reflectivity can be considered constant in the material removal equations [91]. There is a connection between electrical conductivity and reflectivity. The higher the conductivity, the greater the reflectivity. Electrically conductive metals appear shiny because they reflect light [89, 90, 95].

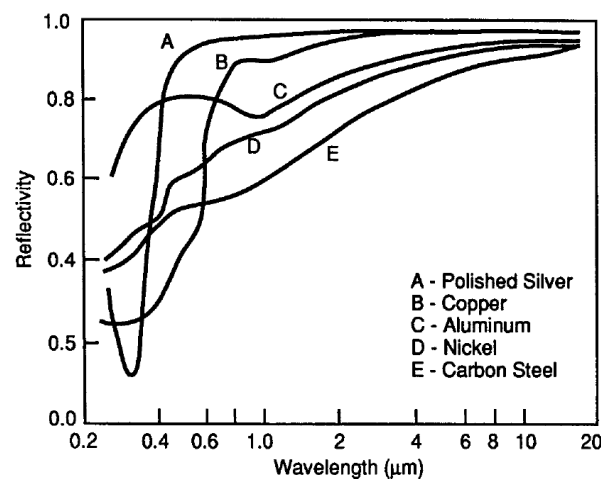


Figure 4.8. Reflectivity as a function of wavelength for several metals [93]

4.1.6 Laser Power Density

The power divided by the area applied (W/mm^2) gives the *power density* value. The most important parameter in laser-material interaction is the power density. This value affects the material removal mechanism along with the pulse width [92-94]. Figure 4.9 shows different laser-material interaction regimes. Laser assisted fabrication can be grouped as can be seen in Figure 4.10.

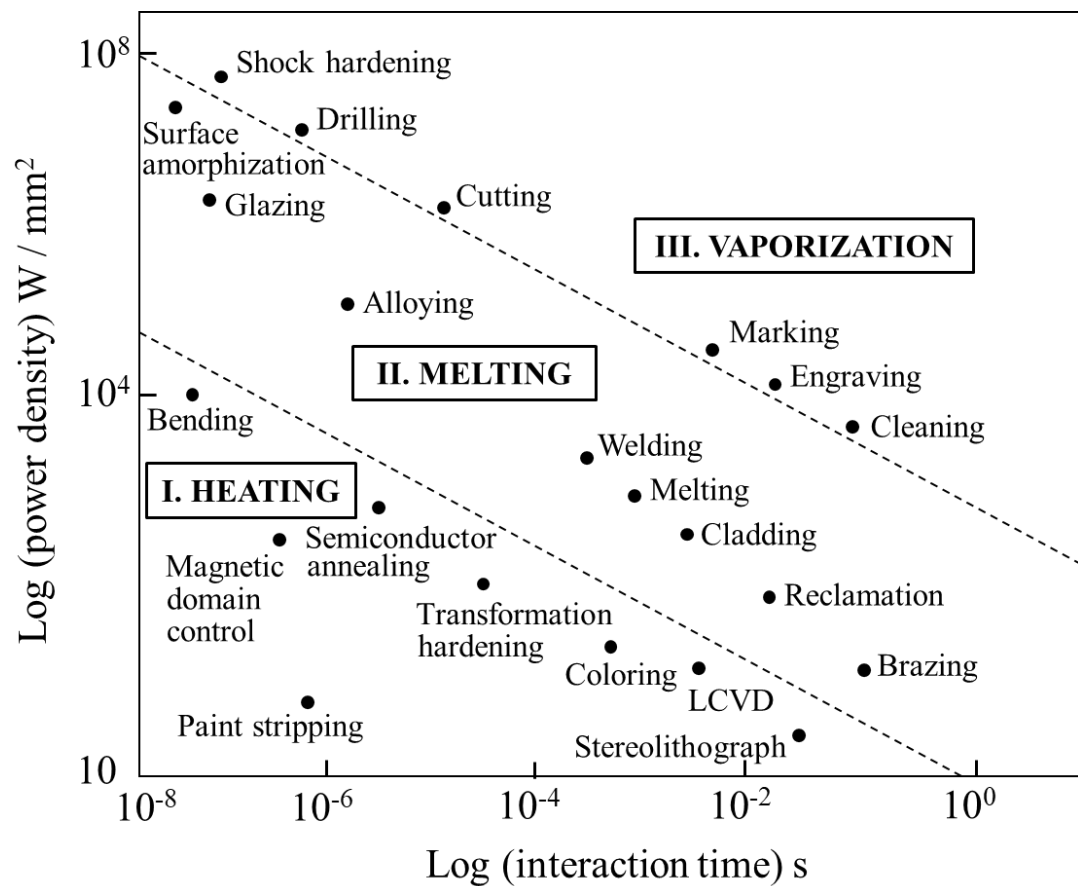


Figure 4.9. Different laser-material interaction regimes [90]

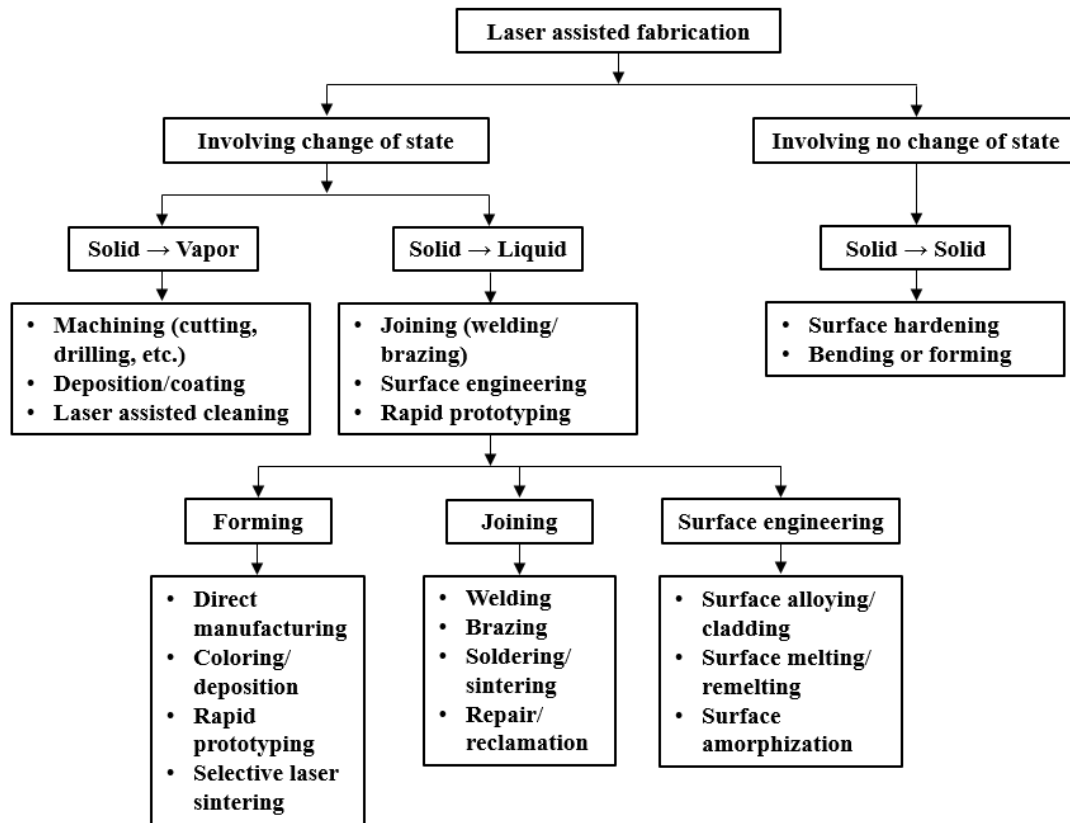


Figure 4.10. Classification of laser assisted fabrication [90]

When the high-power laser beam is focused on a small spot, it interacts with the material. The absorbed radiation is converted into heat and the material is removed [power density $> 10 \text{ (kW/mm}^2\text{)}$]. For operations such as cutting/drilling, the power density must be high enough to remove material, but if it is too high gas/optical breakdown (ionization) will occur and the laser will be absorbed and reflected somewhere above the workpiece (plasma absorption/shielding) [88, 92, 93, 95].

4.1.7 Material Removal Model

A liquid-vapor model is available that describes material removal, as can be seen in Figure 4.11. According to this idea, the material is removed as both liquid and vapor (melting + vaporization). However, the liquid-vapor ratio decreases as the power

density of the laser increases. At a limit point the model evolves into a solid-vapor model (the material skips the liquid phase very quickly and evaporates directly from the solid). This approach is suitable for Q-switched (pulsed) lasers. When high power density and short pulse width are applied, the evaporation temperature at the surface can be reached very quickly with less energy applied [90, 92, 93, 96].

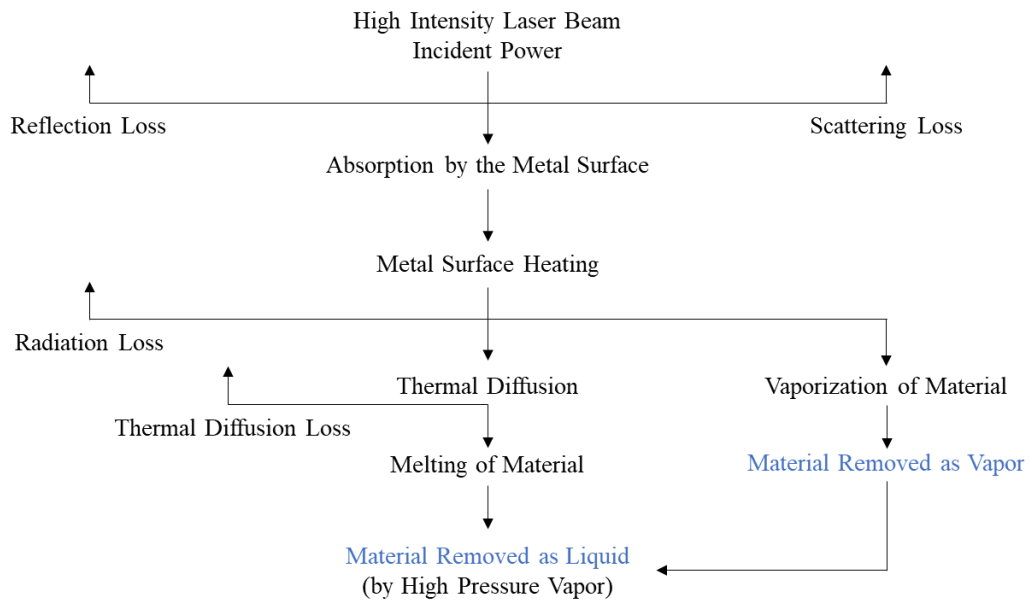


Figure 4.11. Material removal [92]

4.1.8 Vaporization Mechanism

According to the vaporization approach, the laser energy heats the material above its boiling point at high power density [$\sim 1 \text{ (MW/mm}^2\text{)}$] and material is ejected as vapor from the machining zone. The steps are as follows: [92-95]

1. The laser beam reaches the surface and the photons collide with the electrons.
2. Some of it is reflected, the rest is absorbed.

3. The surface temperature rises to the boiling point very quickly, so melting due to thermal conduction is largely prevented.
4. With the pressure [$\sim 10^2$ (bar)], the vapor is rapidly [$\sim 10^3$ - 10^6 (cm/s)] separated from the surface. Evaporated material goes into the air.
5. The recoil pressure of the ejected vapor drags the molten material and eroded particles from the surface (melt ejection) and thus a cavity is formed. The assist gas flow used also helps to expel the molten material.
6. The recoil force of the vapor leaving the surface creates a shock wave on the material surface. Grains near the surface may shift locally and surface hardness may increase.

Looking at the thermal zone around the hole, there is a steep gradient of temperature, causing locally high mechanical stress [$\sim 20,000$ (MPa)]. As if a point load is applied, a stress field is formed and this stress is transmitted to the material as a wave. This short-term [10^{-9} - 10^{-3} (s)] interaction, which is similar to a local knock, does not cause damage to ductile metal materials, but the impact of knocking is reflected inside the material, creating a chipping effect in brittle materials [92].

If the vapor leaving the surface is hot enough, it starts to reflect, scatter, or absorb the incoming laser beam (plasma shielding) because it has a high electron density (ionization). Particles smaller than the wavelength of light scatter the light (eng. Rayleigh scattering) or electrons absorb photons (inverse Bremsstrahlung). This phenomenon depends on the material type and is seen at high power density. For this reason, the optimum power density must be decided [88, 96].

4.1.9 Plasma Effect

When a single high-power laser pulse is considered, the initial sharp power rise triggers the formation of evaporation of the material. Since plasma is formed and interrupts the energy, the evaporation rate decreases for a certain period. Due to the

decreasing power towards the end, the plasma weakens and evaporation from the material continues. This effect can be seen in Figure 4.12 [92, 93].

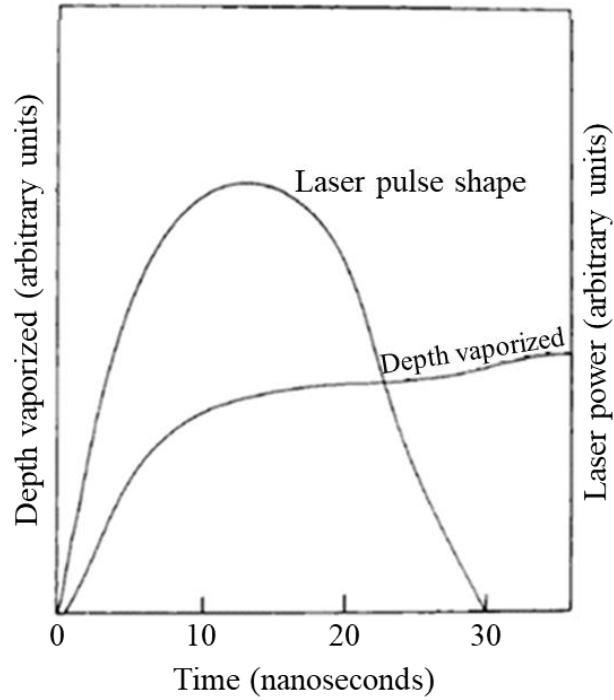


Figure 4.12. Effect of a single pulse [93]

When plasma is formed, only a certain amount of laser energy can reach the surface. It can be represented by the following formula:

$$E_s = E_{las} e^{-\tau} \quad (4.4)$$

where E_s is the energy that can reach the surface, E_{las} is the energy of the incoming laser beam, and τ is the optical loss coefficient of the plasma (depends on laser wavelength and the electron density in the plasma) [95].

If the electron density in the plasma is high enough, the absorption will be too great and laser beam cannot reach the surface. For this to happen, it is necessary to reach the temperature values of 10,000–30,000 °C [89]. There is a critical level of electron

density [electrons per (cm³)], where the plasma completely blocks the laser beam, as can be seen in Figure 4.13 [95].

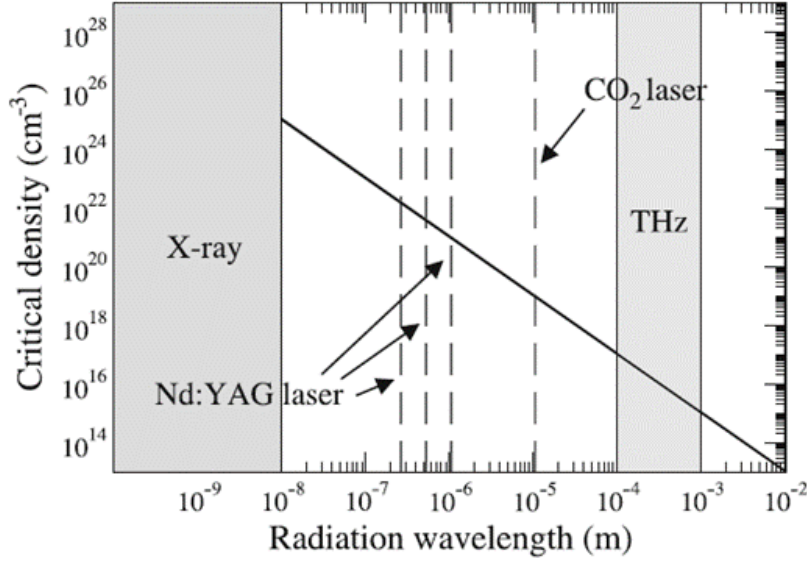


Figure 4.13. Critical density vs radiation wavelength [95]

4.1.10 Energy Balance

The amount of material that can be removed by the evaporation mechanism against the energy applied to the material can theoretically be calculated considering the energy balance [88, 93, 96].

First, the laser energy level should be checked to see whether it is sufficient to the start evaporation. The threshold fluence can be considered [91, 95].

$$\varphi \geq \varphi_{th} \approx \rho \Delta H \delta_{th} \quad (4.5)$$

where φ is the fluence (amount of energy applied per unit area – E_p/A , where E_p is the laser pulse energy, and A is the area of the laser beam), φ_{th} is the threshold fluence, ρ is the density, ΔH is the vaporization enthalpy of the material, and δ_{th} is the thermal penetration depth as given in Equation (4.3).

And the laser pulse energy (E_p) can be calculated as:

$$E_p = P/f \quad (4.6)$$

where P is the laser power and f is the frequency.

According to Ready [88, 93] and Kannatey-Asibu [96], the energy balance equation can be set up as follows:

$$[C_p(T_v - T_0) + L_f + L_v]\rho d_v \pi D^2/4 = (1 - R)E_p \quad (4.7)$$

where C_p is the specific heat of the material, T_v is the vaporization temperature of the material, T_0 is the room temperature, L_f is the melting energy of the material, L_v is the vaporization energy of the material, ρ is the density, d_v is the depth of material removal per laser pulse, D is the laser beam diameter, R is the reflectivity coefficient, and E_p is the laser pulse energy.

Assumptions in order to use the above equation:

- Only the vaporization mechanism is active (no melting or ionization)
- The material specific heat value is constant during heating
- Material density is constant during heating
- The amount of reflectivity is constant throughout the heating
- Very low losses (no scattering, conduction, convection, or radiation)

This equation works well at energy levels close to the threshold fluence value, as some assumptions neutralize each other's effects.

4.1.11 Effect of Auxiliary Gas

In laser applications, assist gas is generally used. The reasons, which are given in [94, 96], are as follows:

1. To disperse the formed vapor and plasma by blowing and thus enabling the laser to reach the target.
2. Protecting the processing area and isolating it from the environment or accelerating the exothermic reaction
3. Protecting the focusing lens from splashing material
4. To be able to remove molten material before freezing in the processing zone
5. Reducing the HAZ in the material by creating a cooling effect in the machining area

Inert gases (Ar, He, N₂) or reactive gases (air, O₂) can be preferred as auxiliary gases. Argon is cheaper and denser, so it better seals the processing area and provides protection. Helium is preferred if the laser has a higher power density or takes longer to focus in the same region (such as piercing), because it has greater thermal conductivity and is more difficult to ionize (less plasma loss). Reactive gases such as oxygen, on the other hand, increase the exothermic reaction in the material to achieve higher cutting speeds, but lower cut quality.

4.1.12 Quality Issues

Since LBM is a thermal process, there is always some recast and HAZ formation on the machining zone, depending on the energy level and pulse width (Figure 4.14).

Recast layer:

When the laser pulse ends, the cooling cycle begins. The time remaining for cooling (the time between laser pulses) is longer than the duration of the laser pulse. During this time, all the molten material cannot be ejected and re-solidifies on the inner wall surface. The microstructure is different compared to the base material [92]. The mechanism can be summarized as follows:

1. When the laser beam hits the surface for the first time, a sudden hole formation begins. The shape of the cavity formed as a result of the laser pulse is conical.
2. The edges become steeper and while vaporization continues on the surface, melting occurs at the edges.
3. When the power density on the surface fails to maintain its vaporization state, liquid (molten material) is formed at the bottom of the hole. This liquid oscillates and moves while trying to minimize surface tension. The liquid moves up and down the hole and solidifies as it cools. Due to these chaotic movements, depth and recast layer thickness variation may occur in the hole.

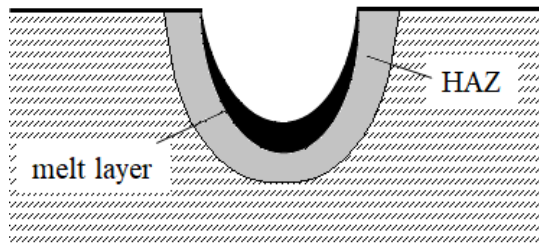


Figure 4.14. Recast and HAZ

Heat affected zone (HAZ):

The heat effect of the laser pulses may not be localized under all conditions, and in this case the heat is radiated into the material. This causes microstructure changes in the regions where heat is transmitted in the material. This region is called the HAZ for short. The width of the HAZ zone is determined by the laser pulse duration, laser energy, laser frequency, and material properties [97].

4.1.13 Summary

As given in [97], important mechanisms in laser material removal are as follows:

1. Optical excitation of electrons in the material
2. Dissipation of energy in the form of heat
3. Phase change of the material

As given in [93], important material properties are as follows:

1. Reflectivity coefficient – determines how much the laser beam is absorbed at the material surface
2. Thermal diffusion coefficient – determines how much of the generated heat is transmitted into the material
3. Vaporization enthalpy – determines how much energy is needed to vaporize the material

Similarly, important laser parameters for a single pulse are as follows:

1. Wavelength – determines how much laser energy is absorbed by the material [93].
2. Power density – how much laser power is applied per unit area affects the material removal mechanism. Certain values must be chosen to achieve the desired vaporization mechanism in hole drilling [93].
3. Pulse width – how long the laser is applied to the surface determines how much heat is transmitted into the material. If it is too long, thermal conduction loss and melting will be high. If it is too short, the surface temperature will be higher, most of the energy will be spent on heating the vaporized material and the penetration depth in the material will be less [88, 89, 97].

In the laser-material interaction, vaporization as a result of absorption on the surface and dissipation of the molten material with the recoil pressure of the vapor causes

the material to be removed. Reflection, thermal losses, and plasma formation are the effects that reduce the amount of material removal. Experimental observation is essential to study laser material removal and to determine the optimum process window of laser parameters [93].

4.2 Water Jet Guided Laser Material Removal Mechanism

WJGL is a technology that combines water jet and laser beam. The water jet acts like a fiber that carries the laser to the machining zone. In this way, the focusing, cooling, and cleaning capabilities of the water are utilized. There are quality advantages over LBM machining (lower recast and HAZ layers, etc) [101-103]. Figure 4.15 shows the general working principle.

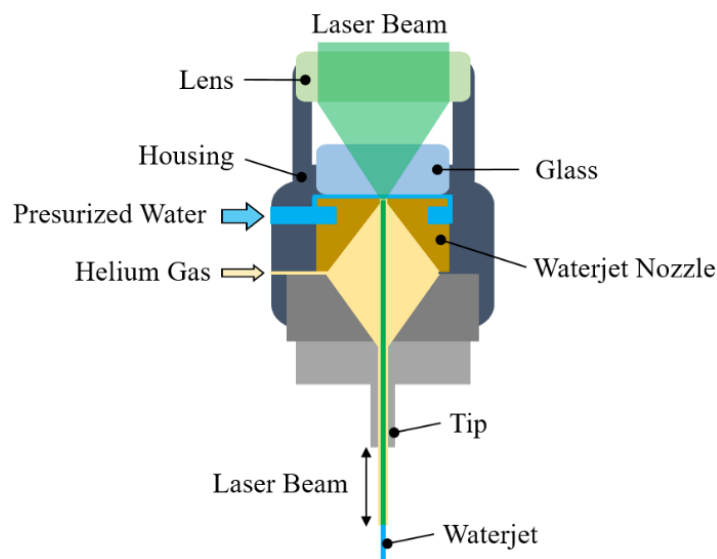


Figure 4.15. Working principle of WJGL

The material removal mechanism is basically similar to LBM. The energy source is the laser beam. The laser pulse is generated as described in the LBM. The surface interaction (photon-electron interaction, absorption, and reflection) is the same.

Vaporization (and partial melting and ionization) occurs due to the power density level used. The energy balance approach is still valid. The use of energy balance is actually more convenient than LBM, because the power distribution at the focal point is equal and each condition is the same as the previous one, since the temperature in the processing zone does not increase due to the cooling of the water in between the laser pulses [62].

However, the auxiliary gas has been replaced by a water jet. Although water is more effective than gas in removing melt and cooling the machining zone [101, 104], the mechanism of water jet formation, the coupling mechanism of the water jet and laser, and the transportation of the laser in the water should be examined separately to better understand the process. In addition, instead of the *laser-solid* interaction in the processing region, the *laser-liquid-solid* interaction should be investigated [105].

4.2.1 WJGL Laser Properties

Although there are a variety of systems available in the market, the below information is valid for the machine that is used in the thesis study.

- Laser type is a diode pumped Nd:YAG solid state laser. It is preferred because its pulsing properties are very good.
- Installed laser power is 100 (W). It is preferred to keep the power density at vaporization level.
- Wavelength is 532 (nm) (visible green light). It is preferred because its absorption in water is very low.
- Pulse order is at nanoseconds level. It is preferred to keep the power density again at vaporization level.

The parameters can be seen in Table 4.1. Q-switch parameters are the number of blockages per second (frequency) and duration of each blockage.

Table 4.1 Laser Parameters

Laser Input Parameters	Value Range
Diode power level	48.5-82.5 %
Q-switch blockage duration	0.02-8.00 (μ s)
Frequency	6-60 (kHz)
Laser Output Parameters	Value Range
Laser Power	0-40 (W)
Pulse Width	50-500 (ns)

4.2.2 Water Jet Properties

The below parameters are valid for the machine that is used in the thesis study.

- Nozzle diameter: Ø40-60 (μ m)
- Nozzle material: Sapphire or diamond
- Water properties: Deionized, purified, and degassed
- Water pressure: 50-500 (bar) [80-250 (m/s)]
- Assist gas: Helium 0-2 (l/min) (to increase the stable length of the water jet)

Deionized, purified, and degassed water is used with reverse osmosis, UV lamp, filter, and vacuum membrane system. This is to make sure there are no substances or bubbles in the water that could disrupt the laminar water flow, absorb/reflect/scatter laser energy, stick to the laser glass, or damage the nozzle [66, 101, 106]. The quality of water is measured by its resistivity. Expected value is 17 (M Ω cm) or higher before starting the process [resistivity is 18.2 (M Ω cm) for ideal pure water].

Water consumption is quite low [\sim 1-1.5 (l/hour)]. Therefore, no recycling is required [106, 107]. The force exerted by the water jet on the material surface is very low [\sim 0.1 (N)]. The water jet does not have a direct mechanical effect (chipping, cracks,

etc.) on metals while processing [107, 108]. The formula for calculating the impact force (F_{imp}) is: [105]

$$F_{imp} = \frac{\pi}{4} D_j^2 \rho U^2 \quad (4.8)$$

where D_j is the diameter of the water jet, ρ is the density of water, and U is the speed of the water jet.

The nozzle used is round and with sharp corners. The reason for this is to create a discrete flow from the side wall. The flow of high-pressure water cannot follow the sharp corner of the nozzle and becomes narrower. This effect is known as the *vena contracta* effect, as can be seen in Figure 4.16. The newly obtained water jet diameter after passing through the nozzle is found by the formula [109, 110]:

$$D_j = \beta D_{nozzle} \quad (4.9)$$

where β is the contraction coefficient (typically 0.83) (which depends on the nozzle diameter and the radius of the sharp corner and is found experimentally), and D_{nozzle} is the diameter of the nozzle.

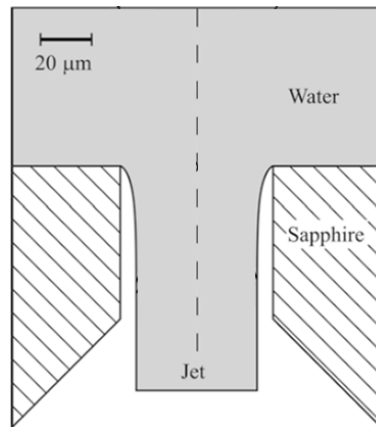


Figure 4.16. *Vena contracta* effect [109]

If there is no contact with the side wall as a result of this narrowing, the water jet comes out with a smaller cross-sectional area (eng. hydraulic flip). In this way, a longer stable water jet is obtained [105].

If there was no narrowing, the laser directed into the water would damage the nozzle in a short time. The surface tension of the exiting water provides the minimum surface energy level and therefore it has a round cross section. The fluidity of water also provides resistance to other changes in shape.

The stages from *vena contracta* to the formation of *hydraulic flip* are shown in Figure 4.17 and explained below: [105]

1. When the flow rate reaches a sufficient state, contraction begins.
2. The flow adheres to the wall of the nozzle again before leaving the nozzle and an air gap is formed in between.
3. The local static pressure is lower than the vapor pressure of water. Bubbles can form in the water, but these bubbles combine with the gap and the gap continues to grow.
4. The cavity eventually opens up to the atmosphere and the water jet is completely separated from the nozzle wall. Laminar flow is obtained at the nozzle outlet.

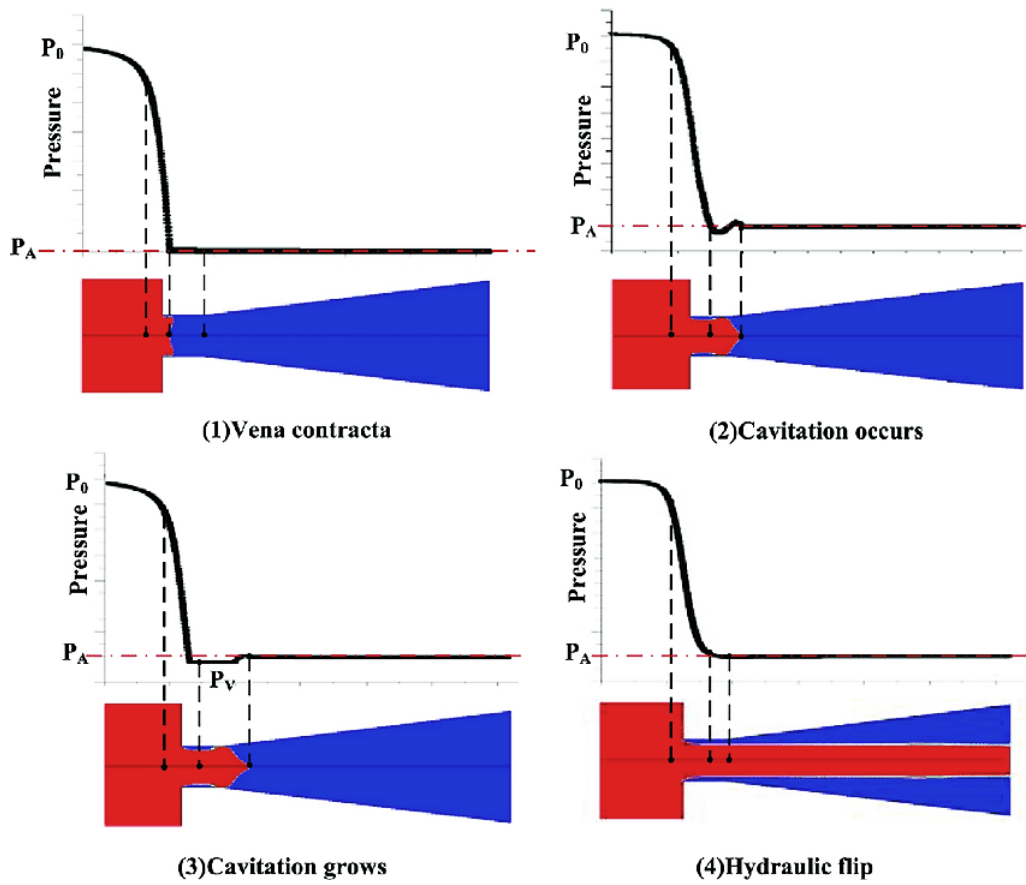


Figure 4.17. Formation of the hydraulic flip [105]

Hydraulic flip will not occur if the nozzle corner is not sharp, the nozzle is too long, or the pressure is not enough. In this case, there is no water jet formation. These situations are shown in Figure 4.18.

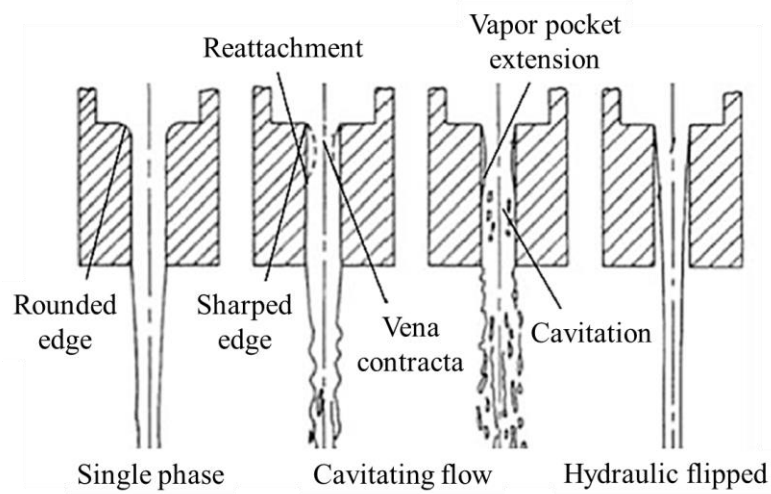


Figure 4.18. Different flow conditions [105]

Even if the water jet is obtained as stable, it naturally deteriorates after a certain distance (gravity, atmospheric conditions, velocity profile change, etc.). The desired stable distance should be adjusted with the nozzle diameter and water jet velocity (or pressure) (Figure 4.19).

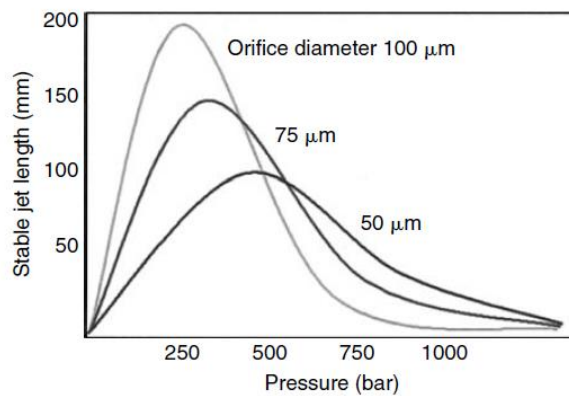


Figure 4.19. Stable jet length vs Pressure [108]

The velocity of the water (U) exiting the nozzle is independent of the nozzle diameter and depends on the pressure. It is calculated by the following formula (Bernoulli's principle) [109]:

$$U = K \sqrt{\frac{2\Delta P}{\rho}} \quad (4.10)$$

where K is the nozzle loss coefficient (typically 0.94) (The ideal theoretical speed cannot be reached due to friction and turbulence. The value is found experimentally), ΔP is the water and ambient pressure difference, and ρ is the density of water.

After the water jet leaves the nozzle, the laminar flow is disrupted after a certain distance due to the initial disturbances and droplet formation begins. The distance between the nozzle and the point where the dispersion starts is called the breakup length (L_b), as shown in Figure 4.20. This distance normally shows fluctuation in time and space [109].

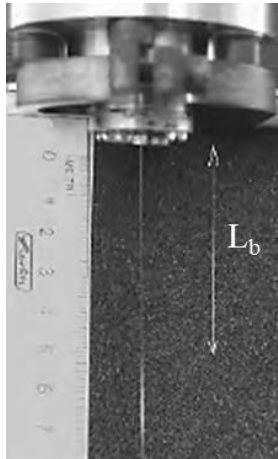


Figure 4.20. Jet breakup length [103]

Nozzle geometry, water density, surface tension, temperature, and aerodynamic factors affect this value. However, in all cases, a behavior as shown in Figure 4.21 is observed depending on the water output velocity [111, 112].

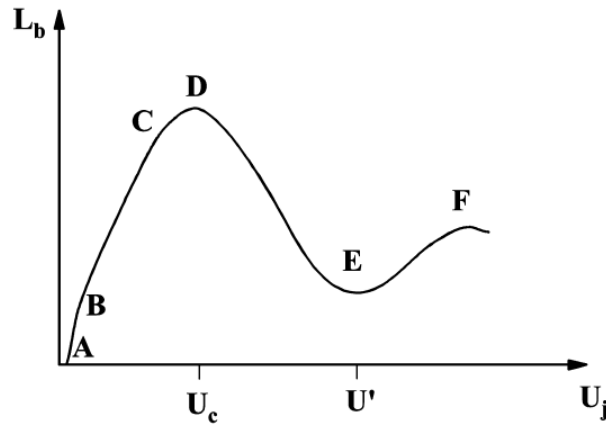


Figure 4.21. Jet breakup length vs Mean jet velocity [111]

The explanation for the plot is as follows: [111]

- Beyond the initial velocity (AB), L_b increases linearly with velocity (BC). There is a laminar flow due to the surface tension of the water. Oscillations growing towards the end of the stream form a droplet larger than the diameter of the water jet and dispersion begins. This region is called the *Rayleigh breakup regime*.
- The dynamic effects of the surrounding gas flow in the (CD) region can no longer be ignored. A critical velocity is reached, giving the longest distance (U_c). This speed varies depending on the type of gas used and the nozzle shape.
- L_b decreases in the (DE) region. This region is called the *wind-induced regime*. The dispersion point of the water is determined by the disturbance caused by the gas used. Fluctuations like a sinusoidal curve are observed on

the surface. In the region up to point E, the fluctuation on the surface increases exponentially, eventually causing droplets of the same diameter as the water jet.

- At higher speeds (EF) L_b starts to increase again. Due to friction with the surrounding air, the wavelength of the ripples on the surface becomes considerably shorter, becoming smaller than the nozzle diameter. The turbulence in the water also begins to take effect. L_b becomes difficult to measure because droplets smaller than the water jet begin to break off from the water jet surface before they reach the distance L_b .
- From point F, spraying starts at the nozzle and the water jet completely disappears. This is the atomization zone.

The machine used in the study works until point D.

Depending on the exit velocity, the stable water jet distance can be calculated approximately as follows based on the water jet velocity: (Gravity and gas effects are ignored) [108]

$$L_b = Ut_b \quad (4.11)$$

$$t_b = \frac{1}{\beta_{max}} \ln\left(\frac{r_{jet}}{\delta_0}\right) \quad (4.12)$$

$$\beta_{max} = 0.34 \sqrt{\frac{\sigma_w}{\rho R_0^3}} \quad (4.13)$$

where L_b is the stable water jet length, U is the water jet speed, t_b is the time required for a disturbance in jet radius to grow, β_{max} is the frequency of most rapidly growing disturbance, r_{jet} is the radius of the water jet, δ_0 is the amplitude of the initial disturbance (taken as 10^{-3} - $10^{-4} R_0$ for practical calculations), σ_w is the surface tension of water, and ρ is the density of water.

4.2.3 Effect of Gas

Helium gas is used to isolate the water jet from the aerodynamic effects in the environment and to keep its stable length longer. Helium gas is sprayed coaxially around the water jet, as can be seen in Figure 4.22 [113, 114].

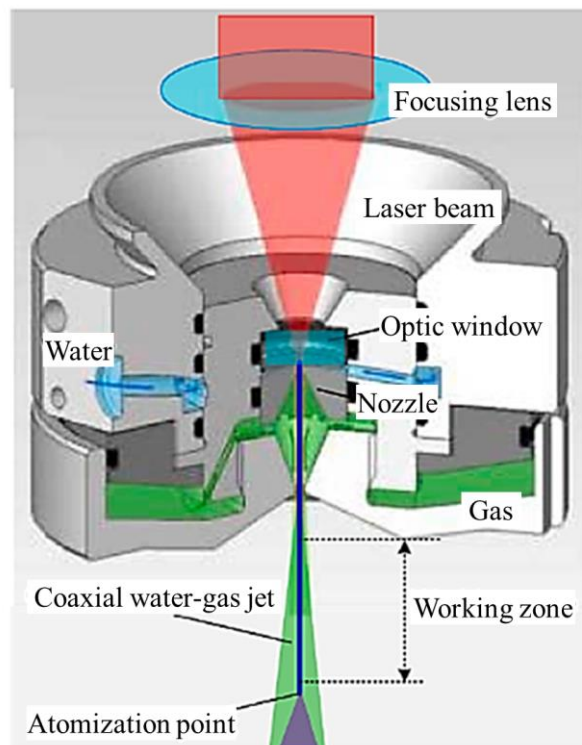


Figure 4.22. Gas-water jet interface [105]

The reasons for choosing Helium in particular: [113]

- Very light (heavy gases disturb the water jet earlier)
- Density is less than air (does not settle down)
- Non-explosive
- Non-toxic

- Thermal conductivity is high (difficult to ionize)
- Refractive index is less than water, approximately same as air (≈ 1)

An experiment performed with Helium gas is shown in Figure 4.23. Experimental conditions in the photo: 36 (μm) nozzle, 140 (MPa). A: Helium off, B: Helium flow [1.68 (l/min)], C: Helium flow [4.14 (l/min)] [113].

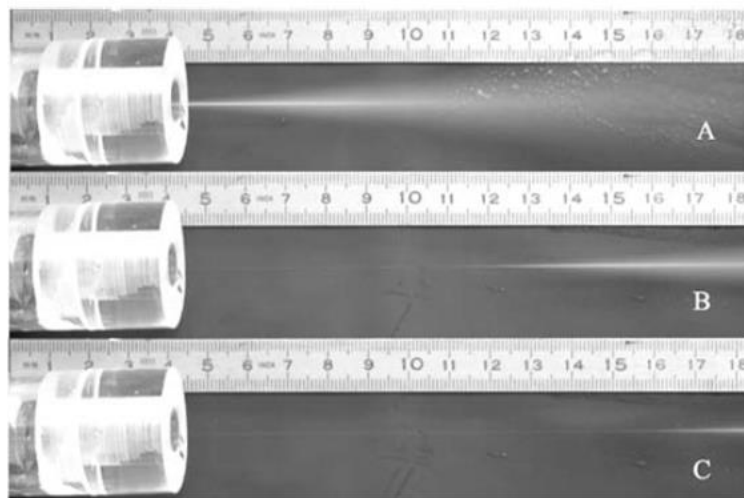


Figure 4.23. Jet surrounded by helium stream [113]

With the use of helium gas, since the stable distance of the water jet is longer, processing can be done from a farther distance and/or deeper cuts can be obtained, as can be seen in Figure 4.24.

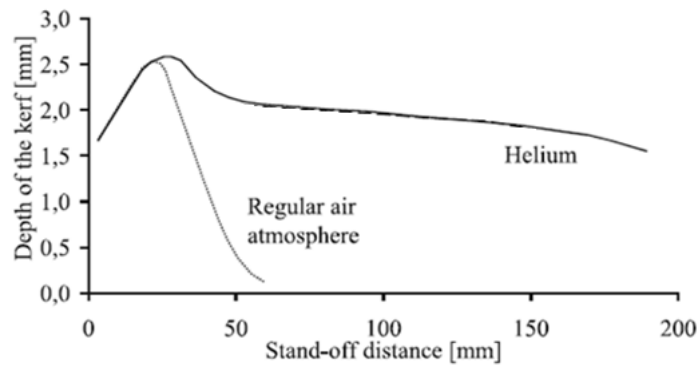


Figure 4.24. Depth vs Stand-off distance [113]

4.2.4 Laser-Water Jet Coupling

A special unit has been designed to direct the laser beam through the water jet. In order to prevent water from escaping, but to allow the laser beam to pass, there is a glass-enclosed, symmetrical axis chamber with dynamic water flow. The laser beam is focused on the water jet nozzle with the help of the lens. While focusing the laser beam, it passes through glass and water, as can be seen in Figure 4.25 [104].

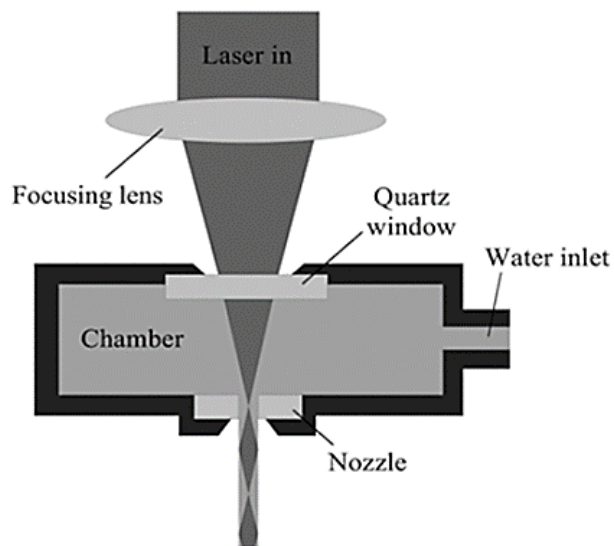


Figure 4.25. Laser-water jet coupling [111]

The combination of water and high power laser does not cause the temperature of the water to rise and/or boil. Looking at the absorption spectrum of water in Figure 4.26, one can see that there is no absorption loss at 532nm wavelength and an almost perfect transmission is provided [74, 107].

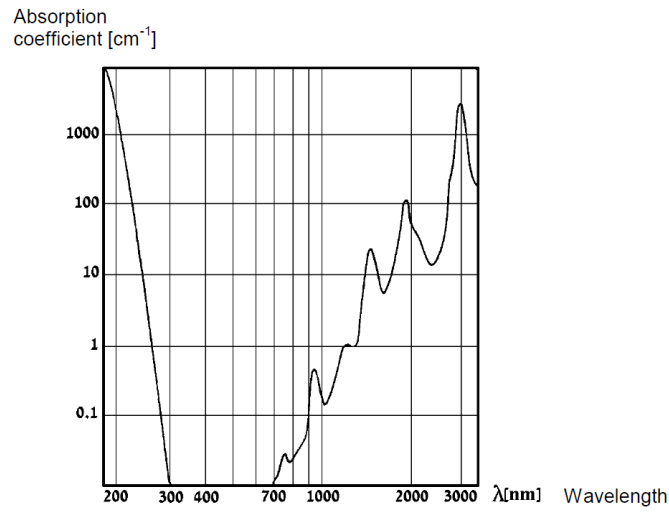


Figure 4.26. Optical absorption spectrum of water [106]

Water jet acceptance angle for the laser beam can be seen in Figure 4.27. There are two basic conditions for the laser beam to enter the water jet properly: [115]

1. The laser focus diameter should be smaller than the water jet diameter:

$$d_{laser} < d_{core}$$

2. The laser angle must be smaller than the acceptance angle of the water jet:

$$\theta_{laser} < \theta_{max} = 2\sin^{-1}(NA)$$

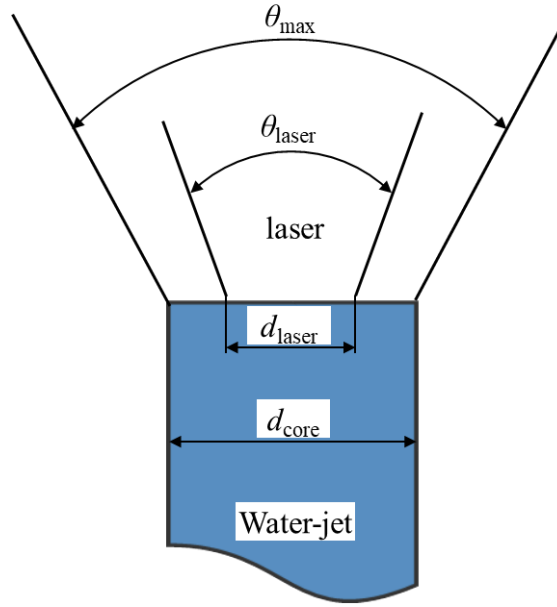


Figure 4.27. Water jet acceptance angle for the laser beam [115]

In optics, each waveguide has a certain angle of acceptance for light. This angle is calculated with a value known as the *numerical aperture* (NA). The NA value defines the condition required for the light traveling in a medium to be completely reflected from the walls. In other words, it is the ability of a fiber to collect light.

NA value is calculated with the difference of refractive index. The refractive index is an experimentally found unitless value that gives the ratio of the speed of light traveling in a vacuum and the speed of light traveling through the material. The water jet has a large NA , which makes the acceptance angle large (123.6°) [105]:

$$NA_{waterjet} = \sqrt{n_{water}^2 - n_{air}^2} = 0.881 \quad (n_{water}=1.333, n_{air}=1) \quad (4.14)$$

$$\theta_{max} = 2 \sin^{-1}(NA) = 123.6^\circ \quad (4.15)$$

If the NA is not selected correctly, the laser will go out of the water jet and damage the nozzle sidewalls, as can be seen in Figure 4.28 [114].

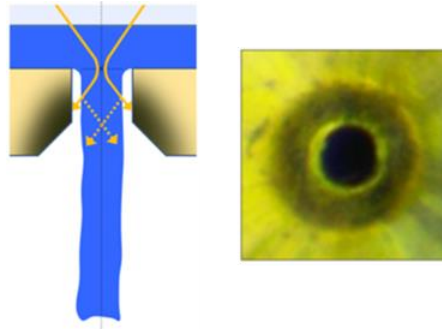


Figure 4.28. Nozzle damage [114]

The focal diameter of the laser can be adjusted in the range of $\varnothing 12.5\text{-}50\text{ }\mu\text{m}$. The laser focus diameter should be smaller than the nozzle diameter to avoid damaging the nozzle [101]. The laser focus diameter is $\sim 35\text{ }\mu\text{m}$ on the utilized machine. In other words, the machine is suitable for the use of minimum $\varnothing 40\text{ }\mu\text{m}$ nozzles.

It is very important to focus the laser in the right place and correctly. Otherwise, due to the misaligned adjustment, high amount of energy comes to the nozzle surface and the power level directed into the water jet decreases, as can be seen in Figure 4.29. The nozzle may absorb the laser beam and the laminar water flow may be disrupted due to the heat generated in the area. Eventually, the nozzle becomes damaged and unusable [109, 116].

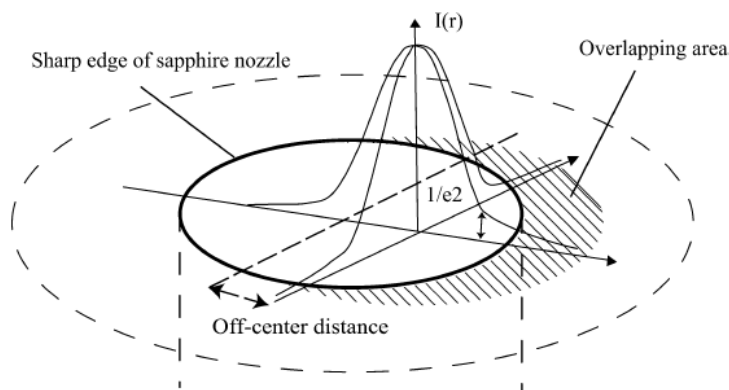


Figure 4.29. Misalignment problem [109]

Alignment error can occur in the d , s , and θ directions (lateral misalignment, vertical misalignment, angular misalignment), as can be seen in Figure 4.30. If the alignment is done correctly and checked regularly, the nozzle life will be long (several months) [101].

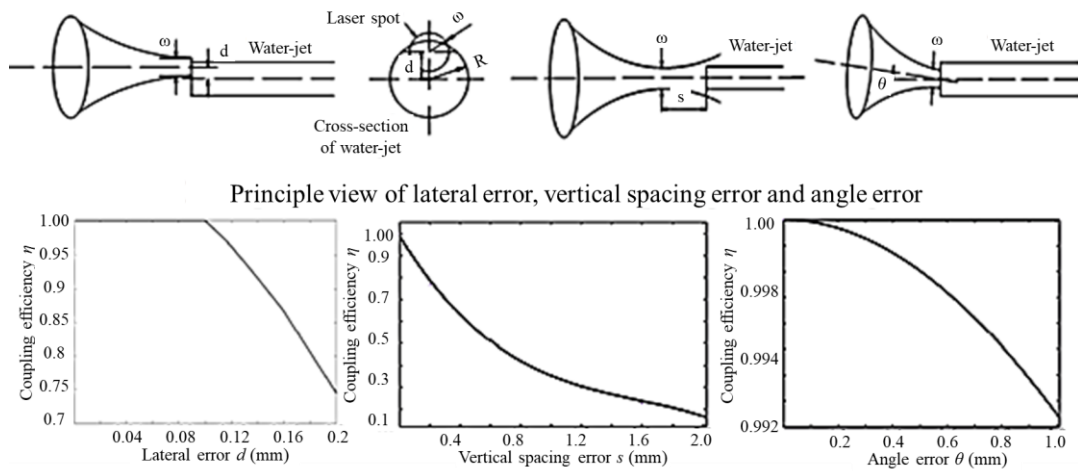


Figure 4.30. The relation of coupling offset error and coupling efficiency [116]

4.2.5 Laser Propagation in the Water Jet

When the laser beam enters the laminar flow water jet, it is reflected due to the refractive index difference at the air-water interface. Therefore, the water jet behaves like a cylindrical waveguide along its stable length. The laser completely fills the water jet as can be seen in Figure 4.31. The laser power profile obtained in this way in water is called *flat-top* or *top-hat*. The energy distribution in the section is uniform [4, 101, 104].

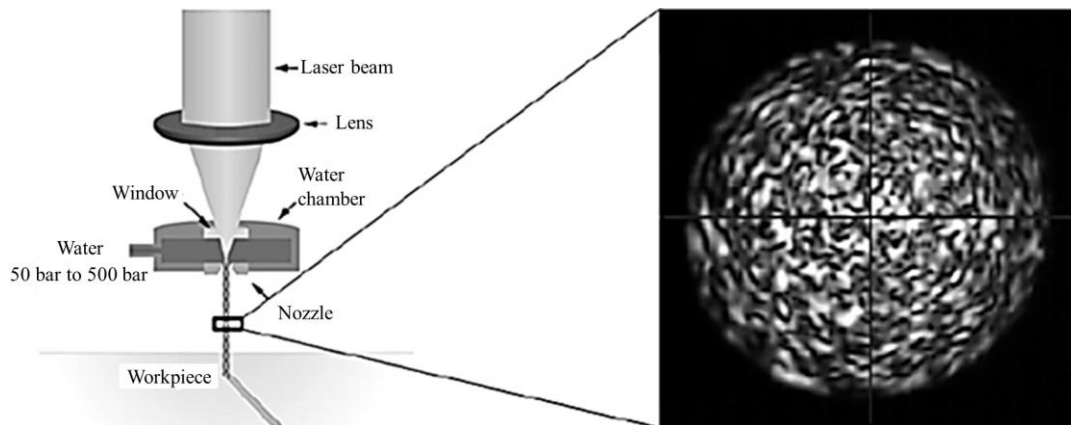


Figure 4.31. Laser beam profile in the water jet [112, 117]

Although there is no laser beam absorption in water, the laser power decreases continuously along the water jet due to scattering by impurities, bubbles, and irregularities in the water jet-air interface in the water. In addition, some nonlinear effects such as Raman scattering are also important [4].

4.2.6 Raman Scattering

Raman scattering is an effect that occurs spontaneously or stimulated. When a material is illuminated with light, the scattered light is emitted at different frequencies than the incident light. This is spontaneous Raman scattering, as can be seen in Figure 4.32. It is a weak effect. Only $1/10^6$ of the incident light wave is scattered at a different frequency at a distance of about 1 cm. The frequency can be less or more. In addition, the scattering is spread over a wide area [118].

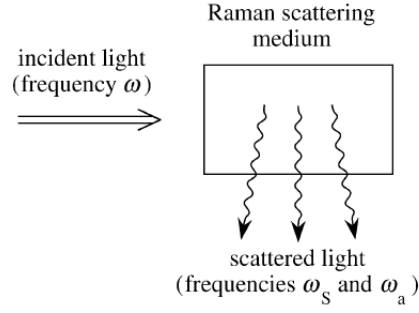


Figure 4.32. Spontaneous Raman Scattering [118]

However, stimulated Raman scattering is seen against a strong stimulus such as laser. 10% or more of laser energy reduces frequency. Scattering occurs in a narrow range along the direction from which the light comes, as can be seen in Figure 4.33.

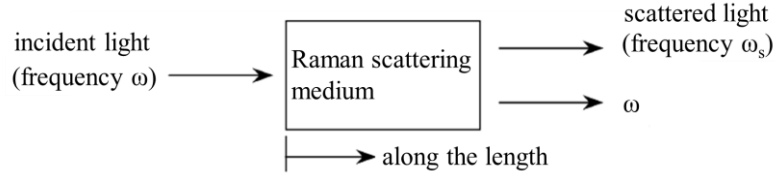


Figure 4.33. Stimulated Raman Scattering [118]

4.2.7 Laser Power Attenuation in the Water Jet

The laser power density used in the WJGL process is suitable for creating Raman scattering in the water medium [4, 116]. Raman scattering, which occurs as a result of the interaction of the green laser and the water jet, causes a shift in the beam frequency and a certain percentage of the beam is shifted to the red color [653 (nm)], as can be seen in Figure 4.34. It was found that at high laser power density [~ 1.3 (GW/cm²)], 26.7% of the green light is shifted to red light. Red light is scattered in all directions inside the water jet. The energy reduction per photon can be calculated with the following formula [4]:

$$h(f_g - f_r) \quad (4.16)$$

where h is the Planck's constant [$6.62607004 \times 10^{-34}$ (Js)], f_g is the frequency of green light [$\sim 5.66 \times 10^{14}$ (Hz)], and f_r is the frequency of red light [$\sim 4.62 \times 10^{14}$ (Hz)].

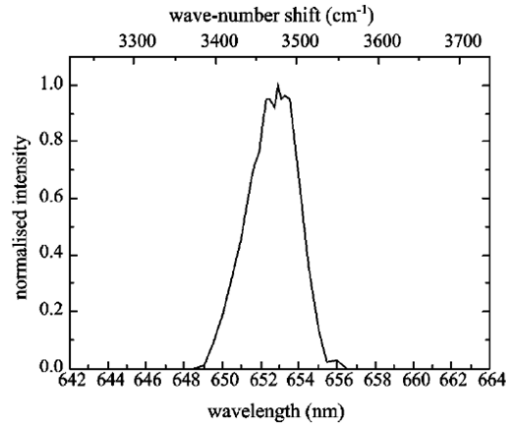


Figure 4.34. Red color shift [4]

In addition, the red light moves towards the outside of the water jet due to the interaction on the walls of the water jet. Some of the beam move in the opposite direction of the water jet. All these effects cause the laser power to gradually decrease along the water jet, as can be seen in Figure 4.35. Similarly, as the laser power is increased, the power transmission decreases as the interaction increases, as can be seen in Figure 4.36.

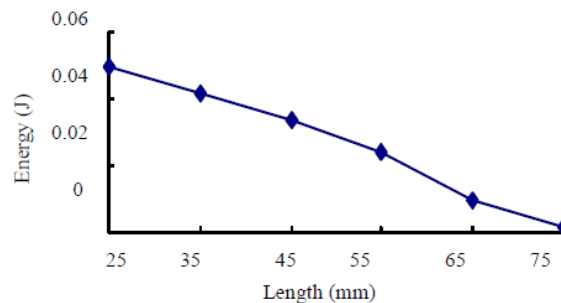


Figure 4.35. Energy vs Length [116]

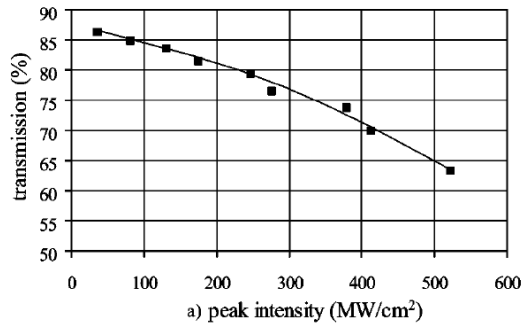


Figure 4.36. Transmission vs Peak intensity [4]

4.2.8 Laser Breakup

The frequency of the laser [order of (kHz)] is at the same level as the natural vibration frequency of the water jet. For this reason, when the water jet is combined with the high-intensity laser beam, the laser beam causes disturbance. As soon as any perturbation occurs, it continues exponentially along the surface of the water jet. When the distortion on the water surface is large enough, reflection on the inner surface becomes impossible and the light leaves the water jet almost completely. Due to the wavy interface, there can be no laser transmission along the normal stable length of the water jet. Therefore, the laser leaving the water jet is somewhere before the water breakup point, as can be seen in Figure 4.37. This point depends on the speed of the water jet, the power density, and frequency of the laser, as well as the laser-nozzle alignment setting. Due to the laser excitation of the water jet, a constant dispersion point is observed in a reproducible manner. This indicates a constant relationship between the laser beam and the laser beam-induced disturbances. In addition, laser-induced distortions dominate the water jet's own disturbance. The oscillation normally seen at the dispersion point of the water jet is no longer visible due to the laser interaction and a fixed dispersion point is obtained [105, 109].



Figure 4.37. Laser breakup [119]

The images showing the use of a water jet with a speed of 94 (m/s) coupled with a laser of 13 (W) and 20 (kHz) frequency are shared in Figures 4.38, 4.39, and 4.40. The successive disturbances became larger and larger, causing droplet formation. The locations of the disturbances are constant along the water jet. There is no excitation between laser pulses and the water jet shows normal hydrodynamic disruption [109].

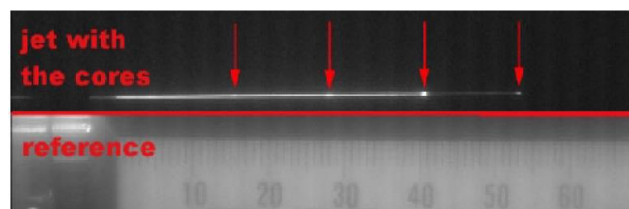


Figure 4.38. Raman scattering in the water jet [109]

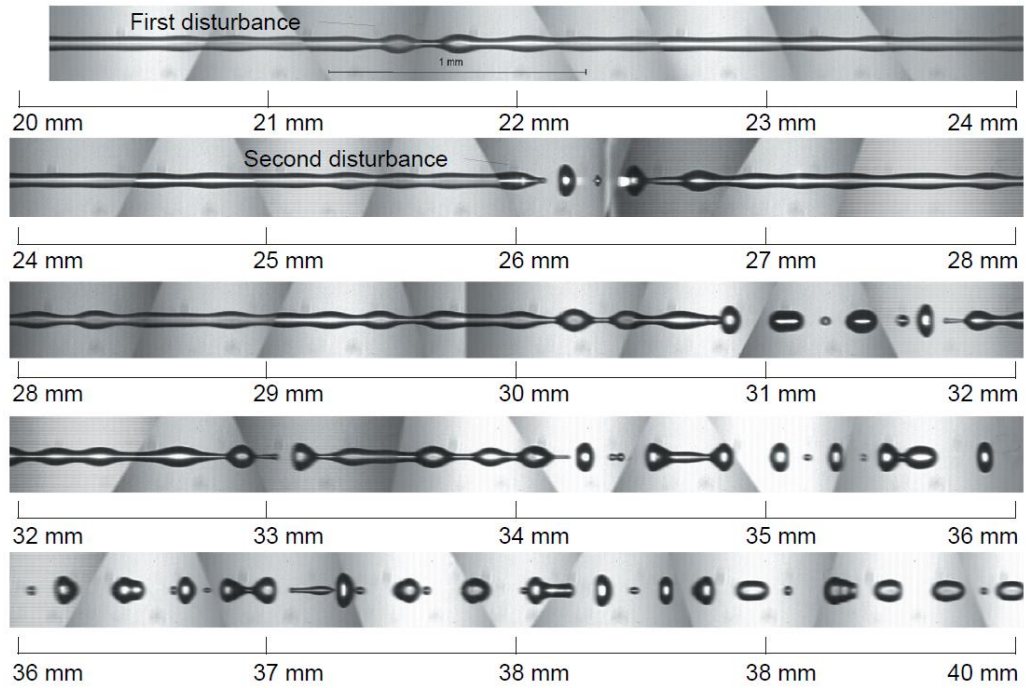


Figure 4.39. Shadowgraph images of the water jet [109]

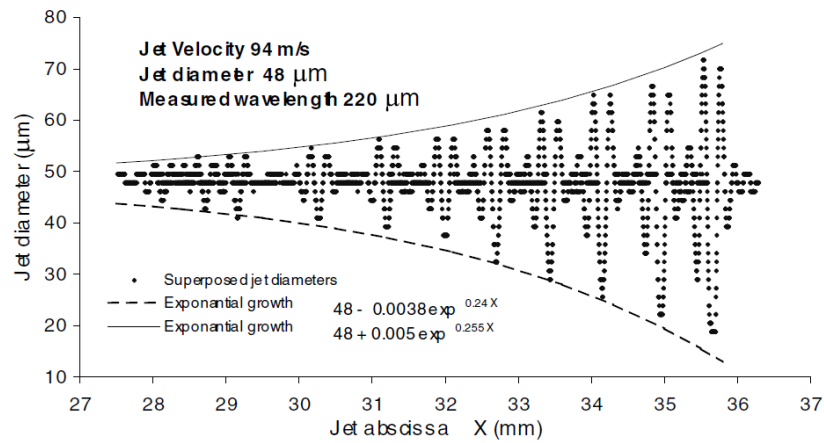


Figure 4.40. Jet diameter vs jet abscissa [109]

The reflection angle of the laser at the water jet-air interface is constantly disturbed due to surface fluctuations. Light escapes in certain areas. At the final point, the laser beam leaves the water jet at an angle of almost 90° to the water jet direction [111].

In the example shared in Figures 4.41 and 4.42, one can see that even if a droplet is formed up to the point where the laser completely leaves the water jet, some of the laser beam escapes, and some of it is directed back into the water jet towards the next droplet, and enters due to the small divergence angles. This way the process can be repeated many times, but each time some of the power is lost [111].

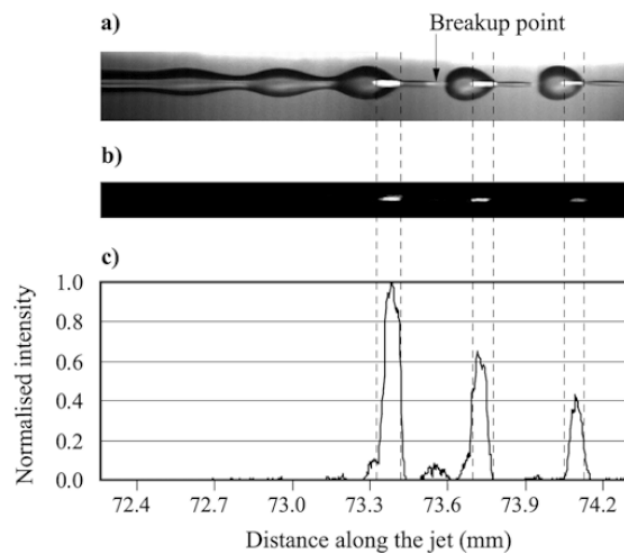


Figure 4.41. Breakup point [111]

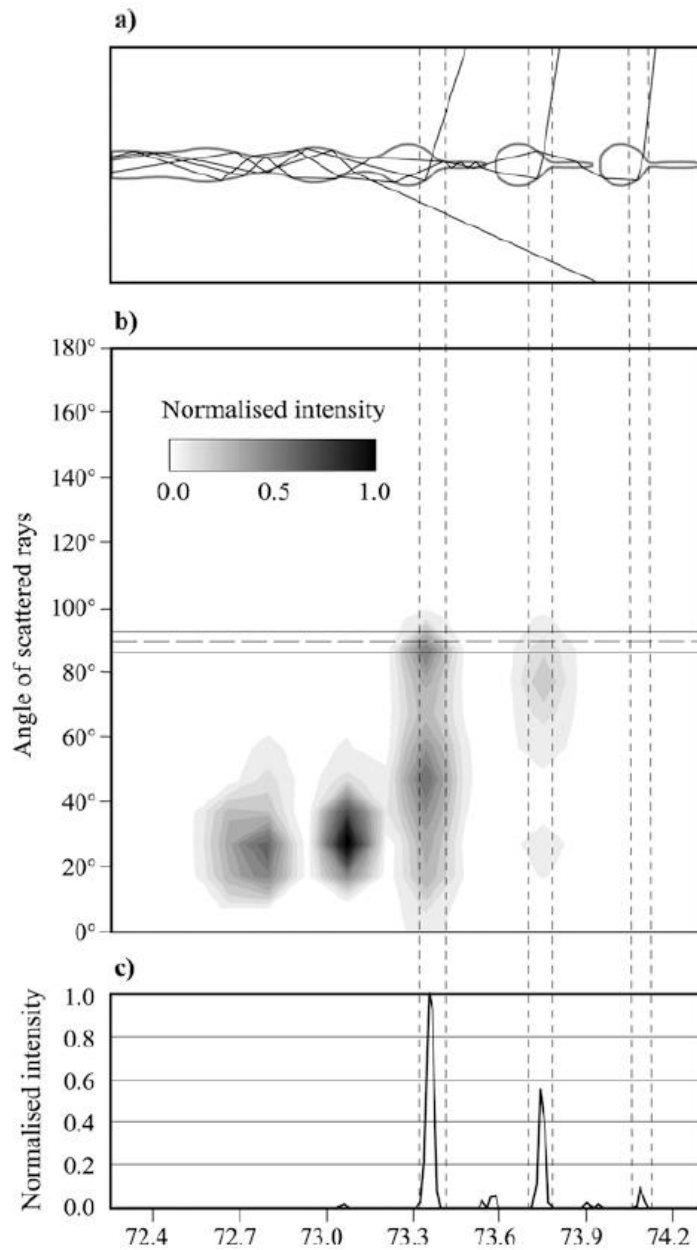


Figure 4.42. Angle of the scattered beam [111]

4.2.9 WJGL Material Interaction

Impingement of the water jet:

The water jet hitting the material surface spreads over a larger area at the contact point. A stagnation zone is formed and water begins to flow outward parallel to the

material surface. The laser beam also falls on the same spot as the pressurized water jet, as can be seen in Figure 4.43. The diameter in the stationary region is about 1.2 times the diameter of the water jet. As the laser beam exits the water jet and reaches the material surface, its cross-sectional area expands. Thus, the area of material removed becomes larger than the diameter of the water jet. Due to the previously mentioned *vena contracta* effect, the ratio of the water jet diameter to the nozzle diameter is 0.83. Since the diameter increases 1.2 times in the water stagnation zone, the area of the laser-material interaction zone is approximately equal to the nozzle diameter [66, 105].

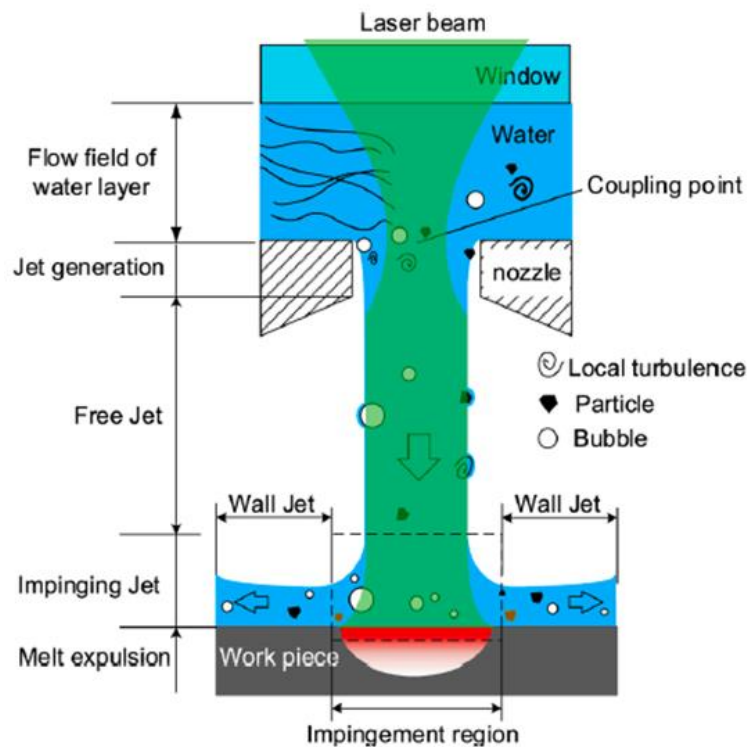


Figure 4.43. Impingement of the water jet [105]

Ablation process:

The sketch showing the stages is shown in Figure 4.44 and explained below [105]:

1. The water jet hits the material surface and begins to spread on the surface. The laser is not turned on yet.
2. The laser turns on and the laser pulse reaches the surface through the water jet. Laser energy is transferred to the material and heats the area.
3. Depending on the power density, melting, vaporization, and/or plasma formation can be seen on the material. The resulting vapor or plasma blocks the laser beam and the water jet for a short time. With the recoil pressure, a shock wave is generated and the molten material is partially removed.
4. When the laser pulse is finished, the vapor and plasma cloud disappears. The water jet removes any remaining molten material and cools the area.
5. The next laser pulse reaches the area and the same material removal cycle is repeated. The whole process is an alternate form of heating-cooling, as can be seen in Figure 4.45.

Considering the parameter ranges used, the cooling time is 1000 times the heating time.

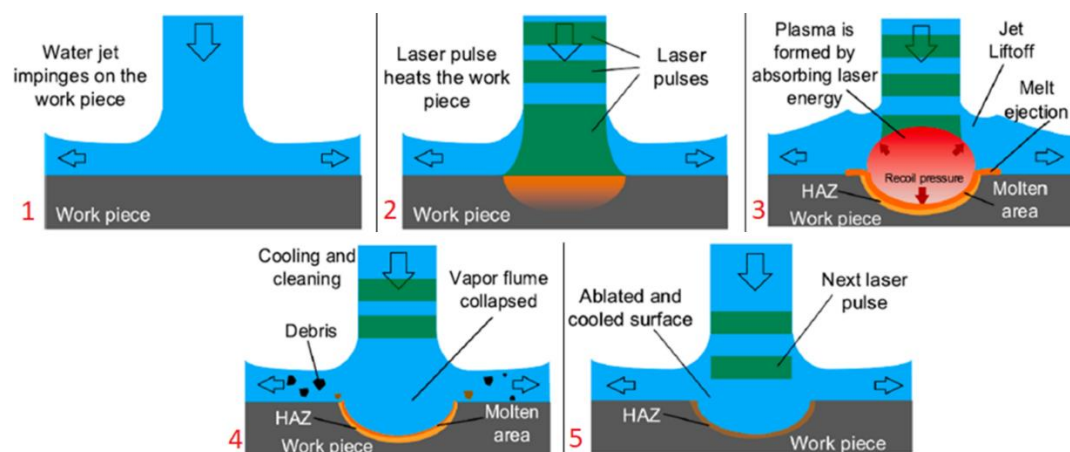


Figure 4.44. Ablation process [105]

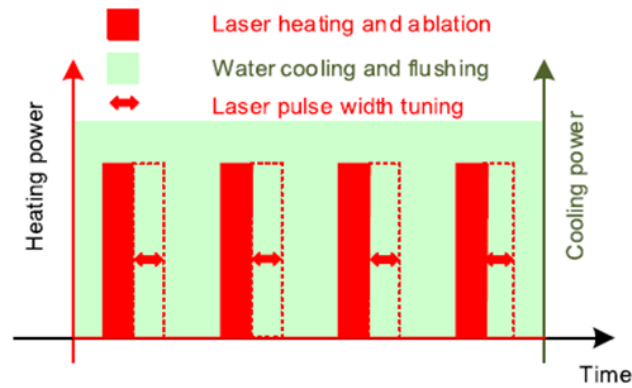


Figure 4.45. Continuous alteration of heating and cooling [105]

Photos and images showing the actual interaction are shared in Figure 4.46 (a) showing the impingement of water jet and (b) jet lift-off after the laser pulse.

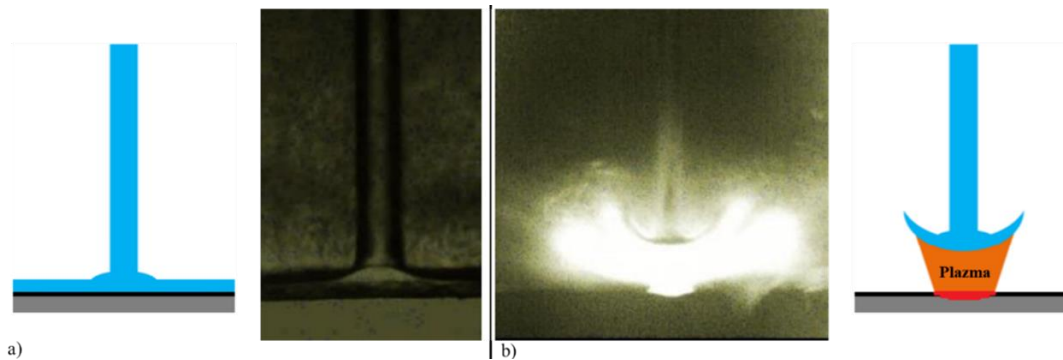


Figure 4.46. Water jet & laser interaction on the surface [68]

In the WJGL material interaction, the transition of water to the plasma state can be ignored, because for this to occur, a power density of $6 \text{ (GW/cm}^2\text{)}$ at 532 (nm) wavelength, i.e. more than the levels used by WJGL technology, is required. However, when the temperature of the material increases with the laser pulse, it is inevitable that the water in the machining zone will evaporate and form bubbles. In addition, bubbles may form in the water due to the sudden pressure drop of water jet

hitting the surface. These bubbles may scatter the laser beam trapped in the water, causing inefficiency and poor machining quality. The laser-material interaction and the energy absorption mechanism of the material during the laser pulse are the same as for LBM. However, due to the cleaning and cooling effect of the water jet between the pulses, there is no heat accumulation in the processing area and each pulse can be evaluated independently of the previous one [105].

4.2.10 WJGL Quality Review

Due to the water jet used in WJGL technology, some physical processes during material removal also change.

The kinetic energy and momentum of the water jet is much higher compared to the gas flow. The molten material on the surface is removed more effectively due to the water jet used in WJGL instead of the auxiliary gas used in LBM. Thus, the recast layer and burr formation are largely prevented [104, 108].

Due to the short laser pulses and the water jet cooling the machining area, no HAZ layer formation is observed [<1 (μm)] [101-103, 108].

Particles separated from the surface as a result of melting and vaporization are trapped in the water and do not spread into the atmosphere. Thus, the spattering problem, which is defined as the adhesion of the molten material to the surface in a large area as a result of processing, is not observed [76, 105, 108].

The processing speed and quality results to be obtained with WJGL have a close relationship with the material properties and the parameters used. Speed and quality are inversely proportional to each other. For example, working at lower power and/or slower speed affects dimensional tolerance and surface quality more positively. However, it is better and more efficient to use high power and/or fast feed in terms of machining time [71, 120].

4.2.11 WJGL Machining Efficiency

The *plasma shielding* effect, which is also seen in the LBM process due to the laser power density used, is also valid for WJGL [4, 74]. However, when compared to LBM, the WJGL process has some specific inefficiencies as follows:

1. In the WJGL process, some of the laser energy is lost in the water jet due to effects such as irregularities in the water jet and Raman scattering. This situation creates inefficiency when considering the benefit obtained in return for the energy given [4, 108].
2. The continuous cooling of the processing zone by water is good for quality, but bad for material removal rate. Therefore, the heat loss created by the water jet in the machining zone also causes inefficiency [108].
3. Water hitting the surface splashes back, largely blocking the water coming from behind, which makes it difficult for the laser beam to reach the surface. To avoid this situation, the processing area should be left behind by moving constantly, as shown in Figure 4.47 [121].

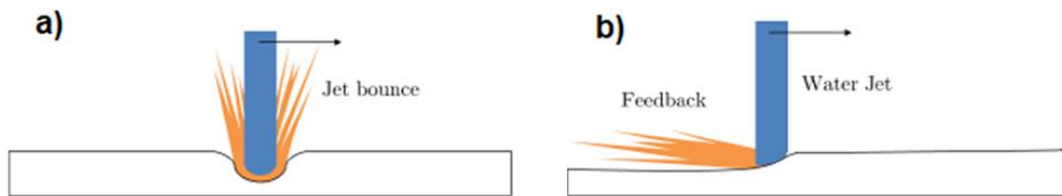


Figure 4.47. Water splashing direction [121]

4. The power density of the laser decreases, as the area of interaction in the machining zone increases due to the movement (the interaction area turns from a circle to an ellipse) [1].

5. Due to the water splashing against the direction of progress at the contact point, the water jet is distorted at the contact point and a part of the laser beam is lost by being directed outward from the cutting zone [121].
6. The water in the machining zone evaporates by absorbing energy from the heated surface [105].
7. Due to mechanical and thermal effects in the water in the machining zone, bubble formation occurs and these bubbles scatter the laser beam and reduce the energy reaching the surface [74, 108].
8. One of the reasons for inefficiency may be that the plasma-induced shock waves causing the water jet to distort [1].
9. It is easy at first to evacuate the water from the cavity formed on the surface during machining. The kinetic energy of the water jet is sufficient. In addition, as you go deeper, an air barrier is formed between the water jet and the material due to vaporization/plasma, helping the water jet to remain in a stable structure [122]. However, this only applies to a certain depth. Once the water accumulation exceeds a certain level, the water jet can no longer maintain its stable structure and the laser beam is dispersed uncontrollably in the accumulating water (Figure 4.48 a). Since the density and kinetic energy of the gas flow surrounding the water jet is also very low, its effect on removing the accumulated water is low and the water-gas boundary cannot be maintained while underwater (Figure 4.48 b). In summary, it is difficult to drill deep holes in the material with WJGL, as it becomes difficult to drain the water in the formed cavity and to maintain the stable structure of the water jet [101, 114].

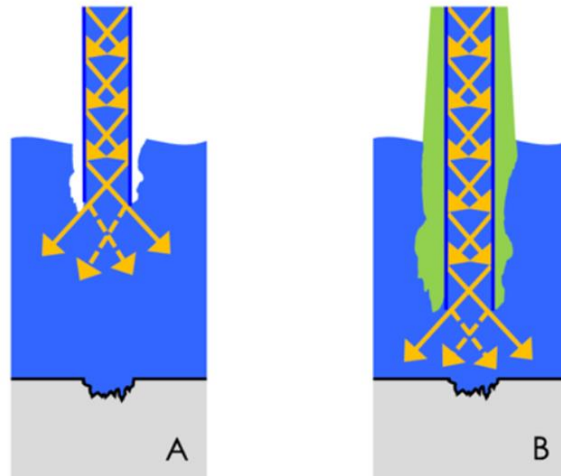


Figure 4.48. The process drowns after certain depth [114]

4.2.12 Summary

The WJGL process is a complex technology involving various physical mechanisms (laser transmission, absorption, and reflection; conduction, convection, and radiation of heat; temperature-dependent material optical and thermal properties; solid, liquid, and gas phase changes, fluids and gas dynamics). With WJGL, a direct focus on the processing area is achieved due to the water jet. The water jet is able to remove molten and vaporized material and cool the machining zone effectively.

The hydrodynamic stability of the water jet must be ensured. The relationship of water with flow parameters, nozzle, auxiliary gas, and atmospheric conditions is important. Attention should be paid to the focus parameters for the coupling of the laser with the water jet. The behavior of the laser beam in water, beam profile, and power loss must be considered.

Due to the water jet used in WJGL, there are many factors that negatively affect the material removal efficiency. A balance between processing speed and quality can be established by choosing the processing parameters properly and in accordance with the material to be processed [123].

4.3 Closure

The material removal mechanisms for both conventional laser and WJGL can be considered as the same. The water used in the WJGL process acts as a fiber to carry the laser energy to the machining zone. The material is rapidly heated due to laser energy absorption. Phase change of the material from solid to gas occurs on the surface. Material properties, such as reflectivity, thermal diffusivity, and vaporization enthalpy are important for material removal. Laser properties such as wavelength, power density, and pulse width dictate the material removal rate as well. However, there are different mechanisms involved in WJGL machining due to water jet utilization. The inefficiencies caused by water are pointed out in Section 4.2.11. The energy balance approach for WJGL is expected to provide good estimations for material removal with the use of proper efficiency factors.

CHAPTER 5

WATER JET GUIDED LASER PARAMETERS AND EXPERIMENTAL DETERMINATION OF THEIR EFFECTS ON PROCESS TIME AND QUALITY²

There are several parameters in WJGL process, as discussed in the previous chapters. For the systematic approach, firstly determining and analyzing of the process parameters are required. For this purpose, a fish-bone diagram showing the cause and effect of the WJGL process has been prepared, as can be seen in Figure 5.1. The parameters have been classified under headings of *laser*, *water jet*, *motion*, and *workpiece*, in order to reach the optimum process time and quality.

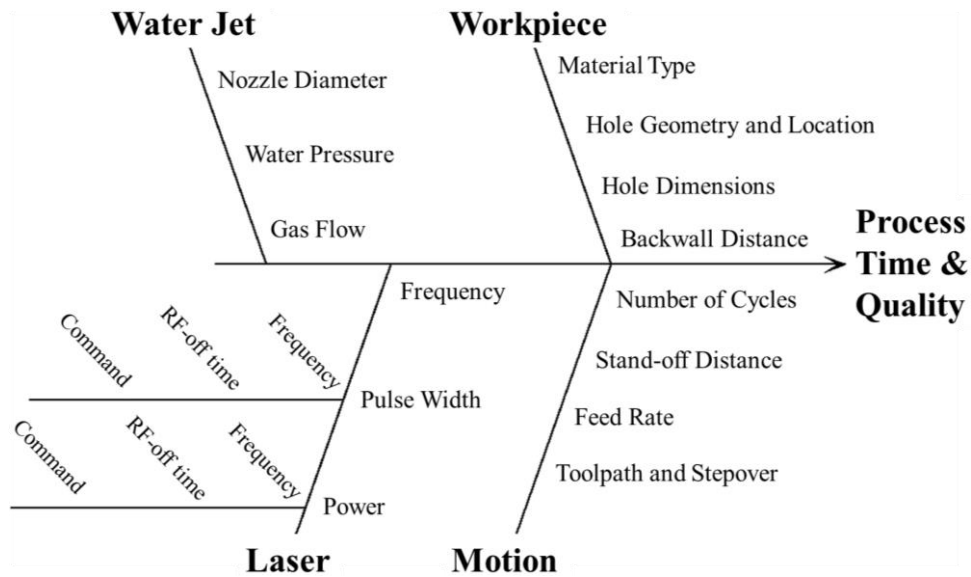


Figure 5.1. Cause and Effect Fish-Bone Diagram of WJGL Process

² This chapter is based on [134], which is a published work of the author

At the beginning, the workpiece variables are already known, such as material type, part geometry, hole diameter, etc. The nozzle diameter is almost always chosen as 50 (μm), since it is an ideal size by experience for making the required micro hole dimensions. Other process parameters have to be decided based on the previous experiences, best practices and machine constraints. In order to decide the most important parameters, an experimental study in terms of cycle time and hole quality for hole drilling has been conducted and the details are given in Section 5.1. The instruments used in experiments throughout the study are given in Section 5.2.

5.1 Experimental Studies on WJGL Process Time and Quality

As presented in previous chapters, WJGL drilling quality is better compared to conventional dry lasers, in terms of heat affected zone, recast layer, spatter, burr formation, taper, etc. However, it is difficult to model the process due to constantly flowing pressurized water splashing back from the surface. There are many variables in the process, which affects the material removal rates and quality of the cuts. In the remaining part of this chapter, a multi objective optimization in terms of process time and taper angle of the micro holes drilled on Inconel 718 super alloy is performed. This effort helps to determine the important factors, their levels, and their effects for the modeling studies.

Inconel 718 is a commonly used material in gas turbines. Solution and Precipitation Heat Treated Wrought Inconel 718 material is used in the experiments. Taguchi Design of Experiment (DOE) and statistical analysis is used to perform the experiments and evaluate the results. A spiral toolpath is used to drill 0.4 (mm) diameter holes of depth 5.6 (mm).

For the experiments, five different factors are considered, namely laser power (W), pulse width (ns), frequency (kHz), feed (mm/min), and spiral step (mm). 50 (μm) sapphire nozzle is used. Water jet pressure and gas flow are set to 200 (bar) and 1

(l/min), respectively. They are kept constant during the trials. Similarly, the standoff distance from the nozzle to the sample surface is kept constant at 10 (mm).

The factors and levels are shown in Table 5.1. Since there are five factors and two kinds of mixed levels, a modified Taguchi L-16 orthogonal table is used for the experiments [124]. The factors and levels for each trial are shown in Table 5.2.

Table 5.1 Factors and Levels

Factors	Level 1	Level 2	Level 3	Level 4
A. Laser Power (W)	25	30	35	–
B. Pulse Width (ns)	200	250	300	–
C. Frequency (kHz)	10	15	20	–
D. Feed (mm/min)	60	120	180	240
E. Spiral Step (mm)	0.010	0.015	0.020	0.025

Table 5.2 Modified Taguchi L-16 Orthogonal Table

Trial	A	B	C	D	E
1	25	200	10	60	0.010
2	25	250	15	120	0.015
3	25	300	20	180	0.020
4	25	250	15	240	0.025
5	30	200	15	180	0.025
6	30	250	10	240	0.020
7	30	300	15	60	0.015
8	30	250	20	120	0.010
9	35	200	20	240	0.015
10	35	250	15	180	0.010
11	35	300	10	120	0.025
12	35	250	15	60	0.020
13	30	200	15	120	0.020
14	30	250	20	60	0.025
15	30	300	15	240	0.010
16	30	250	10	180	0.015

In order to increase the reliability of the analysis, each trial is repeated three times. Therefore, 48 holes are drilled in total. The drilled specimen is shown in Figure 5.2.

The objective of the experiments is to decrease the process time and the taper of the holes.

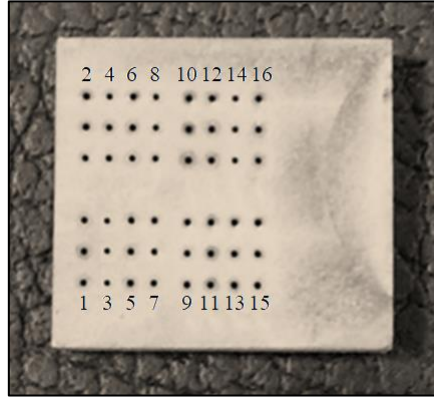


Figure 5.2. Drilled Specimen

The process time is measured with a chronometer. Diameters of the holes are measured with a steel pin gage set, which has 0.01 (mm) increments. Following that, the taper angle (T_a) can be calculated as follows

$$T_a = \tan^{-1} \left(\frac{D_t - D_b}{2d} \right) \quad (5.1)$$

where, D_t is the diameter at the entrance (top), D_b is the diameter at the exit (bottom), and d is the hole depth (workpiece thickness), which is 5.6 (mm).

Analysis is performed using Signal-to-Noise Ratio (SNR) proposed by Taguchi [124]. SNR is a variance index dependent on Mean Square Deviation (MSD). The advantage of using SNR value is that it both contains the mean value and the variance of the data considered. The equation of SNR is

$$SNR = -10 \log_{10}(MSD) \quad (5.2)$$

The value of MSD in this equation depends on the quality characteristic, whether it is *smaller is better*, *nominal is better*, or *larger is better*. Considering process time

and taper angle, they both fit with the *smaller is better* case, for which the equation is given as

$$MSD = \sum_{i=1}^n y_i^2 / n \quad (5.3)$$

where, y_i 's are the obtained results for each repeated test and n is the number of repetitions, which is always 3 in this study. The mean and *SNR* values of the process time and taper angle of the holes obtained after the trials are given in Table 5.3. The response plots with the mean values are given in Figures 5.3 and 5.4.

Table 5.3 Results of the Experiments

Trial	Process Time		Taper Angle	
	Mean (s)	SNR	Mean (°)	SNR
1	361	−51.162	0.46	6.702
2	914	−59.217	0.49	6.106
3	2917	−69.300	0.53	5.569
4	1249	−61.936	0.53	5.528
5	668	−56.497	0.60	4.476
6	305	−49.773	0.46	6.702
7	880	−58.896	0.65	3.763
8	2390	−67.576	0.56	4.970
9	776	−57.814	0.55	5.203
10	312	−49.940	0.43	7.310
11	163	−44.262	0.34	9.322
12	285	−49.101	0.43	7.392
13	539	−54.640	0.38	8.498
14	2008	−66.058	0.41	7.760
15	821	−58.339	0.55	5.253
16	192	−45.666	0.36	8.861
Average	924	−56.261	0.48	6.463

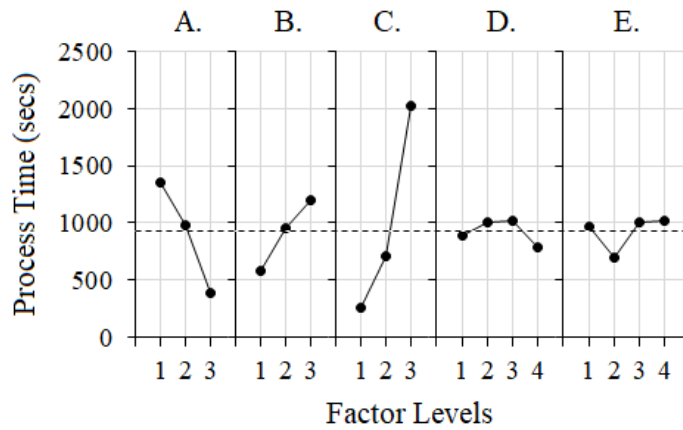


Figure 5.3. Response Plots for Process Time

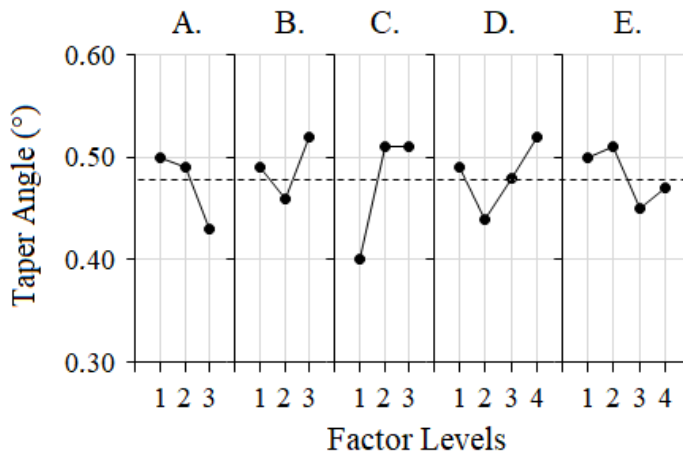


Figure 5.4. Response Plots for Taper Angle

Tables of the main effects for process time and taper angle are provided in Table 5.4 and Table 5.5. When considering *SNR* values, larger value always indicates a better result. Thus, considering the values in the tables, laser power should be chosen as 35 (W) and frequency as 10 (kHz) for the optimal condition. However, there are conflicts with the optimum pulse width, feed, and spiral step values.

Table 5.4 Main (Average) Effects of Factors for Process Time in Terms of *SNR*

Factors	Level 1	Average Effects		
		Level 2	Level 3	Level 4
A. Laser Power (W)	−60.404	−57.181	−50.279	−
B. Pulse Width (ns)	−55.028	−56.159	−57.699	−
C. Frequency (kHz)	−47.716	−56.071	−65.187	−
D. Feed (mm/min)	−56.304	−56.424	−55.351	−56.966
E. Spiral Step (mm)	−56.754	−55.398	−55.703	−57.188

Table 5.5 Main (Average) Effects of Factors for Taper Angle in Terms of *SNR*

Factors	Level 1	Average Effects		
		Level 2	Level 3	Level 4
A. Laser Power (W)	5.976	6.286	7.307	−
B. Pulse Width (ns)	6.220	6.829	5.977	−
C. Frequency (kHz)	7.897	6.041	5.876	−
D. Feed (mm/min)	6.404	7.224	6.554	5.671
E. Spiral Step (mm)	6.059	5.983	7.040	6.772

It is not always possible to find the same optimum factor levels for every characteristic at the same time. In these circumstances, the relative weight of each characteristic can be combined into one Overall Evaluation Criterion (*OEC*) index. It is then possible to perform optimization based on these new values [124]. In order to calculate the *OEC*, which is a dimensionless index between 0 and 1, one needs to determine the weight of each characteristic, the best and worst readings of the experiments. Following that, the *OEC* can be defined as

$$OEC = \sum_{i=1}^n \frac{y_{imax} - y_i}{y_{imax} - y_{imin}} w_i \quad (5.4)$$

where, y_i is the measured reading, y_{imax} and y_{imin} is the worst and best readings of each characteristic for *smaller is better* case, and w_i is the weight of each characteristic. The weights are determined based on the importance of the characteristics for the practitioner. Assuming taper angle (quality) is more important than process time, the related values for calculating *OEC* are given in Table 5.6.

Table 5.6 Overall Evaluation Criterion (*OEC*) Description

Criteria Description	Best Reading	Worst Reading	Relative Weight
1. Process Time (s)	161	2975	40%
2. Taper Angle (°)	0.31	0.67	60%

The mean and *SNR* values of the combined *OEC* index of process time and taper angle are given in Table 5.7. The main effects table of *OEC* is given in Table 5.8. The *MSD* value in order to find the *SNR* is calculated according to *larger is better* case, for which the equation is given as

$$MSD = \frac{1}{n} \sum_{i=1}^n \frac{1}{y_i^2} \quad (5.5)$$

Table 5.7 *OEC* Scores

Trial	Values of each repetition			Mean	<i>MSD</i>	<i>SNR</i>
	<i>OEC</i>#1	<i>OEC</i>#2	<i>OEC</i>#3			
1	0.80	0.63	0.71	0.71	2.013	−3.038
2	0.64	0.55	0.55	0.58	3.032	−4.817
3	0.23	0.26	0.23	0.24	17.598	−12.455
4	0.51	0.49	0.42	0.47	4.552	−6.582
5	0.41	0.42	0.50	0.44	5.230	−7.185
6	0.63	0.81	0.73	0.72	1.978	−2.961
7	0.29	0.30	0.39	0.33	9.869	−9.943
8	0.26	0.18	0.32	0.25	18.170	−12.594
9	0.39	0.66	0.49	0.51	4.341	−6.376
10	0.80	0.90	0.64	0.78	1.754	−2.440
11	0.91	1.00	0.91	0.94	1.132	−0.537
12	0.81	0.81	0.73	0.78	1.647	−2.166
13	0.77	0.86	0.86	0.83	1.457	−1.634
14	0.56	0.58	0.56	0.57	3.123	−4.946
15	0.55	0.48	0.49	0.51	3.939	−5.954
16	1.00	0.91	0.82	0.91	1.230	−0.898

Table 5.8 Main (Average) Effects of Factors for *OEC* in Terms of *SNR*

Factors	Average Effects			
	Level 1	Level 2	Level 3	Level 4
A. Laser Power (W)	−6.723	−5.764	−2.880	–
B. Pulse Width (ns)	−4.558	−4.675	−7.222	–
C. Frequency (kHz)	−1.858	−5.090	−9.092	–
D. Feed (mm/min)	−5.023	−4.895	−5.744	−5.468
E. Spiral Step (mm)	−6.006	−5.508	−4.804	−4.813

When considering *OEC* values, larger value always indicates a better result. Thus, looking at the table, laser power should be chosen as 35 W, pulse width as 200 ns, frequency as 10 kHz, feed as 120 mm/min, and spiral step as 0.020 mm for the optimal condition ($A_3B_1C_1D_2E_3$). These factor levels should allow a less tapered hole to be processed with minimal process time.

Analysis of Variance (*ANOVA*) analysis is also performed to see the significance levels of all the factors. The *ANOVA* table for *OEC* mean values can be seen in Table 5.9. Looking at the percentage values in the table, frequency is the most dominant factor affecting the results. Feed and spiral step are less important, even statistically insignificant factors, so it is up to the practitioner to choose their levels arbitrarily.

Table 5.9 *ANOVA* Analysis

Factors	DOF (f)	S	V	F	S'	P (%)
A. Laser Power (W)	2	0.141	0.070	16.372	0.132	17.8
B. Pulse Width (ns)	2	0.048	0.024	5.637	0.040	5.4
C. Frequency (kHz)	2	0.369	0.185	42.996	0.361	48.6
D. Feed (mm/min)	3	0.015	0.005	1.134	0.002	0.2
E. Spiral Step (mm)	3	0.020	0.007	1.519	0.007	0.9
Other/Error	35	0.150	0.004	–	–	27.2
Total	47	0.743	–	–	–	100.0

It is also possible to calculate the expected outputs based on the selected factor levels at this point. Contribution of each factor level on the average value is taken into consideration one by one for each characteristic, as shown in Table 5.10.

Table 5.10 Estimation of Performance for the Optimal Condition

Factors	Process Time			Taper Angle		
	Average	SNR Opt	Contribution	Average	SNR Opt	Contribution
A.	-56.261	-50.279	5.981	6.463	7.307	0.847
B.	-56.261	-55.028	1.232	6.463	6.220	-0.240
C.	-56.261	-47.716	8.545	6.463	7.897	1.437
D.	-56.261	-56.424	-0.163	6.463	7.224	0.764
E.	-56.261	-55.703	0.558	6.463	7.040	0.580
Total			16.155			3.388
Est.		-40.106			9.848	

The estimated *SNR* value is calculated by adding the total contribution to the average performance, which is -56.261 for process time and 6.463 for taper angle. Based on the estimated *SNR* values, the expected values for process time and taper angle can be found by the equation provided below.

$$MSD = \sigma^2 + (y_a - y_0)^2 \quad (5.6)$$

Where, σ is the standard deviation, y_a is the sample average and y_0 is the target value. Considering the average value only and *smaller is better* case, $\sigma=0$ and $y_0=0$. Following that, using Equation (5.2) and simplifying, Equation (5.6) becomes

$$y_a = \sqrt{10^{-\frac{SNR}{10}}} \quad (5.7)$$

Therefore, using Equation (5.7) and the estimated *SNR* values in Table 5.10, the process time is calculated as 101 (s) and taper angle as 0.32° at the optimum condition.

In order to verify the estimated performance, verification tests with 5 repeats are performed. Using the optimal condition ($A_3B_1C_1D_2E_3$), the mean values of the obtained results are close to the expected values, as shown in Table 5.11.

Table 5.11 Confirming Predicted Results

Criteria Description	Expected Reading	Verification Result
1. Process Time (s)	101	120
2. Taper Angle ($^{\circ}$)	0.32	0.24

The reason for errors or deviations between the expected and the verified results are related to the confidence interval of the estimated performance. Since there are other factors affecting the process, such as real-life disturbances, variations and/or interactions between factors, deviations are always expected. This result also shows that the process window should be extended to cover other parameters and values for further experiments. In this case, the results seem close. Average taper angle performance of 0.24° is even better than expected, which is a value that could not be obtained in the initial trials.

Calculating the peak intensity (or power density) given in Equation (2.4), and matching against the process time measured in the experiments, the plot shown in Figure 5.5 can be obtained. It is clear that there is a strong dependence between the two variables. Thus, it is justified that the optimum condition of 35 (W), 200 (ns), and 10 (kHz) provides better processing time since their calculated peak intensity of 0.97 is higher compared to the values used at initial trials. It seems possible to increase the peak intensity even more, in order to decrease the process time. Laser power should be increased and/or frequency and pulse width should be decreased for this purpose. However, the power density is a constraint for the machine. The damage threshold of the water jet nozzle is approximately 1 (GW/cm^2). This limit should not be exceeded and the optimum condition is already very close to the limit.

Thus, there is not much room for further improvement, when peak intensity is considered.

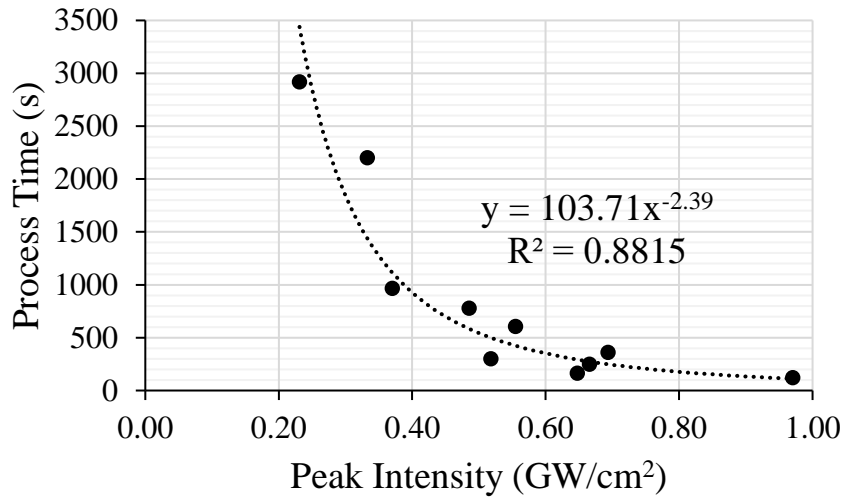


Figure 5.5. Peak Intensity vs. Process Time

Taguchi approach is proved to be useful, as also verified by further tests. Both process time and taper angle objectives are optimized by adjusting the levels. Faster process time is obtained by using the laser parameters that yields to higher peak intensity. Thus, for better performance laser power should be increased or pulse width and frequency should be decreased, taking into account the damage threshold of the nozzle.

The design of experiment did not include any possible interactions or noise factors. Looking at the *ANOVA* table, the error term percentage of 27.2% suggests that there might be some other effects, such as power and pulse width fluctuations, or water splash back blocking the laser beam. It is possible to perform further experiments to understand the factor interactions and fine-tune the results even more. Expanding the process window to include different factor levels and experimenting with different factors, such as water and gas pressure, etc. are done and presented in Chapter 6.

5.2 Instruments used in Experimental Studies

Different types of devices are used for data collection and experiments throughout the thesis. Table 5.12 shows these instruments together with measuring and usage purposes.

Table 5.12 Types of Measurement Instruments and Their Use

Instrument	For Measuring	Used in
Chronometer	The process time	Experiments on process time and quality
Steel pin gage set	Diameter of the holes	Experiments on process time and quality
Power meter	Laser power	Modeling experiments
Oscilloscope	Pulse width	Modeling experiments
Scale	Weight of the samples	Modeling experiments
Image sensor	Laser length and power	Laser beam characteristic measurements
Acoustic sensor	Laser power, hole depth, machining efficiency, and breakthrough	Laser beam characteristic measurements and studies regarding machining behavior depending on hole geometry
X-ray Computed Tomography (CT) device	Hole depth and morphology	Studies regarding machining behavior depending on hole geometry

CHAPTER 6

GENERAL STRUCTURE OF PROCESS MODELING OF WATER JET GUIDED LASER³

There are many parameters in WJGL process, which affect the material removal rate and the quality of the cuts, as presented in Chapter 5. However, correlation of these parameters to process time and quality are not delivered yet. The physics of the material removal is very complex, as mentioned in Chapter 4. A holistic process model including the effect of machine parameters, material properties and hole geometry for the WJGL micro hole drilling process is needed.

In this chapter, the process is elaborated and a useful material removal model is introduced for drilling nickel-based aerospace alloys. Different methodologies including machine learning, empirical (statistical) modeling, and mathematical modeling are used, together with data collection and experiments. The result is a simplified model for a complex process. The proposed model would predict the process time and quality, and decrease the trial and error steps while deciding on the inputs for the optimized results.

In the following sections, the modeling approach and material removal theory are presented. Following that, experiments are conducted and the results are discussed. Finally, the procedure for material removal prediction using the developed model is described.

³ This chapter is based on [135], which is a published work of the author

6.1 General Structure of Process Modeling of Water Jet Guided Laser

In order to perform modeling and process optimization of WJGL micro hole drilling on nickel-based aerospace alloys, the process parameters should be considered separately and sequentially. Thus, the input process parameters given in Figure 5.1 are organized in a flowchart. General flowchart of the WJGL process modeling is given in Figure 6.1.

In order to obtain a material removal model for the WJGL process, some intermediate steps should be considered. Each step should be considered independently, before moving on to the next step. The first step is finding the relation between machine inputs and the in-process laser parameters (laser power and pulse width). This is important, since the obtained values shall be used later in laser ablation equations. As the second step, the effective cutting length should be predicted in order to see the drilling depth capability and also to choose an appropriate standoff distance to prevent back-wall damage. As the third step, the laser power variation within the water jet should be known so that the power level at the end of the effective cutting length can be checked to see if it is sufficient to ablate material from the workpiece for efficient machining. Finally, as the fourth step, a mathematical model can predict the material removal, taking into account all the manual inputs and the predicted in-process variables.

For modeling of these steps, *black-box* and *white-box* modeling methodologies are mixed. Data collection, statistical analysis, physical knowledge, and theoretical analysis are used together, forming a *grey-box* modeling methodology, as can be seen in Figure 6.2.

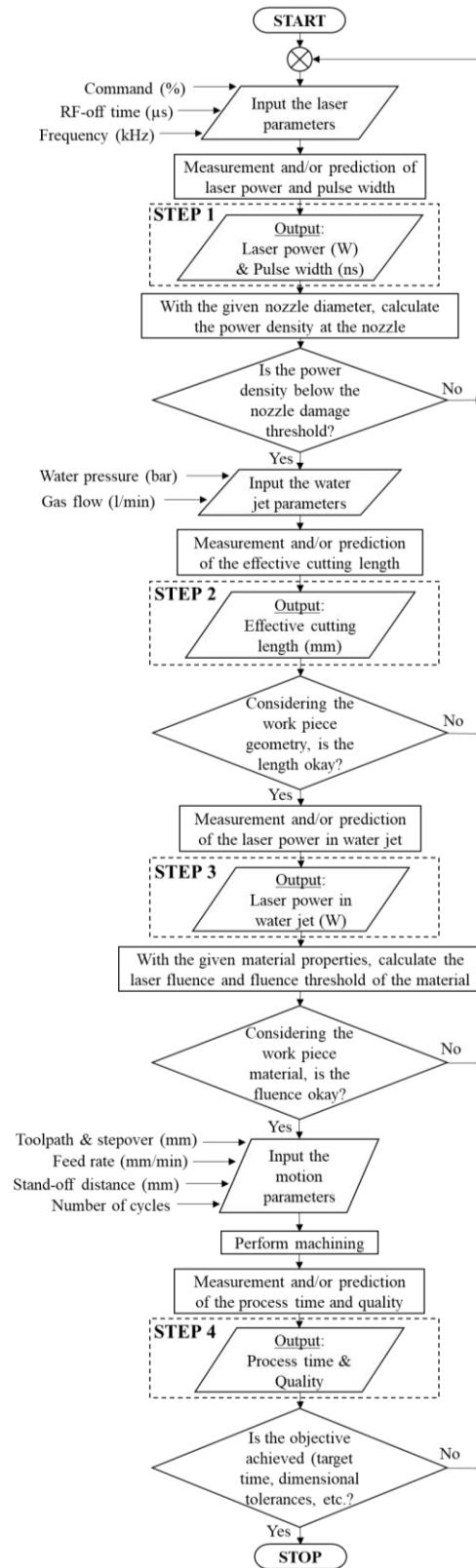


Figure 6.1. General flowchart of WJGL process modeling

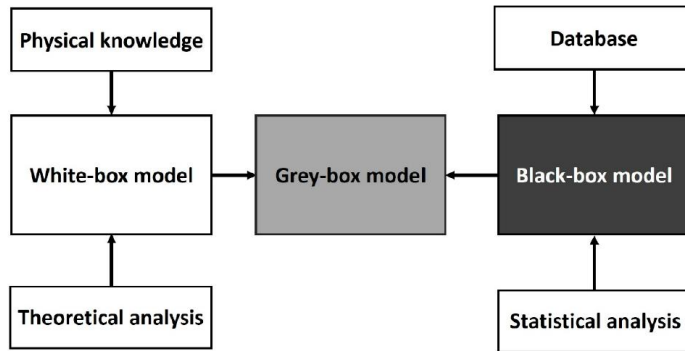


Figure 6.2. General process modeling methodologies

6.2 Modeling for Prediction of the Laser Power, the Pulse Width, the Effective Cutting Length, and the Laser Power in the Water Jet

It is difficult to predict the laser power, the pulse width, the effective cutting length and the laser power in the water jet due to some unmeasurable or uncontrollable factors. The laser parameters are highly affected by the construction of the laser unit, such as variation in properties of the optical components, and distance between the components. There are fluctuations or variations in ambient temperature, humidity, pressure, electrical current, water resistivity, water temperature, nozzle edge sharpness, nozzle roundness, machine vibrations, pump pressure, gas flow due to turbulences, and degradation of optical components, which affect the results as well. It is not easy to express the effects of these factors in a physical model. A better and simplified approach would be to collect the necessary data in time and find the relations empirically, in order to use the results in the final material removal model. The accuracy of this statistical model is shown to be sufficient for the purpose of this study. The aim of this section is to compare different modeling approaches and determine the best one for the first three steps shown in Figure 6.1.

6.2.1 Data Collection for Prediction of the Laser Power, the Pulse Width, the Effective Cutting Length, and the Laser Power in the Water Jet

The number of experimental conditions for data collection for the purpose of laser parameters modeling is 2440. The manual inputs and their chosen levels are shown in Table 6.1. The upper and lower limits of the parameters are based on the machine constraints and a process window suitable for drilling of superalloys. The measurements are done by using the internal powermeter and oscilloscope in the machine. Results vary between 0.1 – 37.2 (W) for power and 65 – 549 (ns) for pulse width.

Table 6.1 Input Levels for Measuring the Laser Parameters (Power & Pulse Width)

Manual Inputs	Levels
A. Command (%)	60, 65, 70, 75, 80 --- (5 levels)
B. RF – off time (μ s)	1.00 to 4.00 with 0.05 increments --- (61 levels)
C. Frequency (kHz)	6, 8, 10, 12, 14, 16, 18, 20 --- (8 levels)

Similarly, the amount of data obtained for modeling the effective cutting length is 720. The related manual inputs and their levels are shown in Table 6.2. The measurements are done manually. Results vary between 22 – 64 (mm) for the effective cutting length.

Table 6.2 Input Levels for Measuring the Effective Cutting Length

Manual Inputs	Levels
A. Command (%)	60, 70, 80 --- (3 levels)
B. RF – off time (μ s)	1.20 to 3.00 with 0.20 increments --- (10 levels)
C. Frequency (kHz)	8, 10, 12, 14 --- (4 levels)
D. Water Pressure (bar)	200, 300, 400 --- (3 levels)
E. Gas flow (l/min)	1, 2 --- (2 levels)

In order to collect data to see the decrease of laser power in the water jet, an external waterproof powermeter is used to take measurements at different heights. Different parameter sets from Table 3 are selected, and the power is measured with 5 (mm) increments starting from the nozzle tip. Three measurements are taken for each condition, in order to increase the reliability of the analysis.

6.2.2 Artificial Neural Network Method for Prediction of the Laser Power, the Pulse Width, and the Effective Cutting Length

Machine learning methods are receiving increasing interest from the world class manufacturers and it is one of the key topics of Industry 4.0 [125]. Especially, artificial neural network (ANN) method has been used in many cases for different laser applications and produced successful results [126-128].

ANN model is a type of a mathematical function. In order to use the model, the related dataset is introduced for training. During the training, the coefficients of the model are determined based on the input and output relations. After the network is trained, the physical representation of the system is embedded into the model and it is ready to produce meaningful results based on the inputs. A well-described ANN model can approximately compute any continuous function [129]. There are different types of ANNs, but in this study a feed forward network, also known as multi-layer perceptron (MLP), is applied, since it is a common and sufficient type for the data that is going to be used. An example of a regression model making use of an MLP model can be seen in Figure 6.3.

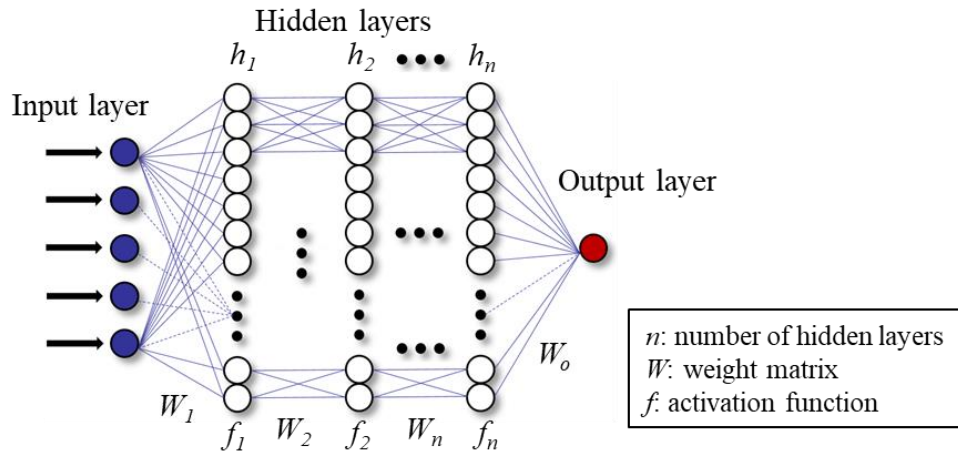


Figure 6.3. An Example of a Feed Forward Network

Using ANN modeling brings its own challenges. There are many parameters related to the quality of the network, which are called hyper-parameters. Unfortunately, there is not a readily available method to obtain the best hyper-parameters for a given dataset. They are generally decided based on experience, trial and error, or systematic search. Extensive research is still going on in this area [130]. Some of the important hyper-parameters for the ANN model are; number of hidden layers, number of neurons for the layers, activation function, cost function, optimizer type, learning rate, etc.

In order to increase the reliability of the model, it is important to avoid overfitting issue during training, which is a phenomenon of memorizing the data points rather than generalization of the dataset. An example can be seen in Figure 6.4. An early stop routine is used in order to avoid the overfitting problem. Thus, if the error of the validation data is not going down for a certain number of epochs, the training is stopped, as can be seen in Figure 6.5.

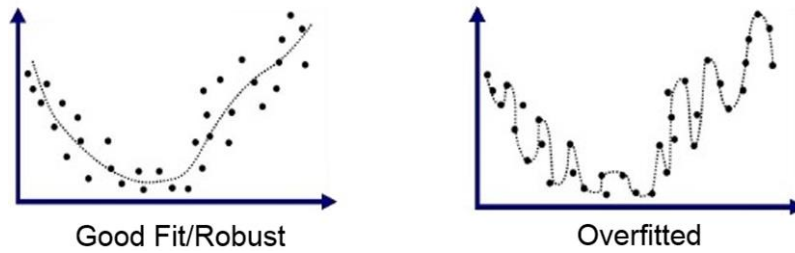


Figure 6.4. Examples of Good Fit and Overfitted Models on the Same Data

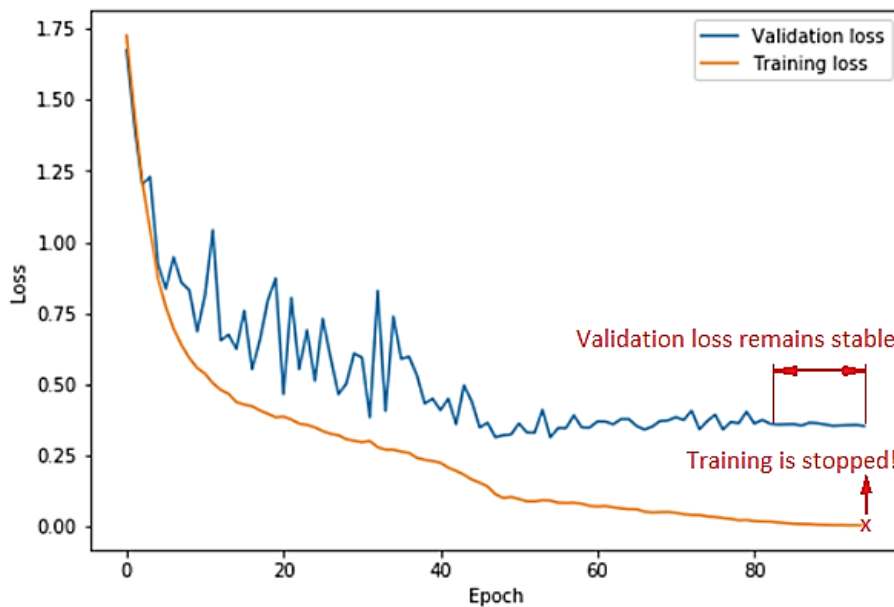


Figure 6.5. How the Early Stop Command Works

The ANN is coded, trained, and tested in Python 3.6 using Tensorflow and Keras libraries. The collected data is randomly split into two parts as 80% training and 20% test data. The training data is further split into 80%-20% as training and validation data. Many trials are performed to determine the best hyper-parameters for power, pulse width, and effective cutting length predictions. Brute force technique is used for the purpose, which allows exhaustively searching for the best set of hyper-parameters of all possible combinations. Since the designed network is not very wide

and deep, the training time is short, mostly within minutes. It takes generally less than 200 epochs for the training to stop, which means the global minimum of the loss function is reached quite fast. Each of the prospective models are run 30 times to test how well the model is generalizing the dataset. The best results for all the datasets are obtained for the hyper-parameters shown in Table 6.3.

Table 6.3 Selected Hyper-parameters for the ANN Models

Number of hidden layers	3
Number of neurons per layer	512
Activation function of the neurons	tanh
Cost function	Mean squared error
Optimizer	RMSprop
Learning Rate	0.001
Weight initialization	Xavier uniform
Normalization	Yes (using standard deviation)

Test results with the constructed ANN model show that power, pulse width and effective cutting length can be predicted with average ± 0.3 (W), ± 4 (ns), and ± 1.7 (mm) error margins, respectively. These are the mean absolute error values of the test data. Since this is a black box model, it is not possible to see the important factors or the relations between inputs and outputs. However, estimation of the model is very good. As a result, ANN model is useful considering that closer predicted values for the measured in-process variables are needed for a better material removal model in the end.

6.2.3 Statistical Analyses for Prediction of the Laser Power, the Pulse Width, the Effective Cutting Length, and the Laser Power in the Water Jet

The collected data can also be evaluated for statistical analysis and regression. Residual plots are checked so that the validity of the analyses is confirmed. The mean

effects plots created in Minitab 18 software for power, pulse width, and effective cutting length can be seen in Figures 6.6 – 6.8, respectively.

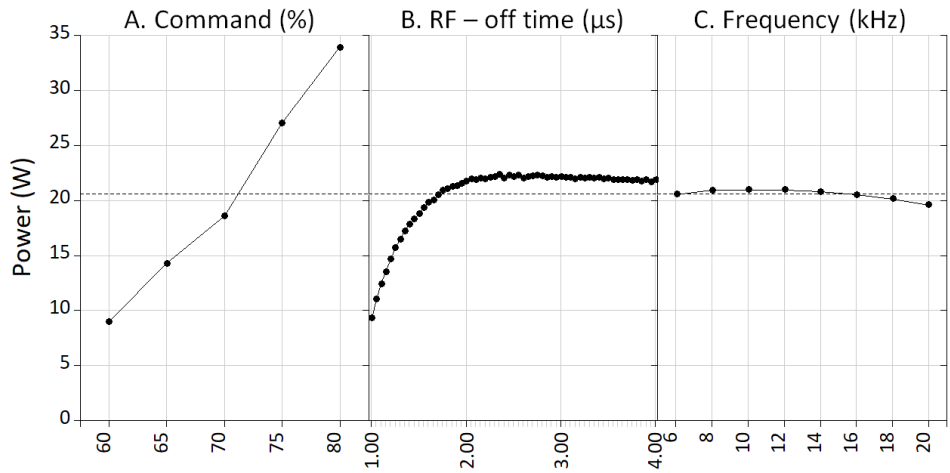


Figure 6.6. Response Plot for Power

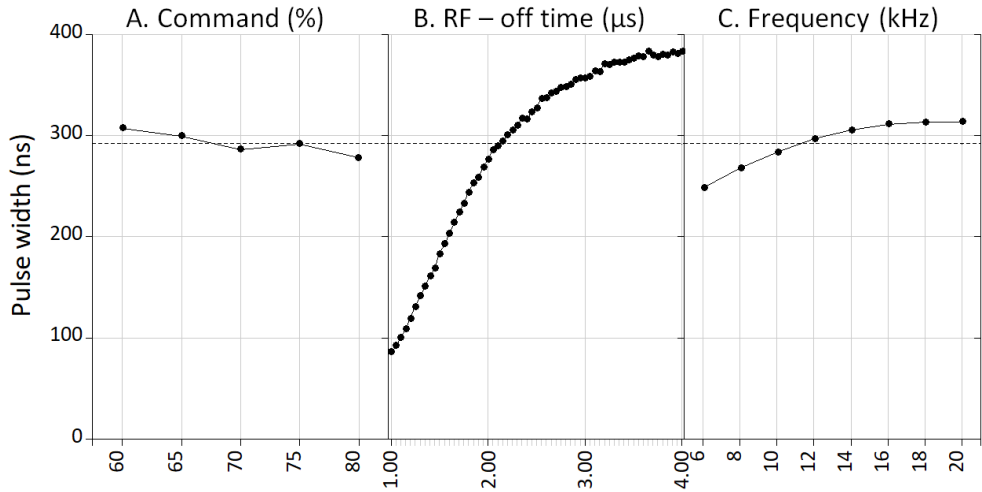


Figure 6.7. Response Plot for Pulse Width

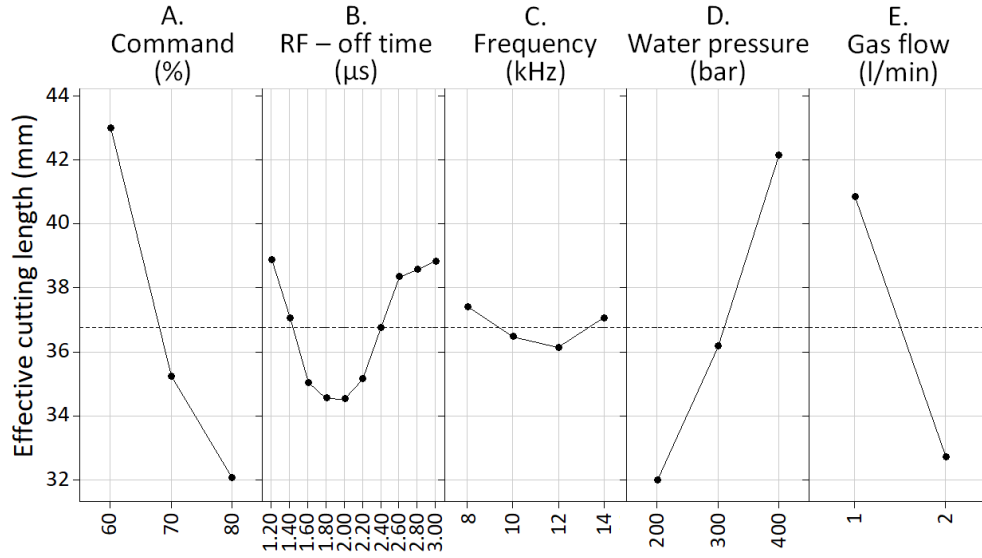


Figure 6.8. Response Plot for Effective Cutting Length

It can be seen that command value is linearly proportional and the dominating factor for predicting power, whereas RF – off time is the most contributing factor for pulse width prediction. On the other hand, effective cutting length is mostly affected by command, water pressure, and gas flow parameters. The interactions between the variables may also be important. Hence, the regression equations are constructed accordingly. In their most basic form, the linear regression models for power (P), pulse width (τ_p), and effective cutting length (ℓ) are given as follows:

$$P = -76.54 + 1.3684A + 7.19B - 0.382C - 0.0899AB + 0.00055AC - 0.106BC + 0.00307ABC \quad (6.1)$$

$$\tau_p = 3.440A + 209.17B - 40.25C - 3.034AB + 0.3652AC + 11.952BC - 0.0606ABC \quad (6.2)$$

$$\ell = 0.0043A + 4.363B + 1.087C + 0.07434D - 4.985E \quad (6.3)$$

where A is the command (%), B is the RF – off time (μ s), C is the frequency (kHz), D is the water pressure (bar), and E is the gas flow (l/min). The coefficient of determination (R^2) for the aforementioned equations are 92.31%, 98.04%, and 95.50%, respectively. Regression equations seem to provide a good approximation

for predicting the measured in-process variables. However, using the collected dataset, the average error margins can be calculated as ± 2.0 (W), ± 37 (ns), and ± 6.5 (mm) for power, pulse width, and effective cutting length, respectively, which are worse than the results of the ANN models. It can be concluded that regression provides valuable insight about the dataset, but lacks the accuracy needed for the material removal model.

The power variation inside the water jet can be evaluated by using curve fitting method. The measurements of different conditions of Table 6.2 approximately yield a plot shown in Figure 6.9. Individual data points are not shown here, in order not to complicate the plot.

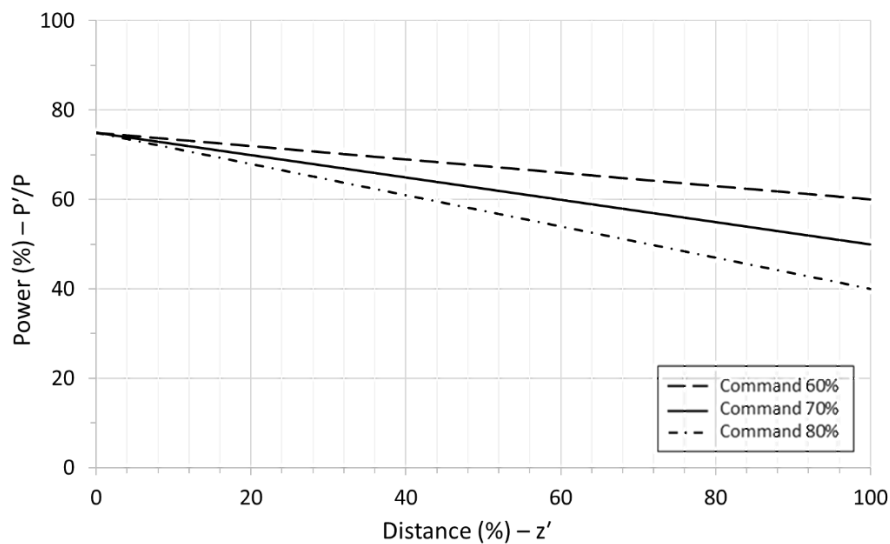


Figure 6.9. Power Variation Plot

The plot starts at 75% of the laser power at nozzle tip. For each condition, there is almost a linear decay towards the end of the effective cutting length. Looking at the results, command value is the main factor changing the slope for power decrease. This is expected, since an increase in laser energy increases the laser-water

interactions. Thus, a corrected power value in the water jet depending on the distance from the tip can be expressed as follows:

$$P' = P(-Mz' + 0.75) \quad (6.4)$$

where P' is the corrected power, z' is the normalized distance from the nozzle tip by using the effective cutting length, P is the laser power, and M is the slope coefficient depending on the command input value. The value of M can be taken as 0.15, 0.25, and 0.35 for command values of 60%, 70%, and 80%, respectively. Taking into consideration all the tried conditions, the R^2 for Equation (6.4) is on average 89.42%, which is a good approximation. It is also possible to perform a linear interpolation to calculate the value of M for different command values.

It can be seen from Figures 6.8 and 6.9 that the effective cutting length and laser power in the water jet are inversely proportional. Depending on the workpiece material and geometry, in order to obtain a proper length with adequate power, necessary adjustments should be done for machining efficiently.

The predicted values for the laser power, pulse width, effective cutting length, and corrected power within the jet using the aforementioned models are all inputs for the mathematical model discussed in the next section.

6.3 Laser Ablation Mechanism for WJGL

Step 4 in Figure 6.1 is related to prediction of process time and quality as a result of WJGL process. Laser ablation is the removal of material from a substrate by direct absorption of laser energy [131]. The main mechanism of material removal is evaporation. In order to define a material removal model and predict the processing time for a given hole geometry, workpiece material properties should be known, as well as the input process parameters. The material properties of some of the most commonly used nickel-based aerospace alloys are given in Table 6.4 [132] and the nominal compositions of these alloys are provided in Appendix A. Ablation enthalpy

represents all the energy necessary to heat the material from room temperature to vapor phase. The reflectivity value is valid for 532 (nm) wavelength.

Table 6.4 Material Properties

Property	Inco 625	Inco 718	Rene 41	CMSX-4
ρ - density (g/cm ³)	8.19	7.98	7.93	8.65
α - thermal diffusivity (mm ² /s)	3.87	3.89	4.07	3.99
ΔH - ablation enthalpy (J/g)	8938	9024	9202	8615
$\Delta H'$ - ablation enthalpy (J/mm ³)	73.20	72.01	72.97	74.52
R - Reflectivity	0.6	0.6	0.6	0.6

The main material removal mechanisms in the WJGL processing applied to metal alloys is mostly thermal evaporation, due to the nanoseconds pulse regime and respectively low power density values [128]. The ablation phenomenon is governed by thermal penetration depth due to the energy delivered to the material surface. The series of equations shown below can be used to calculate the thermally affected volume (V_{th}) [132]:

$$\delta_{th} = 2.36\sqrt{\alpha\tau_p} \quad (6.5)$$

$$V_{th} = \pi(r_{jet} + \delta_{th})^2 \delta_{th} \quad (6.6)$$

where δ_{th} is the depth of thermal propagation during the laser pulse duration, α is the thermal diffusivity, τ_p is the pulse width, and r_{jet} is the radius of the water jet guiding the laser beam. The graphical representation of the volume can be seen in Figure 6.10.

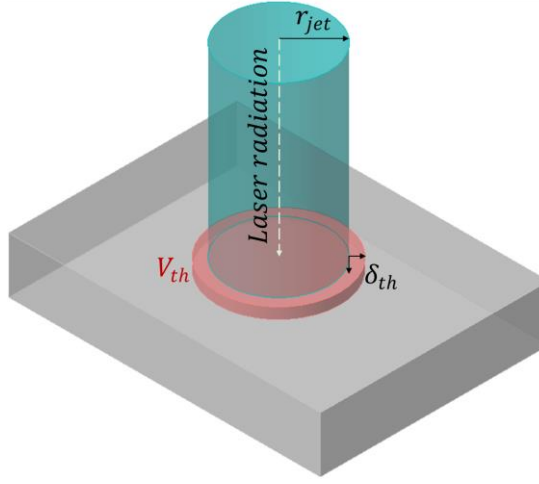


Figure 6.10. Thermally Penetrated Volume from a Laser Pulse

Similarly, the theoretical maximum material removal per pulse (MRP_{th}) in terms of volume for a given set of laser parameters can be calculated using an energy balance equation.

$$MRP_{th} = \frac{\eta E_p}{\rho \Delta H} \quad (6.7)$$

where E_p is the pulse energy, ρ is the density, ΔH is the total vaporization enthalpy per mass, and η is an efficiency parameter including losses through the machine system up to the workpiece surface and at the laser-matter interface (reflectivity). Using Equation (2.1) and Equation (6.4), and considering the absorption of the laser energy on the surface, the efficiency coefficient η can be defined as follows:

$$\eta = (1 - R)(-Mz' + 0.75) \quad (6.8)$$

where R is the reflectivity, and M and z' are the previously defined slope coefficient and normalized distance, respectively.

From a physical point of view, MRP_{th}/V_{th} is considered to describe the ablation process, just like fluence over fluence threshold. The efficiency of the ablation process is reported to be dependent on this ratio for a *top-hat* beam [133].

Equation (6.7) is based on the assumption that all of the laser energy reaches to the surface without interruption and all of the material is vaporized. However, there is generally a recast formation on the machining region, indicating that some of the material is melted and not vaporized. A loss of energy due to plasma absorption above the surface should be expected as well. Thus, the real material removal per pulse (MRP) would actually be less than the theoretical MRP_{th} .

In order to find the actual MRP , direct measurements from the workpiece can be taken. MRR is defined as the removed volume from the material per unit time and can be calculated using Equation (6.9), where Δm , ρ , and t are the mass change of the workpiece, material density and process time, respectively.

$$MRR = \Delta m / \rho t \quad (6.9)$$

Dividing the MRR with pulse repetition rate (frequency), it is possible to obtain the real MRP in terms of volume, as shown in Equation (6.10).

$$MRP = MRR / f \quad (6.10)$$

The MRP is a key value that will be used in the study, since it is easy to calculate using a direct measurement. The real MRP divided by the theoretical MRP_{th} as given in Equation (6.11), describes a measure of the efficiency of the process (η_p). Knowing about this efficiency and the total number of laser pulses on a surface, it is theoretically possible to calculate the process time for a given hole geometry. In practice, it is generally understood that the WJGL process has low efficiency for hole drilling and the reasons are discussed further in this chapter.

$$\eta_p = MRP / MRP_{th} \quad (6.11)$$

6.4 Experiments for Determining the Process Efficiency

The aim of the experiments is to determine how the MRR , MRP , and thus the machining efficiency, is changing with respect to the process parameters.

Understanding about the process efficiency would help predict the material removal for future cases, as explained in the previous section.

In order to understand the material removal behavior, a blind hole drilling experiment is conducted. For all the trials, the water jet nozzle diameter is selected to be 50 (μm), as usual. Spiral toolpath shown in Figure 2.7 is used for drilling the holes. The specimens are ground before the experiments to rule out the initial surface roughness as a factor, which may be important for the first pulses reaching the surface. The weights of the samples are measured before and after the process, using an electronic scale with 0.0001 (g) sensitivity. In order to decrease the measurement uncertainty, 50 blind holes are drilled per trial.

There are eleven factors with at least three levels, which necessitates a huge design of experiment (DOE), as can be seen in Table 6.5. Thus, a full factorial experiment is not possible. In order to simplify the DOE for this case, a modified Taguchi L-27 orthogonal table can be used. The factors and levels for each trial are shown in Table 6.6.

Table 6.5 Factors and Levels for the Experiments

Factors	Level 1	Level 2	Level 3
1. Water pressure (bar)	200	250	300
2. Gas flow (l/min)	0.5	1.0	1.5
3. Power (W) (on the surface)	4	8	12
4. Pulse Width (ns)	200	250	300
5. Frequency (kHz)	10	15	20
6. Material	Inco 625 (1)	CMSX-4 (2)	CMSX-4 (2)
7. Hole Diameter (mm)	0.3	0.4	0.5
8. Stepover (mm)	0.010	0.030	0.050
9. Feed rate (mm/min)	60	120	180
10. Standoff distance (mm)	10	15	20
11. Number of cycles	1	2	3

Table 6.6 Modified Taguchi L-27 Orthogonal Table

Trial	Factor										
	1	2	3	4	5	6	7	8	9	10	11
1	200	0.5	4	200	10	1	0.3	0.01	60	10	1
2	200	0.5	4	200	15	2	0.4	0.03	120	15	2
3	200	0.5	4	200	20	2	0.5	0.05	180	20	3
4	200	1	8	250	10	1	0.3	0.03	120	15	3
5	200	1	8	250	15	2	0.4	0.05	180	20	1
6	200	1	8	250	20	2	0.5	0.01	60	10	2
7	200	1.5	12	300	10	1	0.3	0.05	180	20	2
8	200	1.5	12	300	15	2	0.4	0.01	60	10	3
9	200	1.5	12	300	20	2	0.5	0.03	120	15	1
10	250	0.5	8	300	10	2	0.5	0.01	120	20	1
11	250	0.5	8	300	15	2	0.3	0.03	180	10	2
12	250	0.5	8	300	20	1	0.4	0.05	60	15	3
13	250	1	12	200	10	2	0.5	0.03	180	10	3
14	250	1	12	200	15	2	0.3	0.05	60	15	1
15	250	1	12	200	20	1	0.4	0.01	120	20	2
16	250	1.5	4	250	10	2	0.5	0.05	60	15	2
17	250	1.5	4	250	15	2	0.3	0.01	120	20	3
18	250	1.5	4	250	20	1	0.4	0.03	180	10	1
19	300	0.5	12	250	10	2	0.4	0.01	180	15	1
20	300	0.5	12	250	15	1	0.5	0.03	60	20	2
21	300	0.5	12	250	20	2	0.3	0.05	120	10	3
22	300	1	4	300	10	2	0.4	0.03	60	20	3
23	300	1	4	300	15	1	0.5	0.05	120	10	1
24	300	1	4	300	20	2	0.3	0.01	180	15	2
25	300	1.5	8	200	10	2	0.4	0.05	120	10	2
26	300	1.5	8	200	15	1	0.5	0.01	180	15	3
27	300	1.5	8	200	20	2	0.3	0.03	60	20	1

The main aim for selecting the water jet parameters for the DOE is to find out whether the water blocks the laser light and decrease the machining efficiency for specific conditions. The laser parameters are selected such that the power density is in the safe region as shown in Figure 2.5. Command and RF-off time values are adjusted for each trial so that the power levels at the surface can be achieved as given in Table 6.5. Materials are chosen among the most used alloys considering the sample availability. Hole diameters are selected to cover the most preferred values for cooling holes on gas turbine parts. Stepover values were selected considering the

nozzle diameter. The maximum step size is equal to the nozzle diameter. There is a limit in selecting the feed rate. As the spiral toolpath approaches the center, the motion becomes very rapid and cause vibration on the machine, which may affect the machine axes adversely. The maximum feed rate in Table 6.5 is chosen accordingly. Standoff distance is selected to be a factor in the experiment as well, in order to investigate the water splash back effect and see whether it causes any variation in the results. Finally, there is one important parameter that would affect the machining efficiency and that is the hole depth. However, the hole depth cannot be directly controlled in the machine, due to the nature of laser processing. It can only be determined by choosing the number of cycles for the spiral toolpath. The more the cycle, the deeper the hole becomes.

The setup and an instance from machining can be seen in Figure 6.11. The drilled samples are shown in Figure 6.12.

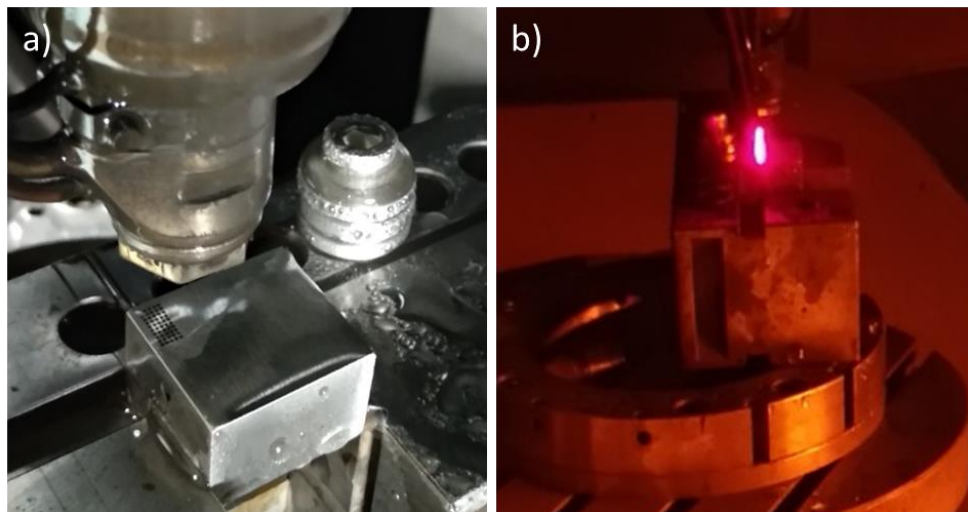


Figure 6.11. a) The setup, b) An instance from machining

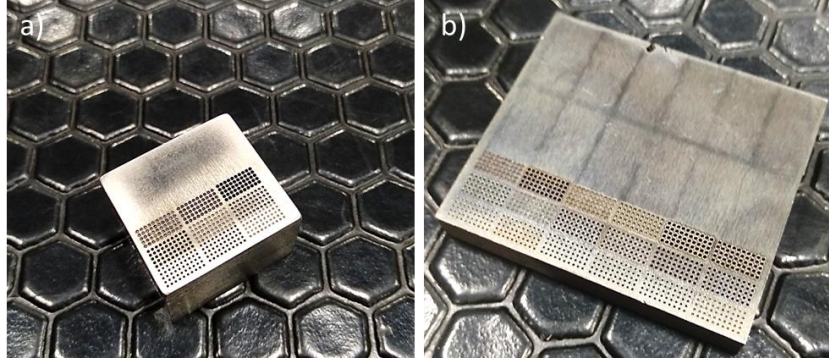


Figure 6.12. a) Inconel 625, b) CMSX-4

Hole diameter, stepover, feed rate and number of cycles differ for each trial. Thus, process time for each hole varies and should be calculated separately for each trial. Process time t can be calculated using Equation (6.12).

$$t = x/F \quad (6.12)$$

where x is the total spiral toolpath length per hole and F is the feed rate. MRR and MRP can be calculated using Equation (6.9) and Equation (6.10), respectively.

A number of different statistical analysis methods are used to find out the significant factors. Minitab 18 software is used for this purpose. Analysis of variance (ANOVA) method is used to calculate the importance of the factors. Statistical comparison tools such as 2-sample t, ANOVA one way, Mann-Whitney, and Kruskal-Wallis are used to determine whether the differences of means or medians for each factor and group are statistically significant. Anderson-Darling normality test and homogeneity analysis are performed on the dataset beforehand to find the most suitable comparison tool for each factor. Similarly, correlation analysis is performed using Pearson and Spearman methods to measure the strength and direction of the relationship between the input and output variables.

The effects of the factors can be seen in Table 6.7. MRP/MRP_{th} is the machining efficiency, as described in Section 6.3. The factor plots of efficiency for certain factors are shown in Figure 6.13.

Table 6.7 Factor Effects – H: High Effect, M: Medium Effect, L: Low Effect

Factors	<i>MRR</i>	<i>MRP</i>	<i>MRP/MRP_{th}</i>
1. Water pressure (bar)	L	L	L
2. Gas flow (l/min)	L	L	L
3. Power (W) (on the surface)	L	L	H
4. Pulse Width (ns)	M	M	M
5. Frequency (kHz)	M	H	L
6. Material	M	M	L
7. Hole Diameter (mm)	L	L	M
8. Stepover (mm)	H	H	H
9. Feed rate (mm/min)	H	H	H
10. Standoff distance (mm)	H	H	H
11. Number of cycles	M	L	M

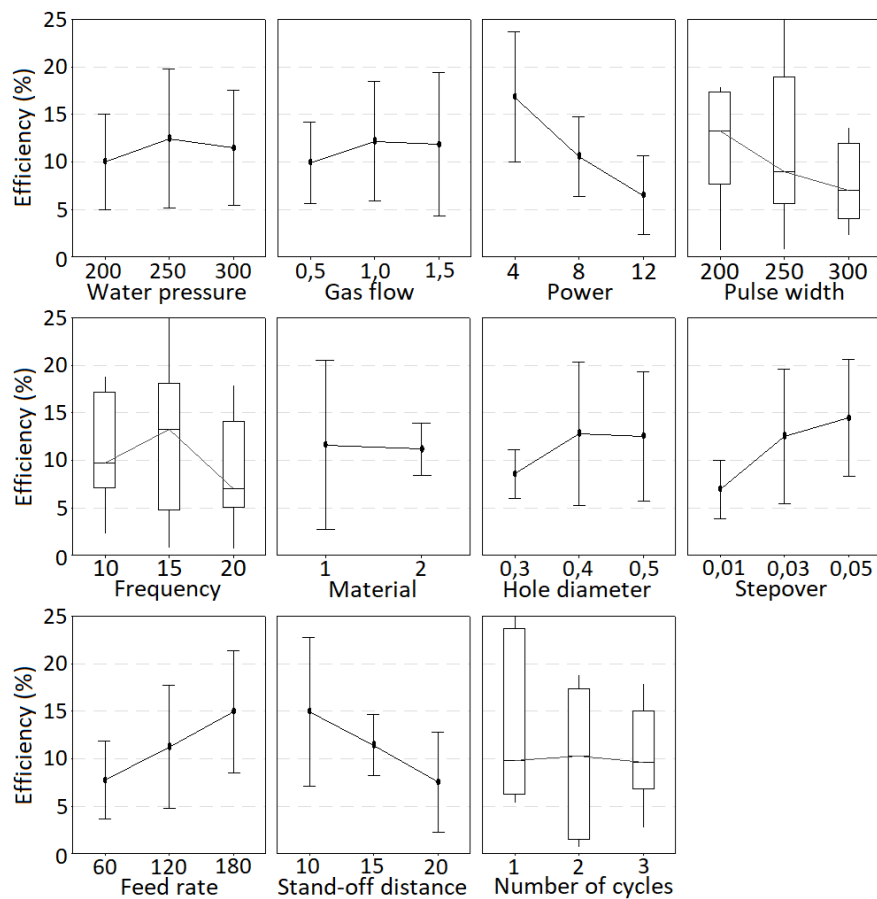


Figure 6.13. Plots of Efficiency

Numerous conclusions can be drawn by inspection of Table 6.7 and Figure 6.13. The water jet parameters (water pressure and gas flow) change the effective cutting length, but as long as the laser energy reaches the surface, they do not seem to play an important role in material removal.

Since the materials are both nickel-based superalloys, which have similar composition and material properties, efficiency remains unchanged. This result was expected and it supports previous findings [132].

The geometric factors, namely hole diameter and number of cycles, are not very significant. This is due to the fact that only superficial material is removed from the surface. According to the previous experience, they would be significant for deeper holes. Another experimental study is planned to correlate material removal to geometric properties, as presented in Chapter 8.

Stepover and feed rate define the pulse overlap and it seems controlling the pulse overlap has a significant impact. The experiments show that it is better to separate the pulses, which means going faster and with a larger spiral stepover is better. Overlapping pulses cause inefficient machining and one should move faster and away from the machining zone. This finding might be related to the shape of the ablation front. For separate pulses, the water jet contact point is smaller (more a disk shape than an ellipse), and the pulse density is actually higher.

The standoff distance also is an important factor for material removal. Even though the laser power is the same on the workpiece surface for all of the trials, efficiency gets lower as the distance gets larger. This phenomenon might be related to the interaction of water jet with the workpiece. More disturbance occurs on the jet in free space due to spray and splashback affecting the aerodynamic flow. It is possible to see a flickering effect just above the machining zone, indicating that the amount of laser energy reaching the surface is decreased for a larger distance.

Regarding the laser parameters (power, pulse width, and frequency), they have some unexpected effects on *MRR*, *MRP*, and efficiency. For example, it is not possible that

power is an insignificant factor for MRR , based on both literature and previous experience. No solid conclusions can be drawn from pulse width and frequency, either. There must be some potential causes hindering the statistical conclusions, which can be deduced as follows:

- i. The range of the selected levels for the experiments may be too narrow.
- ii. Interaction with other factors may have caused undesired variation on the results.
- iii. Number of experiments may not be enough.

In order to increase the number of experiments, a new design of experiment is made by varying the laser parameters in a broader range and fixing the other factors. The factors and their new levels are shown in Table 6.8. A factorial design of experiment is used for three factors with different levels. Two of the factors are fixed each time, while the other factor is changed for each case. Thus, a total of 12 experimental conditions are obtained. Trial conditions are given in Table 6.9. The laser parameters are selected such that the power density I_p shown in Equation (2.4) is in the safe region.

Table 6.8 Factors and Levels for the Experiment

Factors	Levels
1. Water pressure (bar)	200
2. Gas flow (l/min)	1
3. Power (W) (on the surface)	Varying (4-18 W)
4. Pulse Width (ns)	Varying (90-350 ns)
5. Frequency (kHz)	Varying (7-35 kHz)
6. Material	CMSX-4
7. Hole Diameter (mm)	0.4
8. Stepover (mm)	0.020
9. Feed rate (mm/min)	120
10. Standoff distance (mm)	10
11. Number of cycles	1

Table 6.9 Trial Conditions for the Experiment

Trial	Factor		
	Power (on the surface) (W)	Pulse Width (ns)	Frequency (kHz)
1	4	120	12
2	8	120	12
3	14	120	12
4	18	120	12
5	10	90	12
6	10	120	12
7	10	170	12
8	10	350	12
9	10	120	7
10	10	120	9
11	10	120	17
12	10	120	35

The analysis of all the conditions, including the previous design of experiment, yield the results shown in Table 6.10. The laser factor effects on efficiency can be seen in Figure 6.14. As a result of all the experiments, 6 factors out of 11 came out moderately or highly effective for efficiency calculations. Those factors and their effects on *MRR*, *MRP*, and machining efficiency are shown in Table 6.11.

Table 6.10 Factor Effects – H: High Effect, M: Medium Effect, L: Low Effect

Factors	<i>MRR</i>	<i>MRP</i>	<i>MRP/MRP_{th}</i>
Power (W) (on the surface)	H	H	H
Pulse Width (ns)	H	H	H
Frequency (kHz)	M	H	M

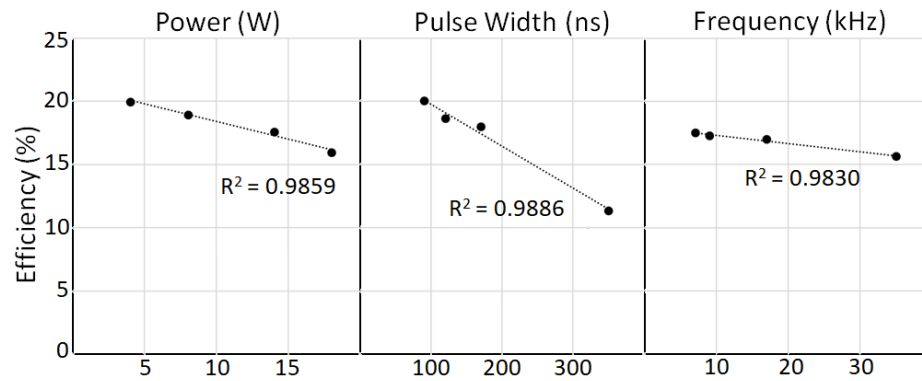


Figure 6.14. Plots of Laser Factors vs. Efficiency

Table 6.11 Change of Factors in order to Increase the *MRR*, *MRP*, and Efficiency

Factors	<i>MRR</i>	<i>MRP</i>	<i>MRP/MRP_{th}</i>
Power (W) (on the surface)	↑	↑	↓
Pulse Width (ns)	↓	↓	↓
Frequency (kHz)	↓	↓	↓
Stepover (mm)	↑	↑	↑
Feed rate (mm/min)	↑	↑	↑
Standoff distance (mm)	↓	↓	↓

Looking at the laser parameters, power should be increased, whereas pulse width and frequency should be decreased in order to increase the *MRP*. This result suggests that increasing the power density (I_p) should increase material removal, as evidenced by Equation (2.4). This result was expected and it supports previous findings [134]. In fact, the fluence ratio for ablation (MRP_{th}/V_{th}) is directly proportional to the power density (I_p). Thus, it is evident that MRP_{th}/V_{th} ratio should be as high as possible for an increased *MRP*. Figure 6.15 shows how the *MRP* is changing with respect to the MRP_{th}/V_{th} ratio for the experimental trials.

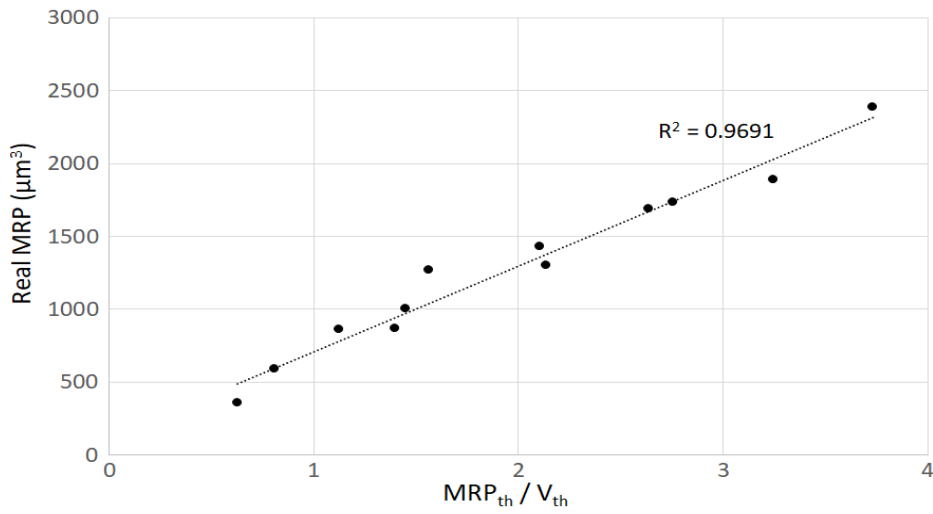


Figure 6.15. MRP_{th}/V_{th} vs. MRP

In order to increase the efficiency; stepover and feed rate should be increased, whereas laser power, pulse width, frequency, and standoff distance should be decreased. Power increase causes inefficiency due to *plasma shielding* effect. Vaporized material starts ionizing above the surface and absorbs the laser energy. The laser feeds the plasma and therefore cannot reach the surface efficiently. Longer pulses cause inefficiency due to the decrease in *peak power*. The same amount of laser energy is applied on a surface for a longer time, which causes the heat to spread to a greater volume instead of focusing on a smaller spot. Instead of vaporization, melting may tend to occur. Higher frequency causes inefficiency due to the fact that laser pulses can be interrupted before reaching the surface. The vapor absorbs the consecutive pulses before there is enough time for the vapor to escape from the machining zone.

If the ultimate aim is to decrease the process time, the *MRR* should be increased as well, but increasing the *MRR* does not necessarily mean that the machining efficiency should be high. Considering Table 6.11, it can be seen that power is directly proportional to the laser power applied on the surface. However, *MRR* cannot be modeled independent of the workpiece material. Since efficiency is

independent of the workpiece material, modeling the efficiency is a more generalized approach.

Taking into consideration both experiments (39 trial conditions total), the efficiency can be modeled as a linear regression equation given in Equation (6.13).

$$\eta_p = 31.76 - 0.929A - 0.03989B - 0.122C + 171.4D + 0.0602E - 0.874F \quad (6.13)$$

where the dummy variables A is the laser power on the surface (W), B is the pulse width (ns), C is the frequency (kHz), D is the stepover (mm), E is the feed rate (mm/min), and F is the standoff distance (mm). The R^2 for Equation (6.13) is 75.62%, and standard error of regression (S) is 3.85. The equation predicts the efficiency (%) within ± 2.6 on average and maximum error is 9.7. The measured and estimated efficiency for the trial conditions are plotted in Figure 6.16.

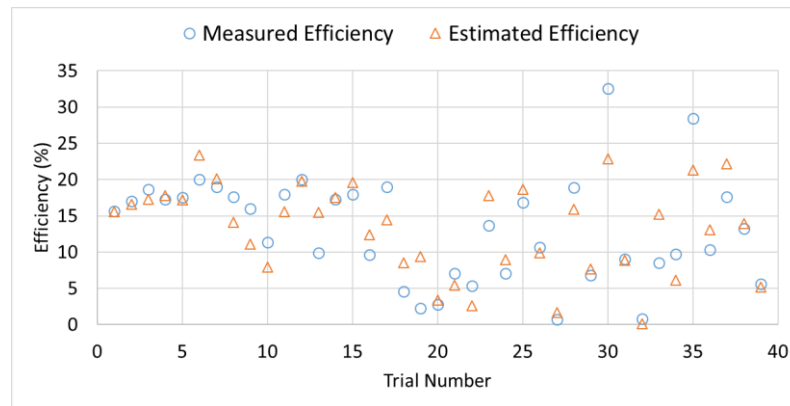


Figure 6.16. Measured Efficiency vs. Estimated Efficiency for Linear Regression

Considering the results, the linear regression approach is not very accurate. It is possible to increase the accuracy by introducing factor interactions, but the equation becomes too complicated and generalization capability of the method is lost. Thus, a nonlinear regression modeling approach is introduced as given in Equation (6.14). The exponential function shows a saturation behavior, which represents a similar trend to the observations.

$$\eta_p = 11.845 \exp(-0.241145A' - 0.210852B' - 0.0212871C' + 0.197393D' + 0.219942E' - 0.30707F') \quad (6.14)$$

The dummy variables in Equation (6.14) are the same as Equation (6.13), but the prime (') symbol indicates that the values are normalized using the formula given in Equation (6.15).

$$y' = \frac{y - \mu}{\sigma} \quad (6.15)$$

where y' is the normalized data point, y is the real value of the data, μ is the mean value of the data, and σ is the standard deviation of the data. The standard error of regression (S) for Equation (6.14) is 3.87. The equation predicts the efficiency (%) within ± 2.8 on average and maximum error is 6.5. The measured and estimated efficiency for the trial conditions are plotted in Figure 6.17.

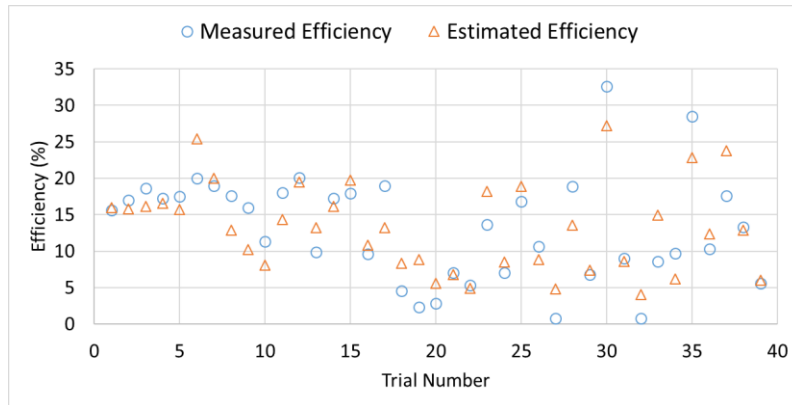


Figure 6.17. Measured Efficiency vs. Estimated Efficiency for Nonlinear Regression

Comparing the linear and nonlinear regression equations, the accuracy is almost the same, but the maximum error for the nonlinear equation is smaller.

6.5 Prediction of Material Removal Using the Developed Model

In order to predict the process time for a given condition, the process input flowchart given in Figure 6.1 can be used. The laser power and pulse width can be estimated using either the ANN or the regression models given in Sections 6.2.2 and 6.2.3. The power density should be checked using Equation (2.4). Similarly, the effective cutting length can be found by the methods described in Section 6.2.2 or 6.2.3. The length should be checked to see whether it satisfies the requirements. Following that, the laser power in the water jet for a specified standoff distance can be estimated using Equation (6.4). The fluence ratio MRP_{th}/V_{th} for ablation should be checked using Equation (6.6) and Equation (6.7). Machining efficiency can be calculated using either Equation (6.13) or Equation (6.14). Following that, the real MRP can be calculated using Equation (6.11). Finally, the process time needed to drill a specified hole can be calculated using Equation (6.9) and Equation (6.10).

From here, it is possible to calculate the number of cycles needed to drill a hole or predict the depth for specified process parameters. The model can also be used for optimization purposes, by changing the input parameters and see how the results change.

As a result of the experiments, the fluence ratio for efficient ablation is found to be directly proportional to material removal. Although the material removal depends on the material type, the machining efficiency is independent of the workpiece material, which is shown to be valid for nickel-based aerospace alloys. Thus, the material removal model is based on the machining efficiency. The limitation of the model is that it would work only for a few number of cycles, which means it is valid for a limited depth. The model will be modified and improved to include the geometrical factors that are mentioned in Section 6.4. The effect of hole diameter and depth on the machining behaviour is covered in Chapter 8.

6.6 Closure

In this chapter, the material removal mechanism of WJGL is investigated and a holistic model is developed including the necessary parameters for micro drilling of nickel-based superalloys. The methods are presented to determine the in-process unknown variables (laser power, pulse width, effective cutting length and power in the water jet), which are used in the material removal model. Laser ablation mechanism is discussed. Significant process parameters affecting the material removal are determined. A methodology is presented to estimate the unknown outputs, such as total process time, hole depth at an instance and number of cycles needed to drill a hole. The developed methodology can be used to determine the machine inputs for the drilling of a new geometry. It can also be used for optimization purposes.

Data collection, modeling, and experiments for all the steps in Figure 6.1 are covered in this chapter. Real-time measurement solutions for the second and third steps are covered in Chapter 7. Regarding the fourth step, effects of the hole geometry to process time and quality is discussed and a real-time acoustic measurement method to monitor the machining conditions is presented in Chapter 8.

CHAPTER 7

EXPERIMENTAL STUDIES FOR REAL-TIME MEASUREMENT OF THE LASER BEAM CHARACTERISTICS⁴

As stated in the previous chapters, there are many noise factors in WJGL process affecting the laser beam characteristics, namely the effective cutting length and the average laser power in the water jet. Although these variables are mainly set by the laser and water jet parameters, uncontrollable factors cause variations. Additionally, the interaction of the laser with the water jet is not fully understood yet. The process involves various nonlinear physical mechanisms, such as laser transmission, absorption, reflection, and scattering in the water jet; convection and radiation of heat; change of temperature-dependent optical and thermal properties of water in time and space; phase changes; fluids and gas dynamics, etc. There are noise factors that should be considered as well, such as water resistivity and temperature, water jet nozzle edge sharpness and roundness, alignment between laser spot and water jet nozzle, gas turbulences, bubble formation in water, water jet disruption, etc. For these reasons, there is currently no mechanistic model in the literature, which describes the laser behavior in the water jet. Measuring the exact values of the laser beam characteristics is crucial for process planning and selection of the machining parameters, such as stand-off distance and number of cycles. In Chapter 6, prediction methods have been presented for these characteristics. In this chapter, two different real-time indirect measurement methods related to image processing and acoustic signal processing are proposed, both of which provide instantaneous readings for the laser beam characteristics in a WJGL machine.

⁴ This chapter is based on [147], which is a published work of the author

7.1 Measurement Methods for Measuring the Laser Beam Characteristics

The distance from the water jet nozzle to the laser breakup point is called as the effective cutting length. This is the region where stimulated Raman scattering occurs. The reflection angle of the laser at the water jet-air interface is constantly disturbed due to the surface fluctuations and at the end of the effective cutting length, the laser beam leaves the water jet almost completely, as can be seen in Figure 7.1 [111]. Since the power level is dropped drastically, machining cannot be performed beyond this point [135].

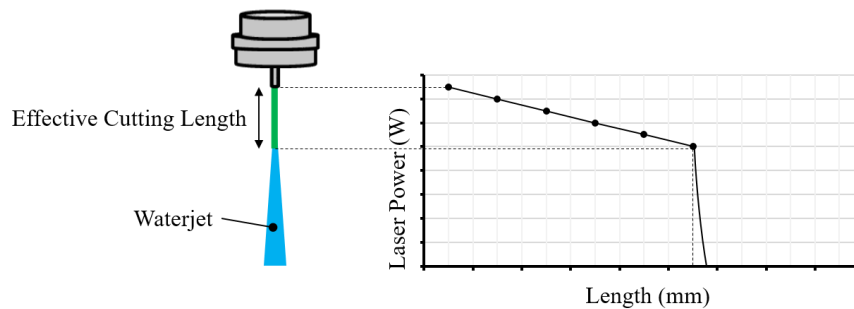


Figure 7.1. Effective cutting length

The effective cutting length and laser power distribution along the water jet should be known before starting the machining process. The certain benefits can be summarized as follows:

- Stand-off distance between the nozzle and the workpiece can be adjusted to make sure the laser energy is reaching the workpiece surface,
- Stand-off distance can be adjusted to protect the back-wall for a hollow workpiece,
- The machining depth capability can be seen, and
- It can be verified that there is enough laser power to ablate material from the workpiece for efficient machining.

Both the effective cutting length and the power level in water at a specific stand-off distance are affected by the laser and water jet parameters, such as laser power, laser frequency, laser pulse width, water jet nozzle diameter, water pressure, and gas flow. Thus, there is a need to perform measurements for both of them for various input conditions.

There is already an external waterproof power meter in the machine for measuring the power level in the water. Although it is possible to use it before starting the process, the measurement takes time, since the nozzle should travel to a different location in the machine and then stay there at the laser on condition for some time to get the power reading. Regarding the effective cutting length measurement, there is no equipment available on the machine to precisely measure it. The distance from the tip of the nozzle to the tip of the visible laser light is generally measured by eyesight taking a fixed plate as reference. This method may result in repeatability and reproducibility errors.

Many different in-situ measurement methods can be applied in the manufacturing domain using sensors. There are variety of sensor technologies in the market, such as electromechanical, semiconductor-based, optoelectronic, piezoelectric, biochemical, electrochemical, or even organic sensors. The selection mainly depends on the sensing function [136]. In this case, the need is to perform inspection to verify specific characteristics of the laser beam. The idea is to select the methods that accomplish this function the best. Vision and acoustic based solutions can be preferred since there is a need of a non-tactile inspection.

Image and acoustic sensors are used for the indirect measurement of the effective cutting length and the laser power in water. The types of the sensors and the setup procedures are described in this section. Design of the experiment is presented as well.

7.1.1 Image sensor – Setup and Application

A mono camera with a CCD sensor recording at 30 frames per second is used to capture the images. Resolution of the camera is 1.3 (MP). The lens attached to the camera has a wide angular field of view so that longer effective cutting length values can be captured. A welding glass is used in front of the lens to filter the intense laser light. The camera is placed in a closed waterproof housing. Camera position and the coordinates of the nozzle in the machine are determined taking into consideration the ease of the setup. The focus of the lens is adjusted to clarify the image, whereas the aperture (f-number) is adjusted for the optimum brightness. The camera is connected to a computer and image analysis is performed with an in-house built software given in Appendix B, which captures the image and performs the necessary calculations. The setup can be seen in Figure 7.2. Preliminary tests showed that the readings from both low laser power and high laser power levels are possible, which fits the purpose.

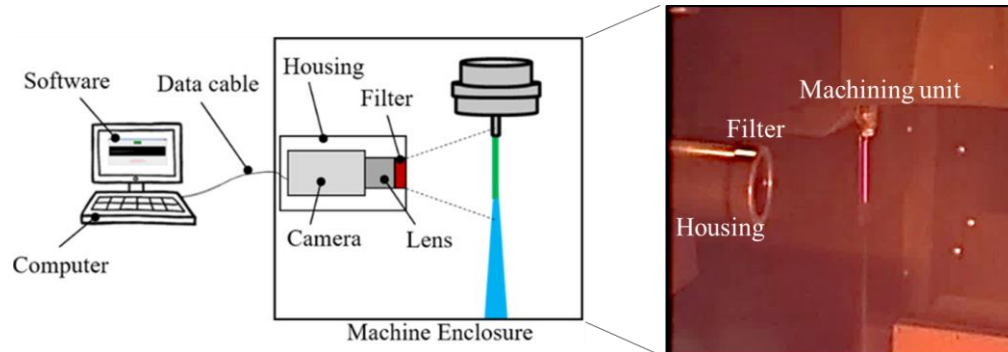


Figure 7.2. Camera setup

7.1.2 Acoustic Sensor – Setup and Application

Acoustic sensors are widely used in manufacturing for process monitoring or diagnostics. Deformation of a material creates elastic stress wave propagation within a medium, which can be detected as acoustic emission in the ultrasonic frequency range [~ 20 -2000 (kHz)] [137]. When used for process monitoring, it is possible to

model the process mechanics depending on the emitted sound. Thus, the output behavior of the process can be predicted for different conditions just by inspecting the acoustic signature.

There are generally two types of acoustic sensors; airborne acoustic emission sensor and structure-borne acoustic emission sensor. Since the laser beam characteristics in the water jet is to be determined in this study, an airborne sensor type should be used. The state-of-the-art membrane type microphones have a maximum 100 (kHz) frequency limit, which is not sufficient for the purpose since the machine background noise would hinder the data collection in this range.

The novel optical microphone manufactured by Xarion works on a different principle. The active element consists of an infrared laser interferometer made up of two opposing miniature mirrors. A momentary refractive index change of the air between the mirrors due to sound pressure causes a shift in optical path length and thus a variation in light intensity reflected back from the interferometer. This variation is converted into an electrical signal. The working principle of the technology is shown in Figure 7.3. Unlike conventional microphones, there are no moving parts. Thus, there is no risk of mechanical ringing effects and it is possible to collect acoustic data in a much wider frequency range. Sound can be detected in air with a bandwidth of up to 1 (MHz) and 146 (dB) noise levels. Furthermore, since the sensing element does not contain metallic parts, it is independent of environmental electromagnetic effects [138].

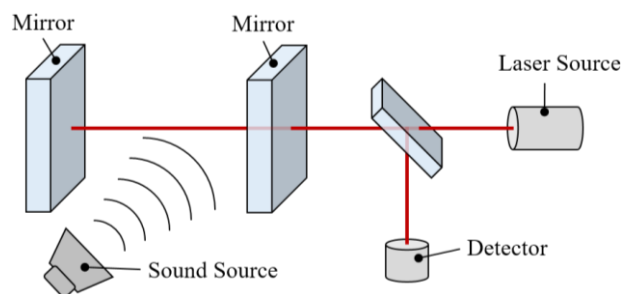


Figure 7.3. Working principle of the optical microphone

There are studies in the literature showing the results of the sensor for different processes, such as powder bed additive manufacturing, laser machining, laser cladding, and laser welding. Prieto et al. [139] used the Xarion sensor for crack detection in laser cladding. Thin-wall formation in stainless steel and thin-layer filling in tool steel were studied with two different experiments. The acoustic signals showing the crack conditions were classified. In both experiments, 200 (kHz) sound frequency levels for the normal process were detected, whereas 600 (kHz) levels were detected for cracks. The cracks were validated by non-destructive testing and the optical microphone proved to be a suitable sensor for real-time detection. Gutknecht et al. [140] compared the process monitoring performance of three different sensor types in the laser powder bed additive manufacturing process. The optical microphone, a pyrometer, and a thermographic camera were used. It was stated that the camera could present intelligible data in the form of a thermal map, but does not have the expected sensitivity. It has been demonstrated that the acoustic sensor is 40 times more sensitive than the camera and 15 times more sensitive than the pyrometer. However, the disadvantage is that while the pyrometer gives more accurate results at different distances, the strength of the signals received differs depending on the position (distance to the melt pool) of the acoustic sensor. Suggestions were made for addressing this shortcoming. Furthermore, a connection between the data received from the sensors and the scanning direction and gas flow has been demonstrated.

The WJGL machining is a noisy process. There is the sound of water pump, mist collector, water jet, and gas flow, which can be heard loudly inside the cabin. It is difficult to detect minor changes in the sound with a conventional acoustic sensor due to the low-frequency ambient noises. Thus, Xarion's Eta250 Ultra is used for the experiments in order to access also the ultrasound frequency range. The sensor head is connected to a signal-conditioning unit, which can change the gain and analog high-pass filter settings. The output is connected to a preamplifier, which is then connected to the High Frequency Measurement System (HF-MES) data acquisition

device for digital conversion and data analysis. The setup can be seen in Figure 7.4. Generally, a high value for the high-pass filter is preferred to cut off the ambient noise. However, the laser frequency is chosen as 10 (kHz) for the experiments as described in the next section and the next closest filter setting is 10 (kHz), which would possess the chance of attenuating the laser frequency signal. Thus, the base value [10 (Hz)] is applied as the filter for the experiments. No additional gain is chosen in accordance with the preliminary tests, since the amplitude of the acoustic signals are already suitable from the start. Sampling rate is chosen as 2 (MHz) (24 bit), in order to get the entire accessible frequency spectrum, considering the Nyquist criteria.

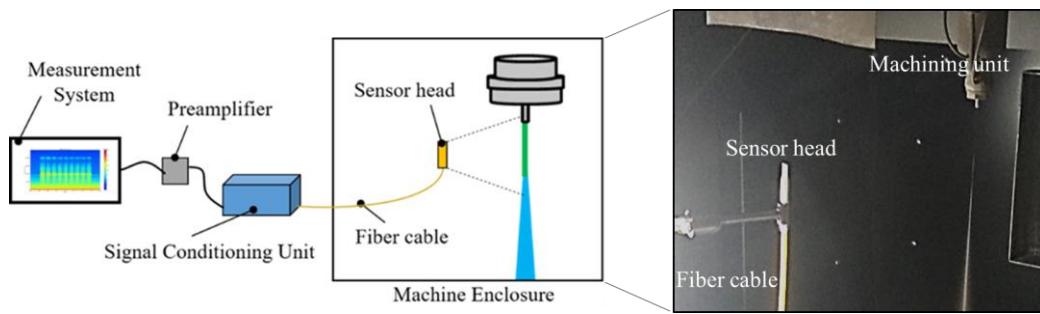


Figure 7.4. Acoustic sensor setup

The studies in the literature mentioned above indicates that the acoustic measurement results are highly position dependent since there is sound attenuation in air. Considering the WJGL machine, staying close to the water jet creates the risk of getting water mist or gas flow inside the sensor head, whereas getting further makes it difficult to detect higher frequencies. Thus, before starting data collection, the optimum location for the sensor is determined. The sensor is bidirectional at higher ultrasound frequencies, so the angle of the sensor head to the processing zone is important as well. The angle of the sensor is adjusted so that it has direct line-of-sight over the water jet. Placing the sensor at 4 cm to the water jet, the sensor did not detect any change between *laser on* and *laser off* conditions. After several tryouts,

the optimum position is found to be 14 (cm) away. The measurement taken from this condition can be seen in Figure 7.5. The acoustic signatures for different conditions can be clearly detected in the plot.

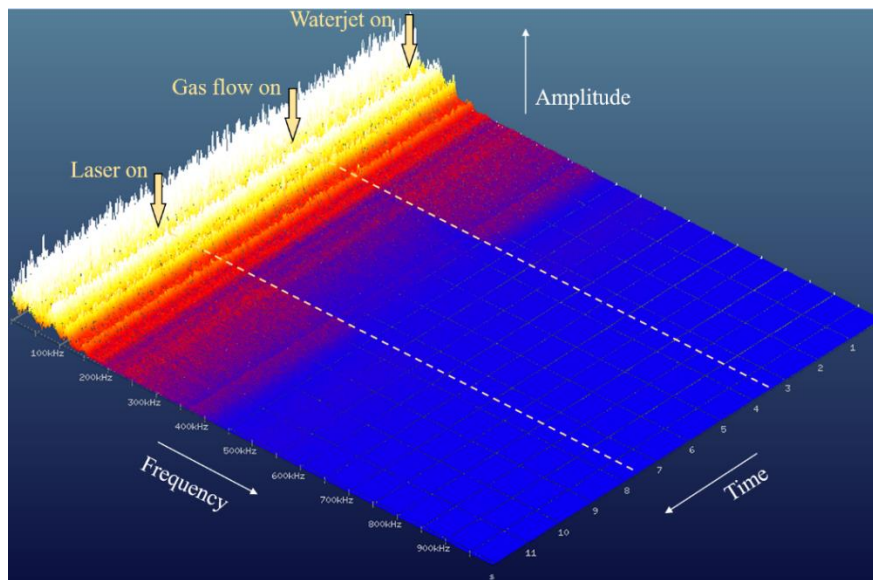


Figure 7.5. Preliminary acoustic measurement [just the water jet is on first-200 (bar), then gas flow is turned on-1 (l/min), and then laser is turned on-80%-2.00 (μ s)-10 (kHz)]

This behavior might be related to the water jet stability. As can be seen from Figure 7.5, firstly the *water jet on* condition without any assist gas creates higher sound frequencies. The *gas on* condition diminishes the higher frequencies, which means there is a more stable water jet. Following that, *laser on* condition disrupts the water jet again, causing sound amplitude in higher frequencies. Thus, it is not the sound of laser-water jet interaction that the sensor is getting, but rather the change of flow of the water jet. The laser excites and disturbs the water jet as described in Chapter 4.2.9. Staying close to the water jet, it is not possible to detect the laser breakup point, since the angle is beyond the sensor's detection range. Thus, staying at a further distance is better for this case.

7.2 Experiments for Measuring the Laser Beam Characteristics

For the study, the adjustable parameters in the machine interface are considered as inputs, which are the water pressure, gas flow, command value, RF-off time, and frequency. The parameters and their chosen values are given in Table 7.1. The range is decided such that it covers the most and least efficient machining conditions [134, 135]. The corresponding power in the water is between 0-25 (W) and pulse width is between 100~450 (ns) for these factor levels. A full factorial Design of Experiment (DOE) is conducted. Thus, data from the camera and the acoustic sensor are collected for 64 different conditions. Nozzle diameter is chosen as 50 (μm) for all the conditions. The power level in the water is measured with a power meter at 10 (mm) stand-off distance. The effective cutting length is measured by eyesight taking a fixed plate as reference. The acoustic signature is recorded for 1 (s) inside the cabin for all conditions when the machine door is closed. The acoustic sensor is used for different cases stated below for comparison purpose.

1. Water jet, gas flow, and laser are all off (reference background noise),
2. Water jet and gas flow are on, but laser is off (reference process noise),
3. Water jet, gas flow, and laser are all on for 64 different experimental conditions.

Table 7.1 Design of experiment

Factors	Level 1	Level 2	Level 3	Level 4
Water pressure (bar)	200	300	—	—
Gas flow (l/min)	1.0	2.0	—	—
Command (%)	50	60	70	80
RF-off time (μs)	2.00	3.00	—	—
Frequency (kHz)	10	20	—	—

7.2.1 Image Processing

The aim is to estimate the effective cutting length and the laser power in water at 10 (mm) stand-off distance via image analysis. The images of the selected cases and the related parameters are provided in Figure 7.6. The power and the length values stated in the figure are the real measured values on the machine. Looking at the images, the brightness of the pixels clearly indicates a correlation to the laser power, and the effective cutting length can be calculated by pixel count.

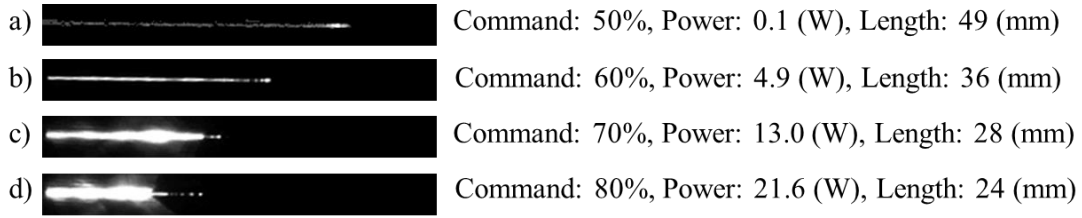


Figure 7.6. Images for different command values [water pressure is 200 (bar), gas flow is 1 (l/min), RF-off time is 2.00 (μ s), and frequency is 10 (kHz)]

A Python script is written to perform the image analysis. The procedure for calculating the effective cutting length is straightforward. Depending on the camera-water jet nozzle distance and the resolution, one pixel size on the screen is found to be 0.154 (mm). The software counts the pixels between the first and the last bright pixel along the length and converts the number of pixels, a , into effective cutting length, ℓ , using Equation (7.1). However, for some cases, it is difficult to detect the endpoint of the Raman scattered region due to the fact that some of the escaping laser beam can be directed back into the water jet due to the small divergence angles [111]. For these cases, the last bright pixel is taken into consideration.

$$\ell = 0.154a \quad (7.1)$$

Similarly, the software finds the average brightness of the pixel values in a certain section around the stand-off distance of 10 (mm) and converts the value to an average power in water. The individual pixel brightness values are between 0 and 65535 without a unit, where zero is pure black and 65535 is pure white. However, in order to model the power in terms of brightness, the factors should be checked one by one to see if only a generalized model is sufficient, or different models are necessary for different conditions. Thus, an ANOVA table is formed for the design of experiment as shown in Table 7.2.

Table 7.2 ANOVA table for the average image brightness

Factors	DOF	S	V	F	S'	P(%)
Water pressure	1	26161039	26161039	1.08	1978726	0.02
Gas flow	1	4963786	4963786	0.21	0	0.00
Command	3	8717709476	2905903158	120.17	8645162537	77.98
RF-off time	1	613064988	613064988	25.35	588882675	5.31
Frequency	1	369789333	369789333	15.29	345607020	3.12
Error	56	1354209531	24182313	—	—	13.57
Total	63	11085898153	—	—	—	100

It can be seen from the table that image brightness is insensitive to the water jet parameters. On the other hand, laser parameters have an influence on the brightness, but the most significant factor is the command input. Since there is a single most significant factor, only a single generalized curve fit equation is considered. The laser power value in the water, P , calculated by the software modeled with Equation (7.2), which takes the average pixel brightness value, p , as the input.

$$P = 6 \times 10^{-4} p \quad (7.2)$$

The data points and the linear fit for the 64 different experimental conditions are shown in Figure 7.7.

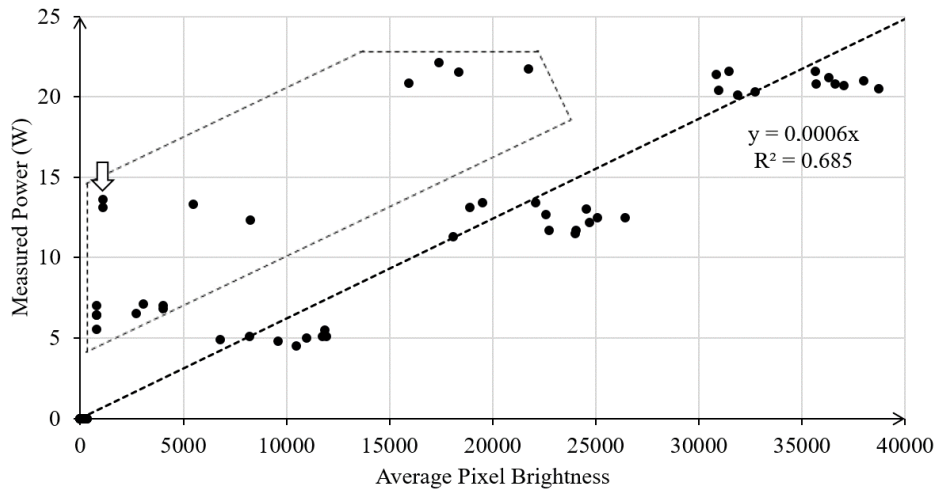


Figure 7.7. Average pixel brightness vs. measured laser power in water (outliers are grouped)

Overall, the fitted curve represents the linear behavior, but there are some outliers as marked in the plot, which decreases the validity of the fit and need an explanation. For example, for the case of Command 70% - RF-off time 3.00 (μs) - Frequency 20 (kHz), the power calculated from the average pixel brightness is only 0.7 (W), whereas the power meter measurement shows 13.6 (W), as marked with an arrow in Figure 7.7. Looking at the images, the brightness is indeed very low when compared to similar conditions, as shown in Figure 7.8.

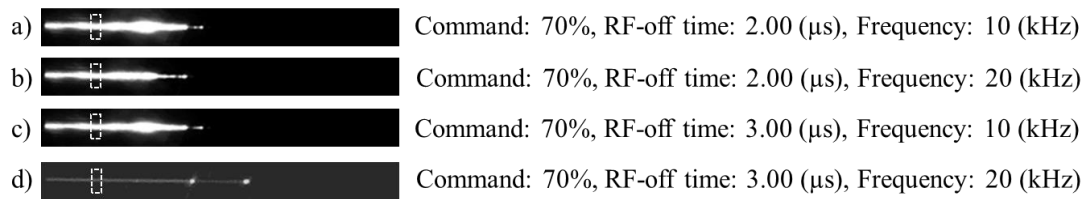


Figure 7.8. Images for different laser parameters [water pressure is 200 (bar), gas flow is 1 (l/min), and the selected area is where the average brightness of the pixel values are calculated]

Thus, this is not an error coming from the methodology, but it is related to a physical phenomenon. The power level is high in the water, but the brightness that is captured by the camera is low. Looking at the specific outlier condition in Figure 7.8d, it can be seen that the pulse width is measured as 437 (ns). Similarly, all the outliers shown in Figure 7.7, has pulse width values above 375 (ns) and laser frequency set at 20 (kHz), whereas good fit cases have pulse width values between 100-320 (ns). High laser frequency values and the pulse energy applied for a longer time decreases the peak power and the power density, which cause the laser-water jet interaction and Raman scattering to occur less severe than expected. This finding indicates that the power calculation from the image analysis is valid for a certain range of parameters and must be used with caution, since the brightness is decreasing with the increasing pulse width and frequency. Another non-linear curve fit may also be considered for the cases, where the power density is low. The coefficient of determination (R^2) value for Equation (7.2) for all the data points is 68.50%. Removing the outliers, the curve fit equation does not change, but the R^2 becomes 97.06%. The variation of the pixel brightness values around the clusters in Figure 7.7 are due to the interaction of the experimental factors given in Table 7.1.

7.2.2 Acoustic Analysis

The aim is to estimate the laser power in the water at 10 (mm) stand-off distance via acoustic analysis. In order to achieve this task, the correlation between machine parameters and sound amplitudes and frequencies should be determined so that accurate predictions can be made with acoustic measurements. Spectrum analysis is performed on the experimental data collected from the sensor. Features are extracted from the signals to facilitate pattern recognition. In this way, the data received from the sensor can be matched with the process parameters.

The first step is to check whether the water jet, gas flow, or laser on conditions make a significant difference in the Power Spectral Density (PSD). The related conditions are compared in Figure 7.9. The amplitude in arbitrary units (a.u.) are based on a

logarithmic scale in the plots since this is more convenient to compare the whole frequency range visually.

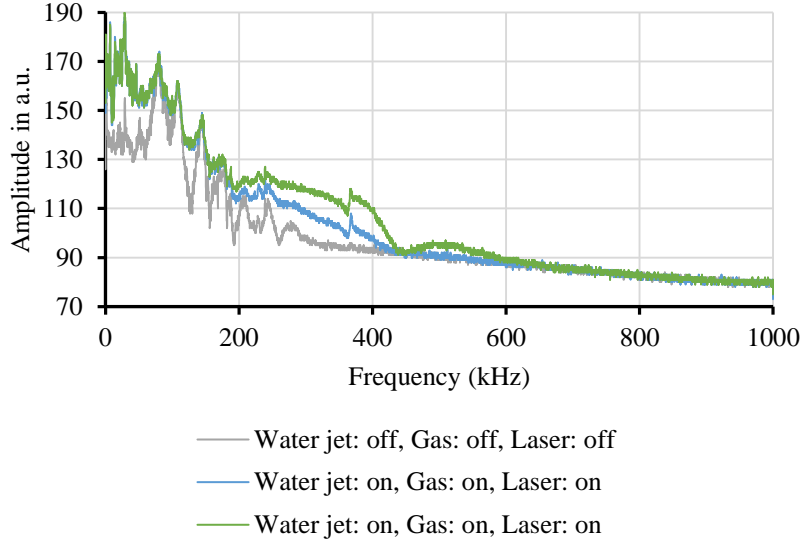


Figure 7.9. PSD comparison of different conditions

It can be seen from the plot that the water jet sound suppresses the acoustic signals resulting from the laser in the low frequency range [<200 (kHz)]. Especially the 10 (kHz) laser frequency cannot be distinguished. However, the difference is significant for the 200 - 600 (kHz) range, which means that the acoustic emission sensing can be used for comparison of different conditions in this range. The higher frequencies [>600 (kHz)] are damped most probably due to the distance of the sensor to the water jet nozzle and the sound attenuation in air.

Figure 7.9 reveals a peak around 365 (kHz) when the water jet and gas are on. Other than that, the frequency plot more or less follows the same pattern as the idle condition. This specific frequency is the about the same as the natural frequency of the nozzle, f_n , which can be calculated by Equation (7.3) [141].

$$f_n = c / 4L \quad (7.3)$$

where c is the speed of the sound in water, which is 1450 (m/s) [142], and L is the length of the chamber, which is the distance between the water jet nozzle and the glass [~ 1 (mm)]. Equation (7.3) gives 362.5 (kHz) as the nozzle natural frequency, which is very close to the observation. Thus, the water jet frequency is in resonance with the natural frequency of the nozzle. The harmonics of the fundamental frequency can be spotted faintly, but they are mostly suppressed or damped, as mentioned earlier. The amplitude of the signals increase when the laser is turned on. Furthermore, another hill pattern around 510 (kHz) is observed. The amplitude of these frequency levels might be of interest for pattern recognition.

The next step is to detect the importance of each factor on the acoustic signal separately. Thus, an ANOVA table is formed for the design of experiment as shown in Table 7.3.

Table 7.3 ANOVA table for the average sound amplitude between 200-600 (kHz)

Factors	DOF	S	V	F	S'	P (%)
Water pressure	1	80.63	80.63	45.07	78.84	10.26
Gas flow	1	452.59	452.59	252.99	450.80	58.67
Command	3	130.95	43.65	24.40	125.58	16.34
RF-off time	1	2.99	2.99	1.67	1.21	0.16
Frequency	1	1.00	1.00	0.56	0.00	0.00
Error	56	100.18	1.79	—	—	14.57
Total	63	768.36	—	—	—	100

It can be seen from the table that the sound amplitude is insensitive to the laser parameters, except the command input. On the other hand, water jet parameters have an influence on the acoustic signals, especially the gas flow. These findings suggest that different models may be needed to model the acoustic behavior for different water pressure and gas flow levels. The acoustic signatures are observed for each condition by changing one factor at a time and keeping the other factors constant. Figures 7.10 and 7.11 shows the PSD plots for different water jet and laser parameters, respectively.

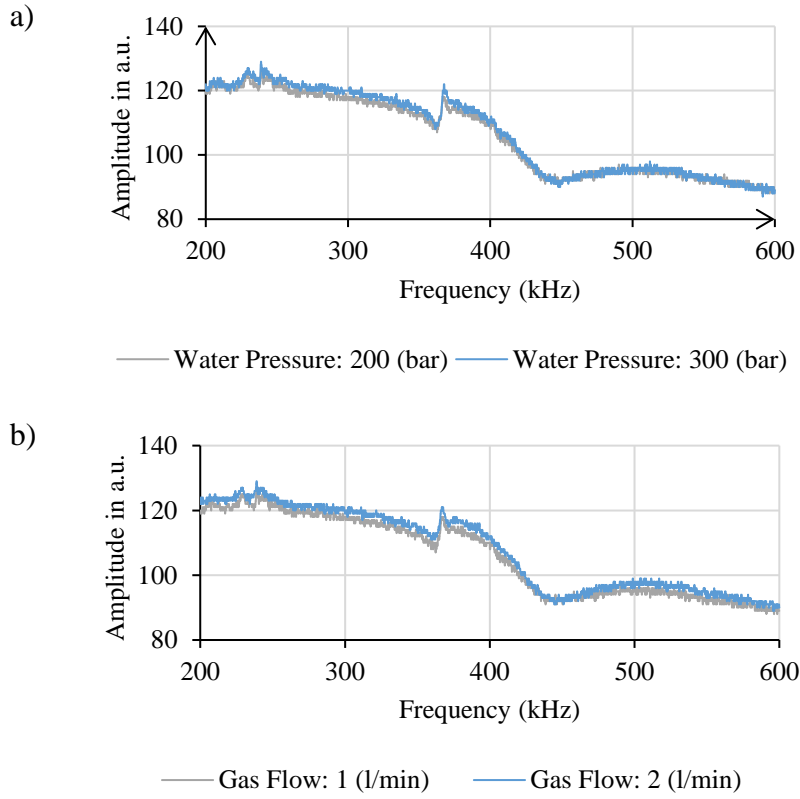


Figure 7.10. PSD plots a) Water pressure comparison [gas flow is 1 (l/min), command is 80%, RF-off time is 2.00 (μ s), and frequency is 10 (kHz)], b) Gas flow comparison [water pressure is 200 (bar), command is 80%, RF-off time is 2.00 (μ s), and frequency is 10 (kHz)]

Water Pressure. The PSD does not show any differences between two different water pressure levels in terms of frequency levels, as can be seen in Figure 7.10a. However, the signal amplitude slightly differs. Thus, the process gets noisier in the ultrasound range with increasing water pressure, but there is no other resonance frequency formation in this range.

Gas Flow. The PSD plots for gas flow of 1 (l/min) and 2 (l/min) can be seen in Figure 7.10b. The average signal amplitude is higher for larger gas flow values. This finding is believed to be related to the water jet behavior, and not the gas flow itself. Increasing the gas flow shortens the water jet breakup length, which in turn decreases

the effective cutting length. The disturbance of stable water jet increases the sound amplitude. This situation is verified by turning off the gas completely. The same sound level is obtained as the 2 (l/min) gas flow condition. Thus, the process gets noisier in the ultrasound range with increased gas flow due to the disturbance of the water jet, and no other resonance frequency formation is observed.

Command. The PSD plots for different levels can be seen in Figure 7.11a. The command value dictates the laser power level. Thus, the plots clearly reveal the correlation between power in the water and the sound amplitude, as expected. There is no other resonance frequency depending on the power level, but the process gets noisier in the ultrasound range with increasing laser power.

RF-off time. The RF-off time value dictates the laser pulse width. In order to make a comparison, the conditions are selected such that the laser power and the laser frequency levels are the same, but the pulse width values are different. The PSD plots for the selected conditions can be seen in Figure 7.11b. The plots mostly overlap. No significant correlation is found between the pulse width and the acoustic emission from the water jet within the experimental process window.

Frequency. In order to make a comparison, the conditions are selected such that the laser power and the laser pulse width levels are the same, but the laser frequency values are different. The PSD plots for the selected conditions can be seen in Figure 7.11c. The plots mostly overlap. No significant correlation is found between the laser frequency and the acoustic emission from the water jet within the experimental process window.

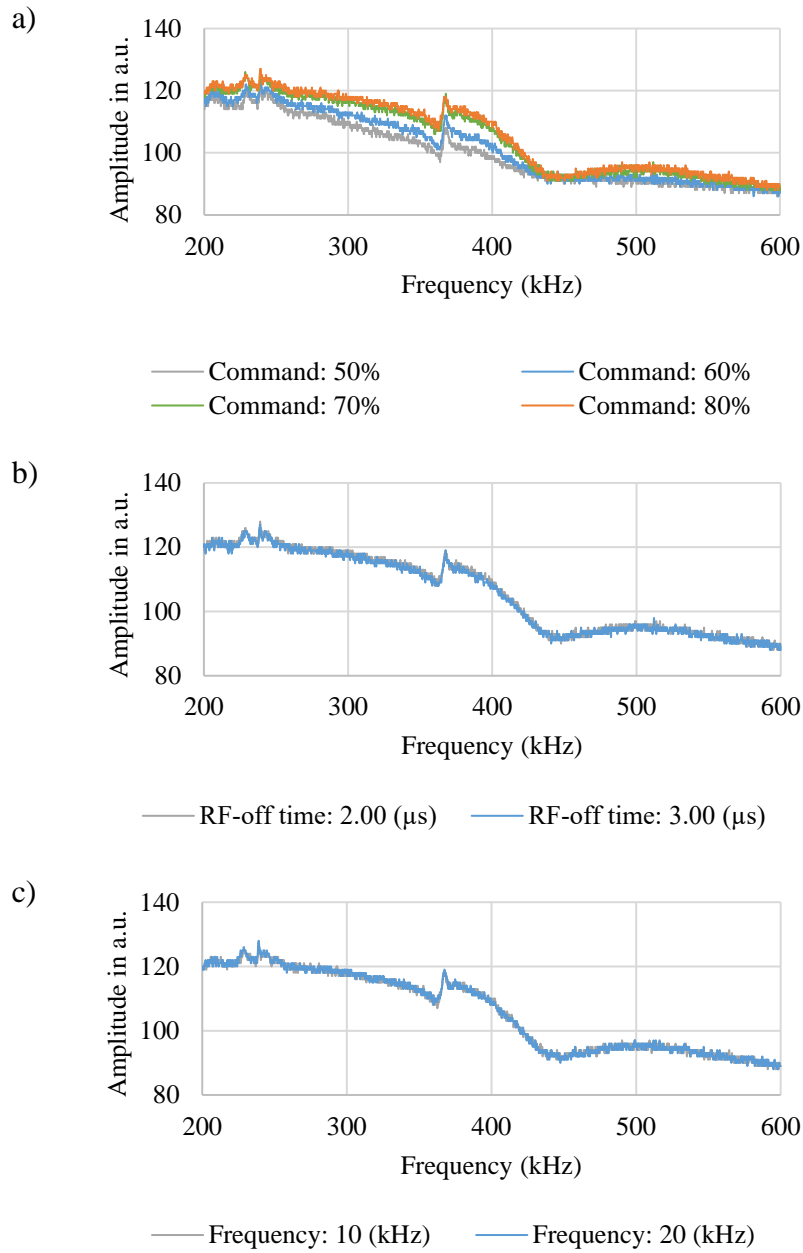


Figure 7.11. PSD plots a) Command comparison [water pressure is 200 (bar), gas flow is 1 (l/min), RF-off time is 2.00 (μs), and frequency is 10 (kHz)], b) RF-off time comparison [water pressure is 200 (bar), gas flow is 1 (l/min), command is 80%, and frequency is 20 (kHz)], c) Laser frequency comparison [water pressure is 200 (bar), gas flow is 1 (l/min), command is 80%, and RF-off time is 2.00 (μs)]

Finally, the acoustic signals for the laser on condition can be matched with the laser power level in water. Since there are more than one significant factor, multiple curve fit equations are considered. Different water pressure and gas flow levels are taken into consideration since they have effects on the acoustic signals as mentioned earlier. The plots are shown in Figure 7.12. The curve fit equations and R^2 values are also visible on the plots.

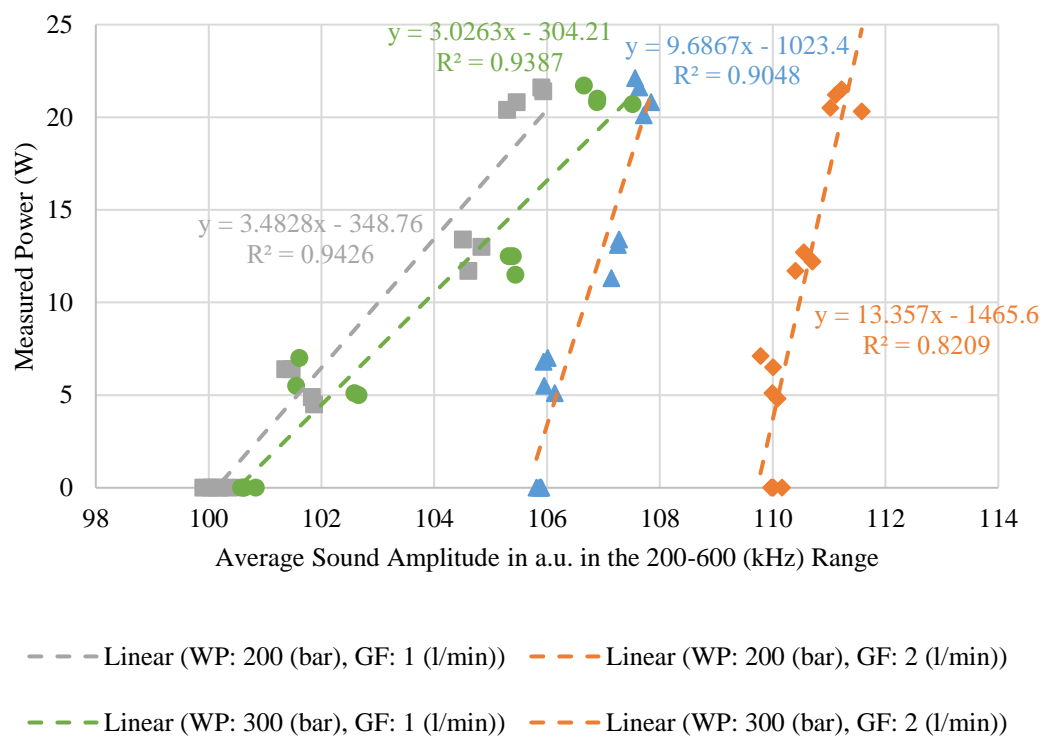


Figure 7.12. Average sound amplitude in a.u. in the 200–600 (kHz) range vs measured laser power in water

The first observation about the plots is the effect of gas flow. As the value gets higher, there is a shift to higher amplitudes, which necessitates a different curve fit to be adapted for this louder range. In addition, the linear curves are steeper for high

gas flow, which means that the laser power is capable of generating less acoustic signal difference since the sound is suppressed by the disrupted water jet in this range.

Secondly, there are less outliers in Figure 7.12 when compared to Figure 7.7 and R^2 value is better for all the data points (90.18% on average), which means that the acoustic analysis method is more robust than the image analysis method in terms of detecting the laser power in the water.

7.3 Closure

Image processing and acoustic signal processing for detecting the effective cutting length and the average laser power in the water jet in a WJGL machine are presented for the first time in literature. The setup for the two methods are shown and the obtained results are compared and discussed in light of the physical aspects of the WJGL process.

It can be concluded that the image processing method is successful in terms of detecting the effective cutting length, but the acoustic emission analysis method is performing better for detecting the laser power level in water. Image analysis is insensitive to water jet parameters, whereas acoustic analysis is insensitive to laser parameters, except the laser power.

It should be stressed that the presented models are valid for the shown setup and they would differ depending on the type or positioning of the equipment. Thus, the equations should be calibrated for a different setup since the acquired images and acoustic signals would change. Another fact is that the obtained and analyzed results are valid for the selected process window only. Factor levels beyond the experiments shown here might have significance on the image or acoustic analysis methods. It is also possible to correlate the laser power in water for different stand-off distance values. In the study, 10 (mm) is taken as a baseline just to show the methodology. It is only a matter of data collection to make the models work for different values.

The developed methods offer many opportunities. For example, a feedback system can be introduced on the machine, in which the operator inputs the desired length and/or power value in the interface. Using real-time indirect measurement by image/acoustic analysis and active feedback control, machine parameters may change automatically to meet the desired output.

Since the acoustic emission analysis provided successful results, the use of an optical microphone in the WJGL machine offer other possibilities, such as breakthrough detection, monitoring the efficiency of machining, and real-time hole depth measurement, which are covered in the next chapter.

CHAPTER 8

INVESTIGATION OF EFFECTS OF THE HOLE GEOMETRY ON MACHINING BEHAVIOUR

One important question about the process is, how much of the laser energy can be really absorbed by the workpiece at the bottom of a blind hole? The answer mainly depends on the diameter of the hole and the depth that machining takes place. As the hole gets deeper or the diameter gets smaller, blockage may occur due to the high pressure water accumulating or splashing back from inside the cavity, causing the machining efficiency to drop significantly. Thus, there is a limit to the aspect ratio of the holes that can be drilled with the WJGL technology. Generally, it is possible to drill any hole which is larger than the water jet diameter, but the obtainable depth differs for each case. Unfortunately, there is not a definitive formula that provides a prediction for the material removal depending on the hole geometry. Trials should be performed to observe the behaviour.

Generally, the material removal models for laser ablation only concentrate on the first few laser shots or layers on the surface, and as the hole gets deeper, the models lose their validity since the uncertainties and assumptions in the models build up and cause deviation. The methodology presented in this chapter provides the means to understand the material removal in a cavity, depending on its size. Experiments are conducted with different hole diameter values to explore the process limits and find out the machining efficiency depending on the hole depth. The minimum hole diameter that can be drilled for a specific thickness or the maximum reachable depth for a specific hole diameter shall be revealed as well. Additionally, a real-time measurement method based on acoustic signals is proposed. The experiments show a correlation between ultrasound emission and material removal depending on the hole geometry in a water jet guided laser machine. The measured sound signatures

are correlated to the hole depth, machining efficiency, and hole breakthrough. Understanding effects of the hole geometry on drilling behaviour and in-situ monitoring of the machining conditions serve the purpose of predicting the expected process time and quality more accurately, which is the fourth step in Figure 6.1.

In the next sections, the properties of the acoustic measurement equipment is presented. Following that, the experimental methodology is explained. Finally, the measured results and analyses are shared and discussed.

8.1 Optical Microphone

Laser ablation generates ultrasound waves. The characteristics of these waves depend on the mechanisms involved in the laser-material interaction. In every case, the ultrasound waves propagate through both the material and the surrounding atmosphere [91].

Acoustic emission analysis as applied to laser drilling is not a new subject. Many studies have found a correlation between the process and acoustic emission waves in air. The studies mostly cover the human audible range [20 (Hz)-20 (kHz)] [143] or a little bit more [up to 40 (kHz)] [54]. However, there are lots of loud noise sources in this frequency range in a WJGL machine, such as the operation of water pump, mist collector, water jet, and gas flow. Thus, it is not possible to detect minor changes in acoustic emission under such circumstances with the conventional microphones. They can only work in a low frequency range due to the mechanically vibrating components that can have limited deformation response to acoustic pressure.

In the WJGL process, when the laser is on and ablation takes place, collapsing vapour flume emits sound waves that can be detected in high frequencies. When the laser is off, or in case it is blocked, there is another sound emission resulting from the interaction of water jet and the workpiece as well. Thus, if it is possible to distinguish these sound waves, it may be possible to tell when the laser-material interaction happens. The method would provide an indirect measurement of the machining

efficiency for a spiral cycle. As a result, a proper efficiency coefficient can be found and applied to the theoretical material removal models, improving the machining time predictions for a specific hole diameter and depth. Optimization would be possible by comparing different laser and/or water jet parameters as well. However, since the WJGL is a noisy process, the equipment for acoustic analysis should be selected accordingly.

The optical microphone, as stated in Chapter 7, is a suitable acoustic measurement device for the task. Working principle of the sensor depends on the refractive index change of the medium due to the sound pressure. When the sound waves alter the optical density, the difference can be detected by a laser-probed interferometer. The schematics of the system can be seen in Figure 8.1. There is a cavity, which is 2 (mm) in length, enclosed by a parallel pair of partially reflective mirrors. An infrared laser is utilized in the sensor, which is capable of detecting the slightest light intensity change in between the mirrors. Refractive index change of the air causes a variation in light intensity due to the sound pressure waves and this variation is converted into an electrical signal. The novel optical microphone has no moving or metallic parts, which eliminates the risk of mechanical resonances or electromagnetic effects. Thus, detection of a significantly broader frequency range is possible, when compared to the conventional sensors [137, 144].

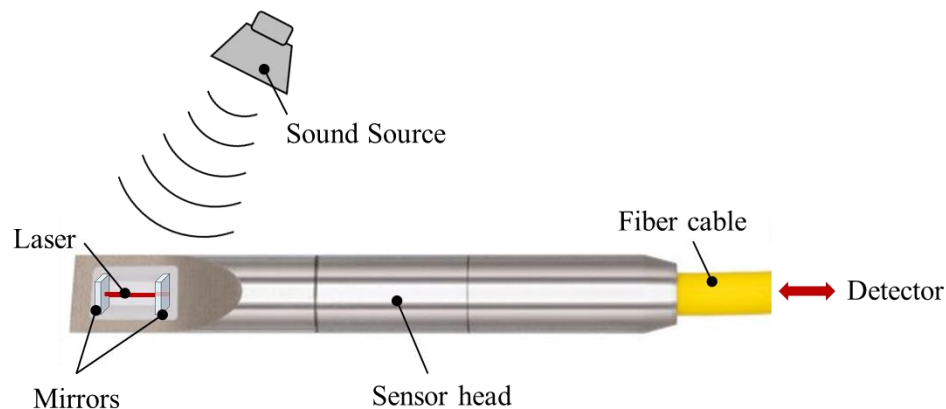


Figure 8.1. Working principal of the optical microphone

In summary, acoustic signatures carry valuable information about the process and the idea of a non-contact sensor capturing the airborne ultrasound signals provides flexibility in a manufacturing environment. There is the chance to avoid the interference of the low frequency ambient sound using this acoustic process monitoring method and obtain more robust measurement results. Thus, the optical microphone technology has a potential when used with a WJGL system.

8.2 Details of the Experiments and Measurements

8.2.1 Drilling Experiments

WJGL machining efficiency depends on many factors, but it is generally independent of the material type. The inefficiency depending on the hole depth is mostly related to geometrical interferences due to the water jet interruption. Thus, the drilling experiments are performed on a single alloy and the selection is made based on availability. 10 (mm) thick coupons made of Inconel 625 alloy are used for the purpose. Spiral toolpath is preferred to drill the holes with a water jet nozzle size of 50 (μm). The selected hole diameters range between 0.2 – 1.0 (mm), which cover the range of cooling hole requirements on aerospace components. In order to see how the material removal is changing with respect to the hole depth, the number of spiral cycles are repeated starting from 1 cycle up to 50 cycles. Thus, a total of 450 holes are drilled on the samples. The design of experiment is summarized in Table 8.1 and the photo of the drilled samples is shown in Figure 8.2.

Table 8.1 Design of experiment

	Hole Diameter Values (mm)								
	Ø0.2	Ø0.3	Ø0.4	Ø0.5	Ø0.6	Ø0.7	Ø0.8	Ø0.9	Ø1.0
Number of Cycles	1	1	1	1	1	1	1	1	1
	2	2	2	2	2	2	2	2	2
	3	3	3	3	3	3	3	3	3

	50	50	50	50	50	50	50	50	50

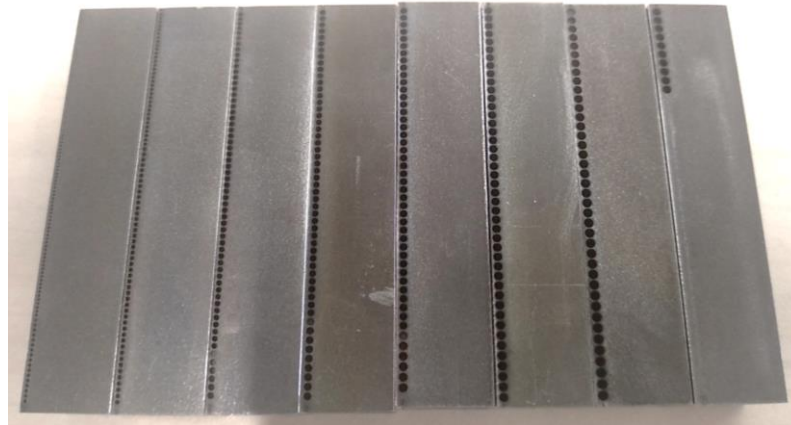


Figure 8.2. Photo of the drilled samples

The first aim is to observe the drilling depth capability for each selected hole diameter. Since the aim is to see the process limits, the most efficient parameters for WJGL hole drilling are selected based on the previous experiences and the best practices. The list of parameters and their values are shown in Table 8.2. The laser break-up length in this condition is found to be approximately 25 (mm), which is

enough to drill a 10 (mm) thick sample. The second goal is to observe how the hole depth is evolving by each spiral cycle for different hole diameter values. Thus, the process efficiency depending on the diameter and depth can be found out. Hole morphology inspection and depth measurements are done with the micro-focus X-ray computed tomography (CT) device. The scan resolution of the system is ~20 (μm). Software of the CT device is used on the reconstructed 3D volume to analyze the vertical cross-section of the holes.

Table 8.2 List of parameters and their values

Parameters	Values
Water pressure (bar)	250
Gas flow (l/min)	1
Laser power (W)	35
Pulse width (ns)	200
Frequency (kHz)	10
Stepover (mm)	0.05
Feed rate (mm/min)	180
Stand-off distance (mm)	10

8.2.2 Acoustic Measurements

The frequency range of the microphone is 10 (Hz) – 1 (MHz). Since the sensor is small and the sensor head is optically fiber-coupled, it can be mounted in the WJGL machine close to the processing zone. The sensor head is connected to a signal-conditioning unit, a preamplifier, and a data acquisition device, respectively. The setup in the machine can be seen in Figure 8.3.

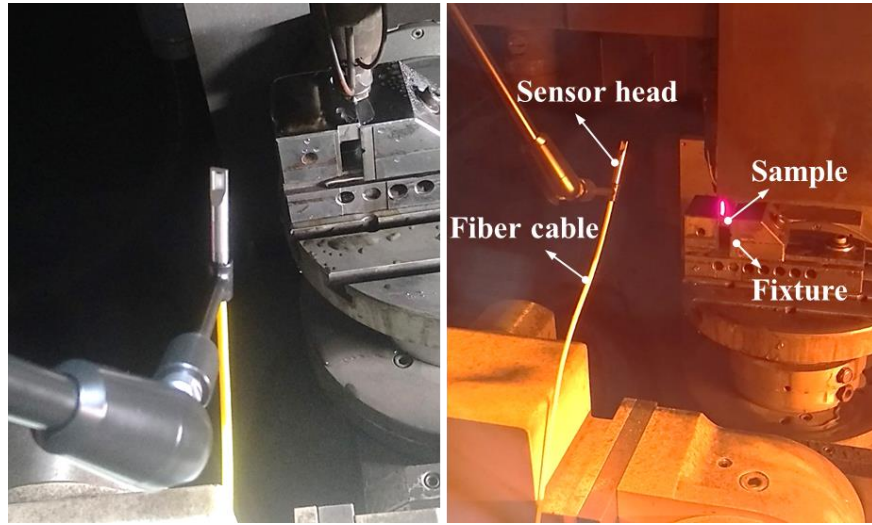


Figure 8.3. Acoustic measurement setup

200 (kHz) for the high-pass filter is selected to cut off the ambient noise. This also means reducing the sound level for the laser frequency, which is 10 (kHz). However, preliminary trials showed that the amplitude of the acoustic signals are only suitable at this level and using a -12 gain. Lowering the filter or increasing the gain causes the ambient noise to suppress the laser ablation sound. Orientation and distance of the microphone to the processing zone is critical as well. There is sound attenuation in air especially for high frequencies. For example, an acoustic wave with a frequency of 1 (MHz) is attenuated by 160 (dB/m) in air [145], which means a huge drop in the sound pressure. Thus, it is better to stay close to the processing zone. However, staying too close to the water jet in a WJGL machine generates the risk of getting water inside the sensor head. After several trials, the optimum location of the sensor head is found to be 16 (cm) away and the orientation of the sensor is adjusted so that it has direct line-of-sight to the processing zone.

The acoustic emission can be monitored in real time in the form of Short-time Fourier transform (STFT), while a computer containing a field-programmable gate array acquires the signal. Changes in the refractive index of the air inside the sensor head measured by the interferometer is a continuous analog quantity. The analog signal

from the sensor head is digitized with a selected sampling rate in the data acquisition system. The time-discrete and amplitude-discrete voltage signal is the primary data for analysis. The data can either be displayed as a raw time-domain signal or be visualized using STFT as a spectrogram, which consists of frequency, time, and amplitude axes. The raw acoustic data can be exported as a binary file as well, which contains the amplitude values for the sampled discrete time units [146]. In this study, the sampling rate is chosen as 24 bit / 2 (MHz), which is the sufficient resolution according to Nyquist criterion. For further analysis, Python is used to obtain the Power Spectral Density (PSD) and energy plots by using the extracted data points.

The aim for the acoustic measurements is to see how the sound pressure and/or the frequency is changing within the spiral toolpath depending on the hole diameter and the depth. In order to do that, the sound data for each spiral cycle (from 1 to 50) for each hole diameter [between 0.2 – 1.0 (mm)] is recorded. The optical microphone is manually triggered to start and stop the recording throughout the 50 cycles, but 1 (s) dwell is introduced between each cycle to differentiate the sound data.

8.3 Results of the Drilling Experiments

8.3.1 Process Limits

One of the objectives of the experiments is to see the maximum drillable depth for the selected hole diameter values. The depths are measured from the vertical cross-section images taken by the CT device. The maximum depth at the blind cavity is measured for each case. Figure 8.4 shows how the depth is evolving for a specific diameter.

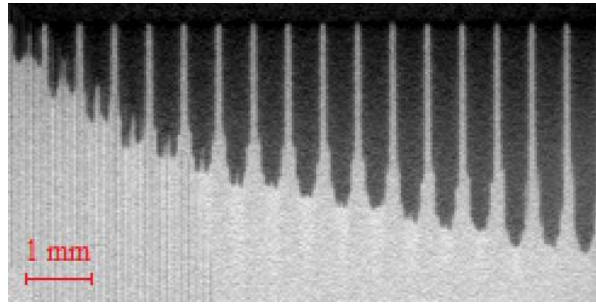


Figure 8.4. CT cross-section image of $\varnothing 0.4$ (mm) hole from 1 to 17 cycles

There are two main observations that can be inferred from the experiments. First, the hole depth values are showing a saturation behaviour as the number of cycles are increased. Figure 8.5 shows the saturation behaviour of the hole depth depending on the hole diameter. It is expected to see that the material removal gets harder as the cavity is getting deeper. The reasons are discussed in more detail in the next section.

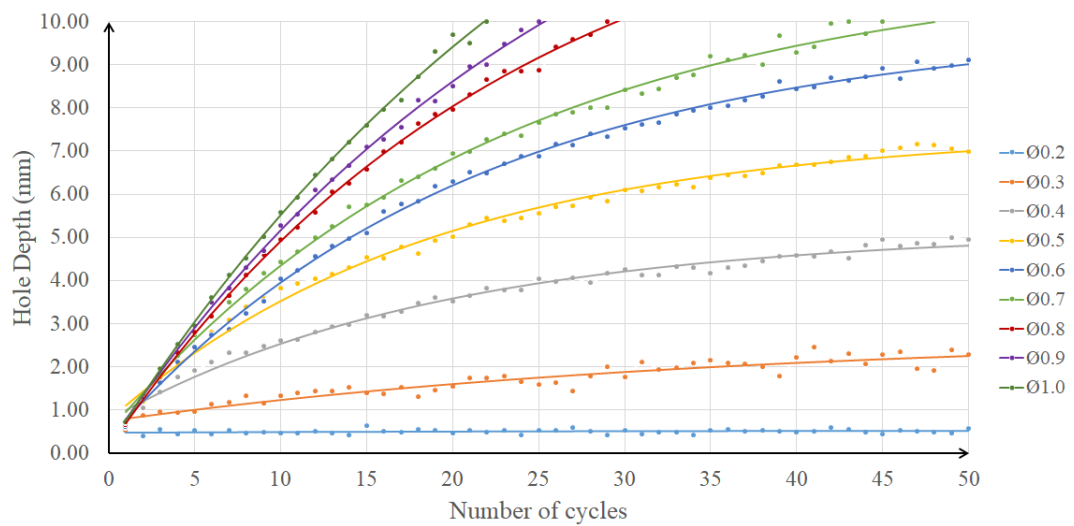


Figure 8.5. Hole depth vs. number of cycles for different hole diameter values

Second observation is that it is more difficult to drill smaller holes. As the number of passes are increased, a depth limit is reached and it is not possible to remove any

more material. The limit depth-to-diameter ratio (DDR) values for the holes can be described as follows:

- $\varnothing = 0.2$ (mm) $\text{DDR} \approx 3$
- $\varnothing = 0.3$ (mm) $\text{DDR} \approx 10$
- $\varnothing \geq 0.4$ (mm) $\text{DDR} \geq 15$

The values are valid for a 50 (μm) nozzle. Smaller nozzles would show a better performance for smaller holes.

8.3.2 Drilling Efficiency

Machining efficiency is thoroughly investigated in Chapter 6. The drilling efficiency for a hole is dependent on the machining parameters as well as the hole geometry. Since the material removal decreases with the hole depth, an equation can be fitted for the saturation behaviour and an efficiency coefficient can be described depending on the hole geometry accordingly. A couple of nonlinear concave curve fit models are applied using Minitab in order to compare and determine the best option. The best results based on the standard deviation of the distance between the data values and the fitted values are obtained for the curve fit equation presented by Adelmann et al. [73], which describes the behaviour for hole drilling as well. Thus, Equation (8.1) can be used to predict the hole depth depending on the number of cycles.

$$d = a - e^{-b(n-c)} \quad (8.1)$$

where d is the drilling depth, a is the maximum hole depth for infinite number of cycles, n is the number of cycles, and b and c are the fitting parameters, which determine the slope and position of the fitted curve. The coefficients obtained for different hole diameters are given in Table 8.3. Figure 8.5 shows the fitted curves for each diameter value.

Table 8.3 Coefficients of Equation (8.1) for different hole diameter values

	a	b	c
Ø0.2	0.5152	0.03980	-85.4155
Ø0.3	2.7582	0.02791	24.9087
Ø0.4	5.1387	0.05165	28.5044
Ø0.5	7.4678	0.05324	35.7514
Ø0.6	9.8929	0.04758	47.4390
Ø0.7	11.2834	0.04432	53.6827
Ø0.8	13.8832	0.04282	61.2289
Ø0.9	16.4450	0.03649	76.4043
Ø1.0	19.6259	0.03231	91.9264

As the hole gets deeper, drilling efficiency decreases. There are many reasons behind this result, as discussed in Chapter 4.2.12. As it can be seen from the discussions, due to the water jet used in WJGL, there are many factors that negatively affect the material removal efficiency. A balance between the processing speed and quality can be established by choosing the processing parameters properly and in accordance with the material to be processed.

There is another important point that should be discussed. Water jet parameters, namely water pressure and gas flow, may also be significant in terms of efficiency for the deep holes. They both affect the evacuation of water from the cavity. However, both parameters should be adjusted based on other necessities. The laser break-up length is highly affected by the water pressure and gas flow, and the length should be checked to see that it is sufficient for drilling before starting the process. For example, in order to drill deeper, it would be better to select a high gas flow rate for better water evacuation, but high levels of gas flow shortens the laser break-up length due to disturbance, which makes it more difficult to drill deep holes. Similarly, high water pressure would be better for penetrating deeper, but it would also mean a stronger splash back. Lower pressure decreases the laser break-up length and makes it more difficult to evacuate water from the cavity as well. Thus, optimum levels should be adjusted taking into consideration the laser break-up length.

8.3.3 Hole Morphology

Quality of the drilled hole is an important issue. WJGL technology provides minimum recast layer and heat-affected zone because of the water cooling and cleaning effects. However, tapering of holes with high DDR is an issue that should be worked on. The exit side of the through holes are generally smaller than the entrance diameter values. Inspection of evolution of the hole morphology might provide some insight on that issue.

First of all, the diameter checks for the holes with a pin gage reveals that the desired diameter values can be obtained very precisely with a spiral toolpath at the hole entrance. The reasons are that the machine axes has high accuracy and the laser beam has a *top-hat* profile. Thus, the toolpath yields high edge quality at the processing zone. Similarly, perfect roundness for the holes can be obtained as expected. On the other hand, since the machining efficiency is lower due to the reasons discussed in the previous section, less material removal causes a smaller diameter formation at the exit side of the hole. It is also more difficult to remove material from the side-walls, when the angle of incidence gets higher [1]. Thus, additional cycles are necessary to increase the exit hole diameter.

The change of the hole morphology during drilling for different hole diameters from the 1st to the 50th cycles can be seen in Figure 8.6. Breakthrough occurred for the holes with Ø0.7, Ø0.8, Ø0.9, and Ø1.0 (mm). It can be seen that the hole bottom diameter is always smaller independent of the depth, but it conforms to the desired diameter as the number of cycles are increased. Thus, the solution to the taper problem seems to be related to the number of cycles that should be applied. However, the time needed to obtain a taper free hole would be too long. For example, hole breakthrough for the Ø1.0 (mm) hole occurred at the 22nd spiral cycle and the taper angle was 1.8° at that point. The taper angle is calculated as 0.5° after the 50th cycle at the end of the experiment, which is still visually large as can be seen in Figure 8.6. Thus, another recipe and/or strategy is needed after the breakthrough to overcome this issue.

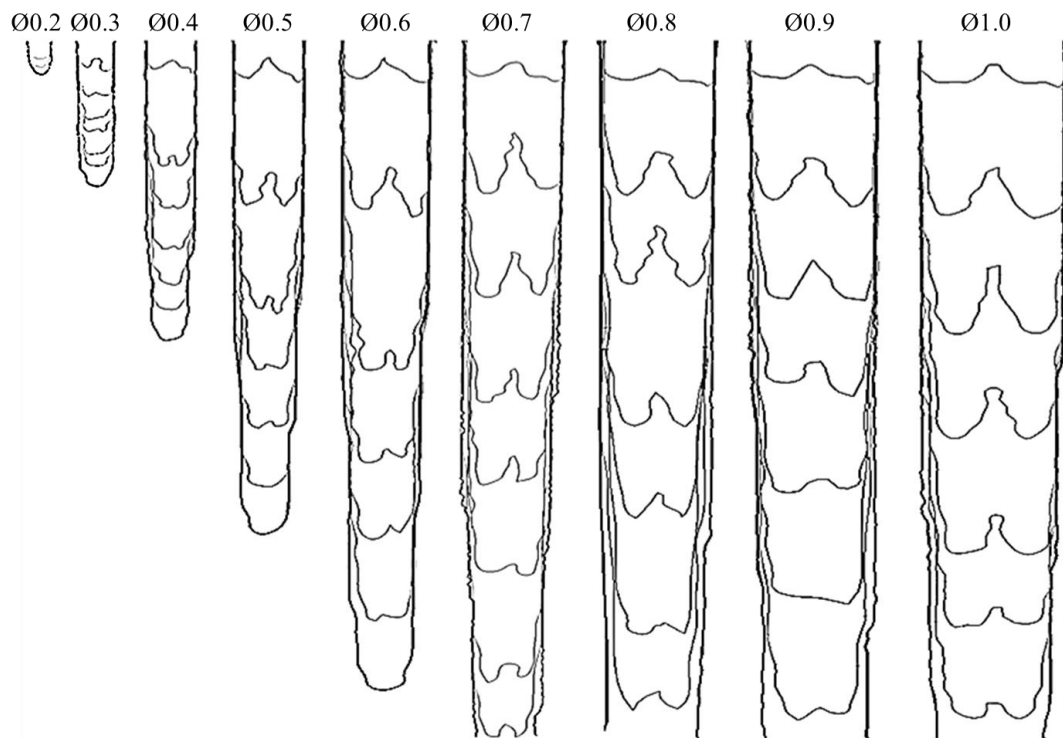


Figure 8.6. Change of hole morphology during drilling

One strategy is to apply a finishing operation by changing the toolpath so that the spiral does not start from the centre, but rather travel on the edges of the hole. Another design of experiment can also be performed in order to decide on the finishing recipe. Increasing the pulse overlap by decreasing the feed rate and spiral stepover without decreasing the power density has some promising results, but further investigation is needed. Similarly, water pressure can be increased assuming there is not any risk of back-wall damage since water splash back is not an issue after the breakthrough. Thus, hole drilling is better taken as a two-step operation. As the first step, the machining efficiency should be kept higher with the optimum parameters to pierce the hole faster. Following that, as the second step, finishing recipe should be applied to obtain the desired quality.

Another observation looking at the cross-section is that the hole bottom starts with a *W* shape and evolves into a *U* shape as the number of cycles is increased. This transformation is visually more distinct for smaller diameters. The reason for having a hill pattern at the centre for the first few cycles is related to the starting point of the spiral toolpath. The laser on condition is actually not at the center of the hole, but shifted per the half of the spiral stepover value, as can be seen in Figure 8.7. In theory, material removal should be uniform around the first circle, but in reality the water jet being concentrated in a smaller region decreases the ablation efficiency at the centre of the hole. Hence, as the drilling operation progresses, the water jet is deflected from the steep side-walls and redirected to the bottom, carrying also the laser energy trapped inside. The chaotic physical impact occurring inside the hole and at the bottom cause morphology change.

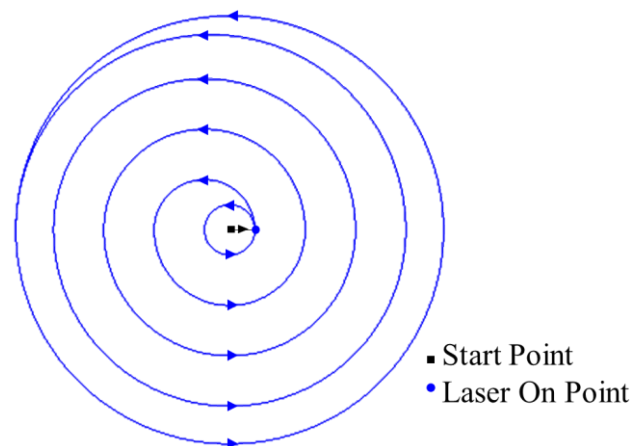


Figure 8.7. Spiral toolpath going outward for Ø0.4 mm and 0.05 mm stepover

8.3.4 Acoustic Analysis

Due to the complex physical mechanisms, it is difficult to make an estimation about the properties of the sound produced by the WJGL process. Many questions can be answered performing acoustic analysis for hole drilling. One of the first things to check is to see how the laser on condition makes difference in sound waves. The

WJGL machine has a unique acoustic signature when the water jet is running. Figure 8.8 shows the PSD plot comparison for laser off and on conditions. Clearly, there is a big difference when the laser is turned on, due to laser-material interaction occurring on the surface. The laser frequency [10 (kHz)] and the harmonics, which are the multiples of the base frequency, are dominant in the plots. The sound difference is more evident in the ultrasound region. However, there is no significant difference beyond 700 (kHz) since the water and air attenuate the acoustic waves for this high frequency range. The sound amplitude of the laser on condition compared to the laser off condition is higher as long as the machining continues. Thus, there is a strong correlation between material removal and acoustic emission. By detecting the minor differences in sound, the methodology can be used for the depth and drilling efficiency predictions.

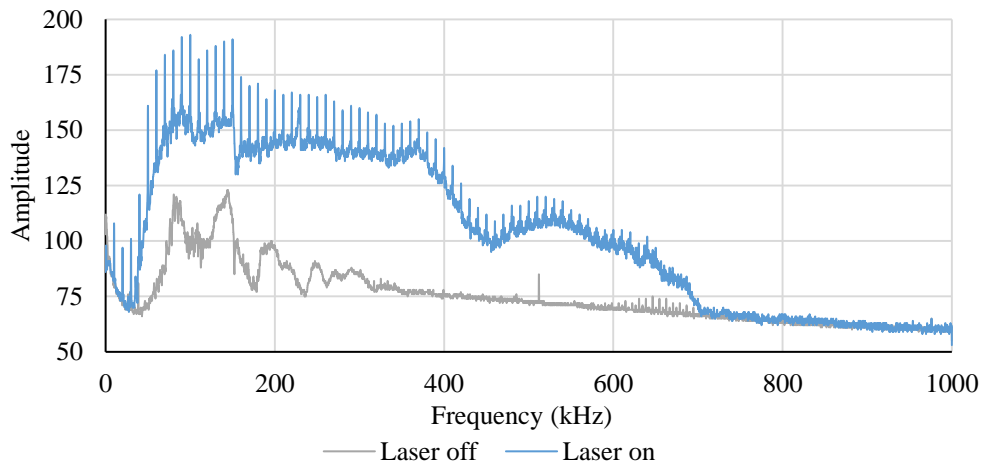


Figure 8.8. PSD plot comparison for laser off and on conditions

Next step is to check whether the sound amplitude and frequencies differ by hole diameter or depth. Figure 8.9 and Figure 8.10 shows the PSD plots for different diameters and depths, respectively. Comparison of the plots indicate that the frequencies produced by the laser-material interaction is the same for every hole size. However, looking at the amplitudes, the difference is significant. Figure 8.9 shows

the sound levels are lower for smaller holes. Similarly, Figure 8.10 shows the sound amplitude decreases as the hole gets deeper. This behaviour is expected, since the emitted sound from a deeper and smaller hole would naturally be muffled compared to a larger and shallower cavity. The water accumulation in the processing zone simply attenuates the acoustic waves even more.

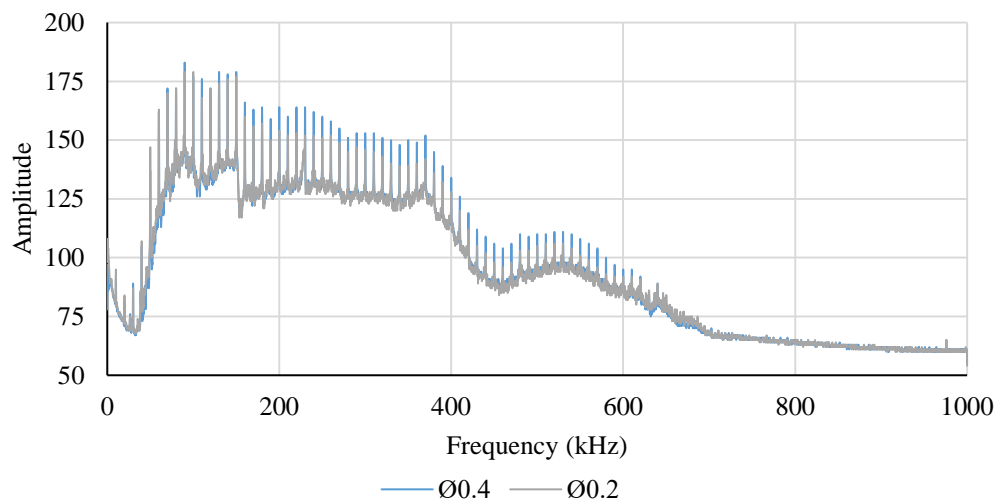


Figure 8.9. PSD comparison between Ø0.2 (mm) and Ø0.4 (mm) holes, 1st cycles

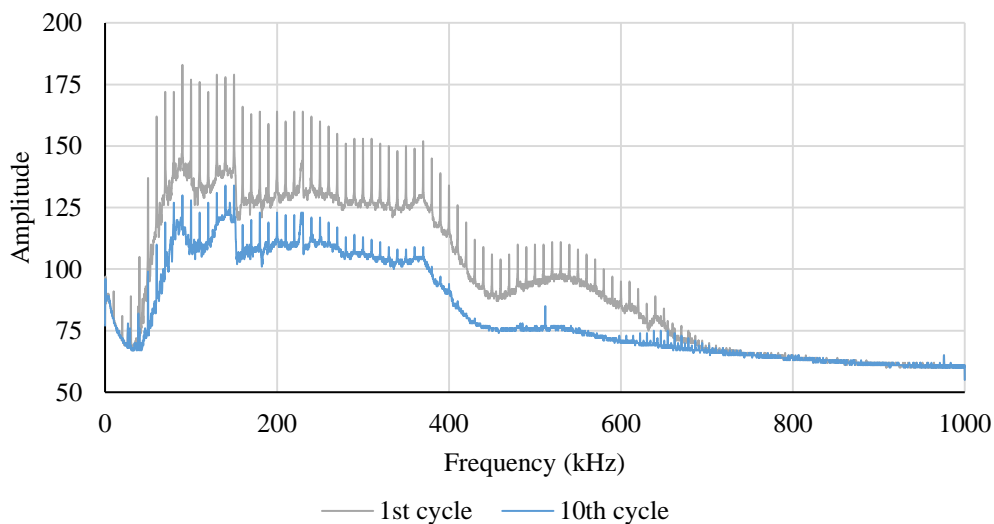


Figure 8.10. PSD comparison between the 1st and the 10th cycles for Ø0.4 (mm) hole

Since the sound frequency levels are independent of hole diameter and depth, only the amplitudes can be compared for different cases. First, the sound change depending on the hole depth can be examined. Since there is a 1 (s) delay between the pulses, as adjusted during the experiments, a window can slide along the energy curve to calculate the average amplitude in one spiral cycle. The methodology can be visually seen in Figure 8.11. Thus, for each diameter and cycle, it is possible to detect the average sound amplitude. Figure 8.12 shows the calculated results in a plot.

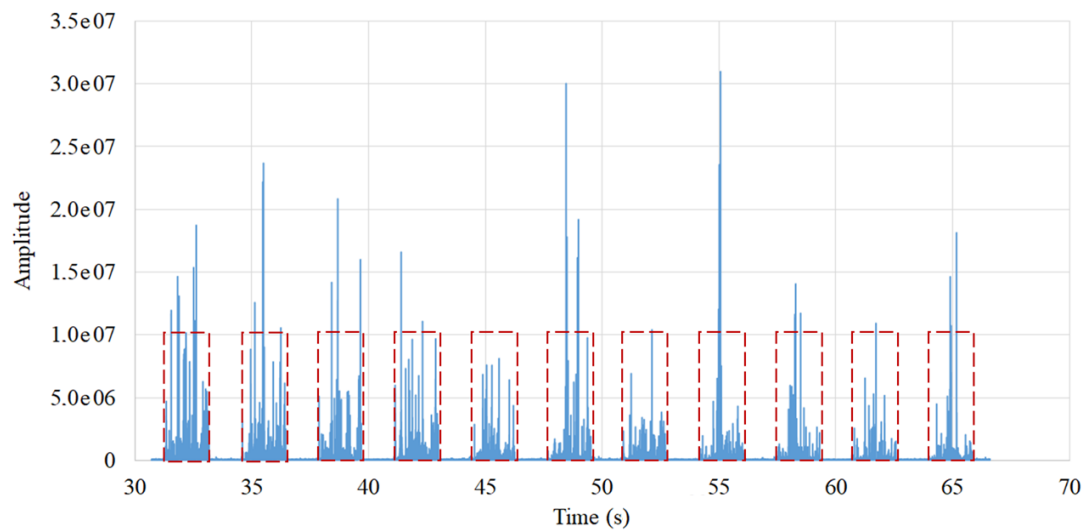


Figure 8.11. Calculating the average sound amplitude for each cycle from the energy curve with a sliding window. Example plot is for Ø0.4 (mm), from 10th to 20th cycle

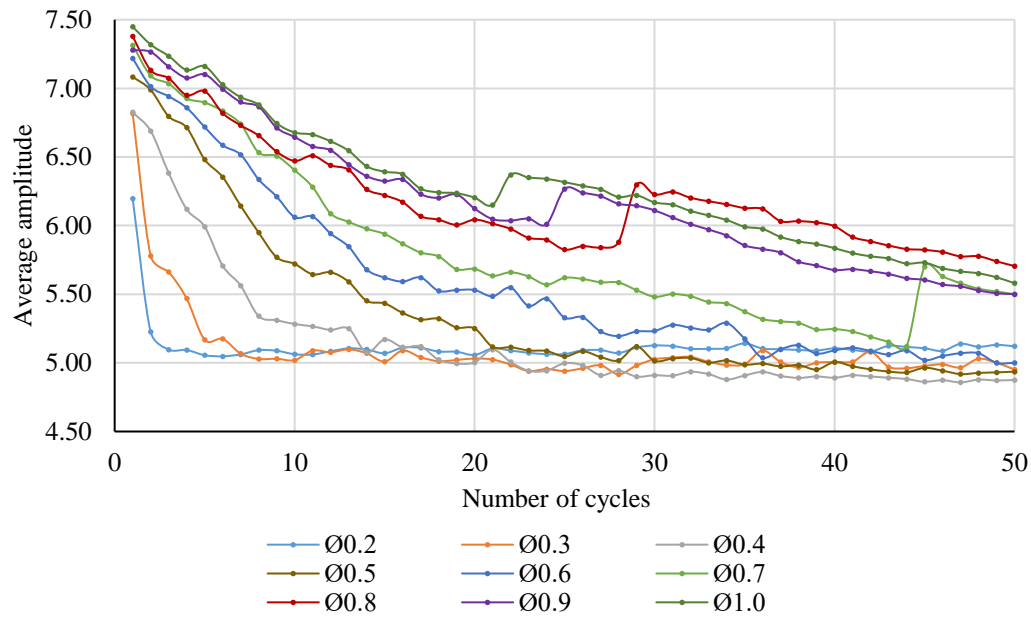


Figure 8.12. Average sound amplitudes depending on the hole diameter and the number of cycles. The amplitude values are scaled by log function

Figure 8.12 reveals some important implications about the process. It can be said that the expectations are met regarding sound amplitude difference depending on the hole diameter and the depth. Smaller holes and deeper cavities make less sound. Thus, it is possible to use acoustic sensing method to approximately determine the hole depth by correlating the sound amplitude to the depth. Deviation and scattering in the plot shows the chaotic nature of the process, especially for hole diameter values less than 0.4 (mm). However, the general behaviour is evident. Another observation is that, when the hole is pierced, the sound amplitude suddenly increases. Looking at the plot, the relevant cycles can be spotted easily [Ø0.7 (mm) hole 45th cycle is an example]. Since there is another opening at the bottom of the workpiece, the sound propagating from the machining zone is better captured by the sensor head. Thus, acoustic sensing has a potential to be used for hole breakthrough detection as well. Nevertheless, more experimentation is needed to see the behaviour for hollow components, where the sound waves would be trapped inside the walls after the breakthrough. Another observation is that as the number of cycles is increased

beyond the hole breakthrough point, the sound amplitude continues to decrease. This is because the material removal at the side walls would be lesser for each additional cycle. In addition, the amount of sudden increase in the sound level at the breakthrough is getting lower as the hole diameter is getting larger. This finding can be attributed to the fact that larger holes already have a higher sound amplitude. Thus, the breakthrough has less effects on the sound amplitude.

Finally, an effort to calculate the drilling efficiency is made by inspecting the energy curves. When there is an interruption of laser ablation during the spiral cycle, it can be detected by acoustic analysis. The success of this method is closely related to the selection of the frequency range and threshold values for the efficiency detection algorithm. First of all, the selected frequency should be distinguishable from the process signal due to intensity. However, reverberation issue might occur in the low frequency range [139] and the low frequencies are generally suppressed by the ambient water jet sound, especially for the deep holes. On the other hand, the sound waves are attenuated significantly at higher frequencies for deep holes. Thus, an optimum frequency level should be found. Examining several PSD plots for different hole diameters and depths, the most convenient frequency level to work with seems to be 200 (kHz). Second, the threshold value can be obtained by calculating the average sound amplitude at 200 (kHz), where the laser is off. Following that, the idle time in a cycle can be measured and efficiency can be calculated using the total cycle time. An example cycle inspection using this methodology is explained in Figure 8.13.

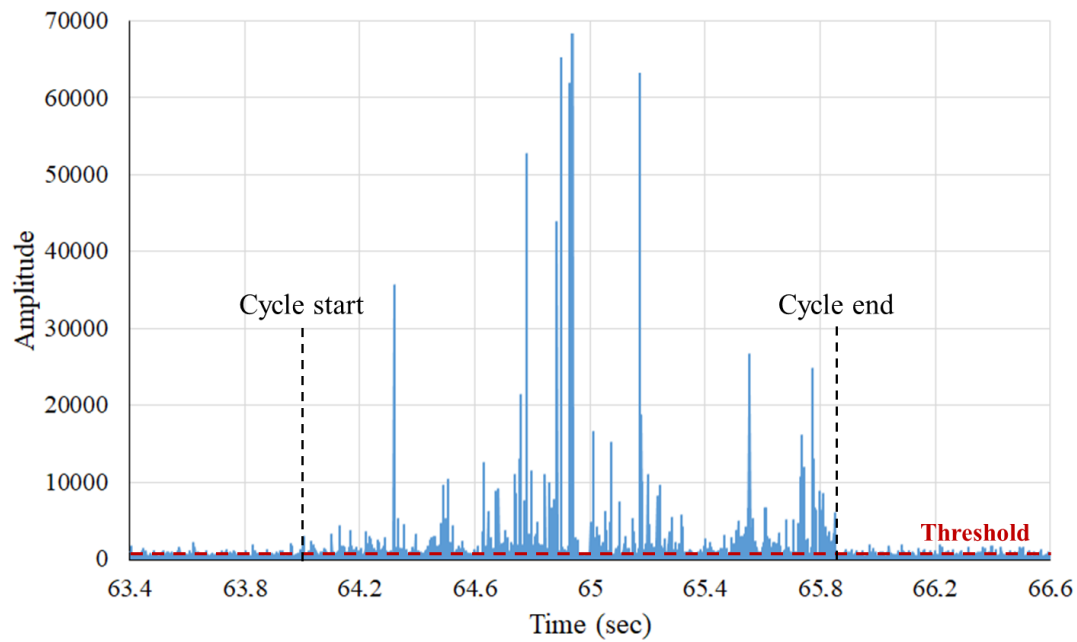


Figure 8.13. Energy curve at 200 (kHz) for Ø0.4 (mm) and 20th spiral cycle, showing the threshold value and cycle start-end

The methodology can be applied to different hole diameters and cycles to determine how the machining efficiency is changing. Table 8.4 shows some calculations for different conditions. For example, for the case of Ø0.4 (mm) and 20th cycle, only 54 laser pulses out of 100 pulses are reaching the surface for the entire spiral cycle. The rest of the energy is lost in the water. It can be concluded that there is a correlation between material removal efficiency and hole size. The efficiency is decreasing with the depth due to water interrupting the laser beam. Thus, the inefficiency should be taken into consideration while machining deeper holes for a proper material removal model of WJGL.

Table 8.4 Calculated efficiency values based on the acoustic analysis for several hole diameters and number of cycles

Diameter (mm)	Cycle #	Cycle time (s)	Idle time (s)	Efficiency (%)
Ø0.4	1	1.882	0.0275	98.5%
	10		0.5235	72.2%
	20		0.8660	54.0%
Ø0.6	1	4.101	0.0465	98.9%
	10		0.3630	91.2%
	20		0.9550	76.7%
Ø0.8	1	7.147	0.0530	99.3%
	10		0.5915	91.7%
	20		0.8445	88.2%

8.4 Closure

A full factorial experiment is conducted by changing the hole diameters and number of spiral cycles to observe how the hole depth, drilling efficiency, hole morphology, and acoustic emission waves are changing in a WJGL system. The measured sound data is correlated to the hole depth and machining efficiency as well. The study is conducted using two novel technologies; a water jet guided laser and an optical microphone. Some physical mechanisms of the WJGL technology is presented and the results of the experiments are discussed in light of the theoretical aspects. First time monitoring of the WJGL micro hole drilling process with an optical microphone is performed. The method provides indirect measurement for the hole depth, machining efficiency, and hole breakthrough. Depending on the water jet nozzle diameter used, there is a reduced limit of DDR especially when drilling small diameter holes. Hole morphology inspection reveals the tapering problem, but also shows that it is possible to avoid it by increasing the number of cycles, and therefore the process time. The drilling efficiency is highly dependent on the hole diameter and depth. Efficiency decreases with increasing the depth and decreasing the diameter. The results are verified by both dimensional measurement and acoustic analysis. The effect of water interruption cannot be neglected and the inefficiency should be taken into consideration when machining deep holes for a proper material removal model of WJGL.

CHAPTER 9

CONCLUSIONS AND FUTURE WORK

9.1 Conclusions

Experimental, optimization, and modeling studies have been conducted to predict the material removal rate for WJGL micro hole drilling. The significant process parameters and their relation to material removal rate and quality are revealed. The physical aspects of material removal mechanisms for LBM and WJGL processing have been investigated. The causes of inefficient machining are discussed in light of the theoretical aspects. Laser ablation mechanism, machine process window, processing limits (minimum diameter & maximum depth capability), and related parameters have been studied for the WJGL. Real-time measurement and monitoring of the process both by image processing and acoustic signal processing have been performed. A better understanding of the process is achieved in the end.

The main outcomes of this study/work are as follows.

1. The efficiency of drilling highly depends on the selected laser parameters, motion parameters, and aspect ratio of the holes, but is not really dependent on material properties within the same family of alloys. Larger stepover and feed rate values increases the drilling process efficiency, whereas larger values of laser power, pulse width, frequency and stand-off distance decreases the efficiency.
2. Material removal with vaporization assumption for WJGL drilling is shown to be a valid approach for predicting the process time. Faster process time can be obtained by using the laser parameters that yields to higher laser power density.

3. Regression modeling provides valuable insight, but lacks the accuracy needed for the material removal model. The mean error values of the regression models for the laser power, the pulse width, and the effective cutting length are ± 2.0 (W), ± 37 (ns), and ± 6.5 (mm), respectively. ANN modeling provides superior results, when compared with the regression model. The mean error values of the ANN models for the laser power, the pulse width, and the effective cutting length are ± 0.3 (W), ± 4 (ns), and ± 1.7 (mm), respectively.
4. Curve fitting model provides a good approximation for the laser power in the water jet, with an average R^2 value of 89.42%.
5. The holistic and simplified material removal model for the WJGL micro hole drilling process is able to estimate the unknown outputs, such as total process time, hole depth at an instance, or number of cycles needed to drill a hole. The proposed model can be used to determine the machine inputs for the first time drilling of a new nickel-based aerospace material and geometry. It can also be used for process optimization, in terms of process time and/or quality.
6. The image processing method based on usage of the camera is successful in terms of detecting the effective cutting length. Image processing is insensitive to water jet parameters.
7. The acoustic emission analysis method based on the optical microphone is performing better for detecting the laser power level in water, since acoustic emission analysis is insensitive to laser parameters, except the laser power. R^2 value for all the data points is 90.18% on average.
8. The acoustic emission analysis method provides estimation of the hole depth, machining efficiency and hole breakthrough.
9. The drilling efficiency is highly dependent on the hole diameter and depth. Efficiency decreases with increasing the depth and decreasing the diameter of the hole. The effect of water interruption cannot be neglected and the inefficiency should be taken into consideration when machining deep holes for a proper material removal model of WJGL.

9.2 Main Contributions of the Study

The following main contributions have been delivered within the scope of the PhD study:

1. A methodology has been proposed for simplified and holistic modeling of the WJGL process.
2. It has been presented how the input parameters should be determined for efficient and higher quality micro drilling of Inconel 625, Inconel 718, and CMSX-4.
3. It has been shown how image processing with a camera can be used to determine the effective cutting length and the laser power in the water jet.
4. It has been shown how acoustic monitoring with an optical microphone can be used to determine laser power in the water jet, hole depth, machining efficiency, and breakthrough.

9.3 Future Work

The thesis would create many opportunities for future work. The modeling study can be further extended to cover other materials. The model can be improved to represent the geometrical conditions better. For example, the effect of different hole angles can be investigated. Different tool paths resulting in different geometries (such as ellipse, countersink, pockets, grooves or surface texturing) may be studied. High-speed camera monitoring can be performed to investigate water jet dynamics and laser-water interaction to develop analytical models for effective cutting length and power variation in the water jet. The physical mechanisms of the inefficiencies related to WJGL micromachining can be studied in more detail so that the model can be developed to give more accurate results. The difference between the material removed per laser pulse for the analytical approach and experiments can be explained by investigating the resolidified substrate material layer on the drilled holes. Other quality aspects of the process, such as the surface quality of the side-walls of the

drilled holes can be examined in more detail. Numerical modeling can be applied for deep holes considering the inefficiency caused by the water in the process. The proposed model can be embedded into a software package so that a digital model or a digital twin of the WJGL machine can be obtained. It is possible to implement intelligent acoustic analysis software into the machine interface so that the acoustic signals would provide feedback to the operator about the machining conditions. Another feedback system can be introduced on the machine, in which the operator inputs the desired length and/or power value in the interface. Machine parameters may change automatically to meet the desired output by using real-time measurement by image/acoustic analysis and active feedback control.

REFERENCES

- [1] Porter JA, Louhisalmi YA, Karjalainen JA, Füger S. Cutting thin sheet metal with a water jet guided laser using various cutting distances, feed speeds and angles of incidence. *The International Journal of Advanced Manufacturing Technology*. 2007 Jul;33(9):961-7.
- [2] Cabalin LM, Laserna JJ. Experimental determination of laser induced breakdown thresholds of metals under nanosecond Q-switched laser operation. *Spectrochimica Acta Part B: Atomic Spectroscopy*. 1998 May 29;53(5):723-30.
- [3] Yeo CY, Tam SC, Jana S, Lau MW. A technical review of the laser drilling of aerospace materials. *Journal of materials processing technology*. 1994 Apr 1;42(1):15-49.
- [4] Spiegel A, Vago N, Wagner FR. High efficiency Raman scattering in micrometer-sized water jets. *Optical Engineering*. 2004 Feb;43(2):450-4.
- [5] Jacobs P. Precision trepanning with a fiber laser. In *International Congress on Applications of Lasers & Electro-Optics 2008 Oct* (Vol. 2008, No. 1, p. 303). Laser Institute of America.
- [6] Wang M, Yang L, Zhang S, Wang Y. Experimental investigation on the spiral trepanning of K24 superalloy with femtosecond laser. *Optics & Laser Technology*. 2018 May 1;101:284-90.
- [7] Hashmi S. *Comprehensive materials processing*. Newnes; 2014 Apr 7.
- [8] Yilbas BS. A study of affecting parameters in the laser hole-drilling of sheet metals. *Journal of mechanical working technology*. 1986 Oct 1;13(3):303-15.
- [9] Forget P, Jeandin M, Lechervy P, Varela D. Laser drilling of a superalloy coated with ceramic. *Superalloys 1988*. 1988:553-62.
- [10] Yilbaş BS, Şahin AZ, Davies R. Laser heating mechanism including evaporation process initiating laser drilling. *International Journal of Machine Tools and Manufacture*. 1995 Jul 1;35(7):1047-62.
- [11] Yilbas BS, Yilbas Z, Akcakoyun N. Investigation into absorption of the incident laser beam during Nd: YAG laser processing of metals. *Optics & Laser Technology*. 1996 Oct 1;28(7):503-11.
- [12] Yilbas BS, Akhtar SS, Karatas C. Laser trepanning of a small diameter hole in titanium alloy: temperature and stress fields. *Journal of Materials Processing Technology*. 2011 Jul 1;211(7):1296-304.
- [13] Sibalija TV, Petronic SZ, Majstorovic VD, Prokic-Cvetkovic R, Milosavljevic A. Multi-response design of Nd: YAG laser drilling of Ni-based superalloy sheets using Taguchi's quality loss function, multivariate statistical methods and artificial intelligence. *The International Journal of Advanced Manufacturing Technology*. 2011 May;54(5):537-52.
- [14] Yilbas BS. Parametric study to improve laser hole drilling process. *Journal of Materials Processing Technology*. 1997 Oct 1;70(1-3):264-73.

- [15] Mishra S, Yadava V. Modeling and optimization of laser beam percussion drilling of nickel-based superalloy sheet using Nd: YAG laser. *Optics and Lasers in Engineering*. 2013 Jun 1;51(6):681-95.
- [16] Ganesh RK, Bowley WW, Bellantone RR, Hahn Y. A model for laser hole drilling in metals. *Journal of Computational Physics*. 1996 Apr 1;125(1):161-76.
- [17] Horn A, Weichenhain R, Albrecht S, Kreutz EW, Michel J, Niessen M, Kostykin V, Schulz W, Etzkorn A, Bobzin K, Lugscheider E. Microholes in zirconia-coated Ni-superalloys for transpiration cooling of turbine blades. In *High-Power Laser Ablation III* 2000 Aug 16 (Vol. 4065, pp. 218-226). SPIE.
- [18] Sezer HK, Li L, Schmidt M, Pinkerton AJ, Anderson B, Williams P. Effect of beam angle on HAZ, recast and oxide layer characteristics in laser drilling of TBC nickel superalloys. *International Journal of Machine Tools and Manufacture*. 2006 Dec 1;46(15):1972-82.
- [19] Arrizubieta I, Lamikiz A, Martínez S, Ukar E, Tabernero I, Girot F. Internal characterization and hole formation mechanism in the laser percussion drilling process. *International Journal of Machine Tools and Manufacture*. 2013 Dec 1;75:55-62.
- [20] Wang R, Duan W, Wang K, Dong X, Fan Z, Mei X, Wang W, Zhang S. Computational and experimental study on hole evolution and delamination in laser drilling of thermal barrier coated nickel superalloy. *Optics and Lasers in Engineering*. 2018 Aug 1;107:161-75.
- [21] Afrasiabi M, Chatzi E, Wegener K. A particle strength exchange method for metal removal in laser drilling. *Procedia CIRP*. 2018 Jan 1;72:1548-53.
- [22] Tam SC, Yeo CY, Jana S, Lau MW, Lim LE, Yang LJ, Noor YM. Optimization of laser deep-hole drilling of Inconel 718 using the Taguchi method. *Journal of Materials Processing Technology*. 1993 Feb 1;37(1-4):741-57.
- [23] Chen X, Lotshaw WT, Ortiz AL, Staver PR, Erikson CE, McLaughlin MH, Rockstroh TJ. Laser drilling of advanced materials: effects of peak power, pulse format, and wavelength. *Journal of laser applications*. 1996 Oct;8(5):233-9.
- [24] Wu Q, Ma Y, Jie J, Miao B, Fang R, Chen X. Hole drilling of INCONEL 718 by high intensity pulsed UV laser. In *International Congress on Applications of Lasers & Electro-Optics* 2001 Oct (Vol. 2001, No. 1, pp. 248-256). Laser Institute of America.
- [25] Wu Q, Ma Y, Jie J, Yu Q, Liao Y, Fang R, Chen X, Wang K. Hole drilling of Inconel 718 by high intensity pulsed ultraviolet laser. *Journal of Laser Applications*. 2003 Aug;15(3):168-71.
- [26] Corcoran A, Sexton L, Seaman B, Ryan P, Byrne G. The laser drilling of multi-layer aerospace material systems. *Journal of materials processing technology*. 2002 Apr 10;123(1):100-6.

- [27] Bandyopadhyay S, Sundar JS, Sundararajan G, Joshi SV. Geometrical features and metallurgical characteristics of Nd: YAG laser drilled holes in thick IN718 and Ti-6Al-4V sheets. *Journal of Materials Processing Technology*. 2002 Sep 20;127(1):83-95.
- [28] Bandyopadhyay S, Gokhale H, Sundar JS, Sundararajan G, Joshi SV. A statistical approach to determine process parameter impact in Nd: YAG laser drilling of IN718 and Ti-6Al-4V sheets. *Optics and Lasers in Engineering*. 2005 Feb 1;43(2):163-82.
- [29] Ghoreishi M, Low DK, Li L. Comparative statistical analysis of hole taper and circularity in laser percussion drilling. *International Journal of Machine Tools and Manufacture*. 2002 Jul 1;42(9):985-95.
- [30] Ghoreishi M, Nakhjavani OB. Optimisation of effective factors in geometrical specifications of laser percussion drilled holes. *Journal of materials processing Technology*. 2008 Jan 21;196(1-3):303-10.
- [31] Leigh S, Sezer K, Li L, Grafton-Reed C, Cuttall M. Recast and oxide formation in laser-drilled acute holes in CMSX-4 nickel single-crystal superalloy. *Proceedings of the Institution of Mechanical Engineers, Part B: Journal of Engineering Manufacture*. 2010 Jul 1;224(7):1005-16.
- [32] Biswas R, Kuar AS, Sarkar S, Mitra S. A parametric study of pulsed Nd: YAG laser micro-drilling of gamma-titanium aluminide. *Optics & Laser Technology*. 2010 Feb 1;42(1):23-31.
- [33] Biswas R, Kuar AS, Mitra S. Multi-objective optimization of hole characteristics during pulsed Nd: YAG laser microdrilling of gamma-titanium aluminide alloy sheet. *Optics and Lasers in Engineering*. 2014 Sep 1;60:1-1.
- [34] Chatterjee S, Mahapatra SS, Sahu AK, Bhardwaj VK, Choubey A, Upadhyay BN, Bindra KS. Experimental investigation of quality characteristics in Nd: YAG laser drilling of stainless steel (AISI 316). *Materials Today: Proceedings*. 2018 Jan 1;5(5):11526-30.
- [35] VanderWert TL, Litzer SA, Meng LW. Laser Drilling Effusion Cooling Holes in Low NOx Turbine Engine Components. In *Turbo Expo: Power for Land, Sea, and Air 1996* Nov 5 (Vol. 78774, p. V001T07A005). American Society of Mechanical Engineers.
- [36] Das DK, Pollock TM. Femtosecond laser machining of cooling holes in thermal barrier coated CMSX4 superalloy. *Journal of Materials Processing Technology*. 2009 Aug 1;209(15-16):5661-8.
- [37] Antar M, Chantzis D, Marimuthu S, Hayward P. High speed EDM and laser drilling of aerospace alloys. *Procedia Cirp*. 2016 Jan 1;42:526-31.
- [38] Fan Z, Dong X, Wang K, Duan W, Wang R, Mei X, Wang W, Cui J, Yuan X, Xu C. Effect of drilling allowance on TBC delamination, spatter and re-melted cracks characteristics in laser drilling of TBC coated superalloys. *International Journal of Machine Tools and Manufacture*. 2016 Jul 1;106:1-0.
- [39] Morar N, Roy R, Mehnen J, Nicholls JR, Gray S. The effect of trepanning speed of laser drilled acute angled cooling holes on the high temperature

- low cycle corrosion fatigue performance of CMSX-4 at 850 C. *International Journal of Fatigue*. 2017 Sep 1;102:112-20.
- [40] Marimuthu S, Antar M, Dunleavy J, Chantzis D, Darlington W, Hayward P. An experimental study on quasi-CW fibre laser drilling of nickel superalloy. *Optics & Laser Technology*. 2017 Sep 1;94:119-27.
 - [41] Parthiban K, Duraiselvam M, Manivannan R. TOPSIS based parametric optimization of laser micro-drilling of TBC coated nickel based superalloy. *Optics & Laser Technology*. 2018 Jun 1;102:32-9.
 - [42] Uchtmann H, Kürschner D, Kelbassa I. Hybrid laser drilling of cooling holes by using millisecond pulsed fiber laser radiation and ultrashort pulsed laser radiation. In *International Congress on Applications of Lasers & Electro-Optics 2015 Oct (Vol. 2015, No. 1, pp. 955-962)*. Laser Institute of America.
 - [43] Gruner A, Schille J, Loeschner U. Experimental study on micro hole drilling using ultrashort pulse laser radiation. *Physics Procedia*. 2016 Jan 1;83:157-66.
 - [44] Dubey AK, Yadava V. Experimental study of Nd: YAG laser beam machining—An overview. *Journal of materials processing technology*. 2008 Jan 1;195(1-3):15-26.
 - [45] Low DK, Li L, Byrd PJ. The effects of process parameters on spatter deposition in laser percussion drilling. *Optics & Laser Technology*. 2000 Jul 1;32(5):347-54.
 - [46] Low DK, Li L, Corfe AG. Effects of assist gas on the physical characteristics of spatter during laser percussion drilling of NIMONIC 263 alloy. *Applied surface science*. 2000 Feb 1;154:689-95.
 - [47] Low DK, Li L, Corfe AG. Characteristics of spatter formation under the effects of different laser parameters during laser drilling. *Journal of materials processing Technology*. 2001 Dec 3;118(1-3):179-86.
 - [48] Low DK, Li L, Corfe AG, Byrd PJ. Spatter-free laser percussion drilling of closely spaced array holes. *International Journal of Machine Tools and Manufacture*. 2001 Feb 1;41(3):361-77.
 - [49] Low DK, Li L, Byrd PJ. Spatter prevention during the laser drilling of selected aerospace materials. *Journal of materials processing technology*. 2003 Aug 20;139(1-3):71-6.
 - [50] Stroud D, Corfe AG, inventors; Rolls Royce PLC, assignee. Laser barrier material. United States patent US 5,140,127. 1992 Aug 18.
 - [51] Gregory O, Griffith AJ, Stroud D, inventors; Rolls Royce PLC, assignee. Drilling turbine blades. United States patent US 5,222,617. 1993 Jun 29.
 - [52] Moore JR, Wheat GE, inventors; General Electric Co, assignee. Beam blocking material and method for beam drilling and inspecting cooling holes. United States patent US 5,773,790. 1998 Jun 30.
 - [53] Flis JD, Jones JD, Waller Jr JF, inventors; United Technologies Corp, assignee. Method of laser drilling an airfoil. United States patent US 5,914,060. 1999 Jun 22.

- [54] Sheng P, Chryssolouris G. Investigation of acoustic sensing for laser machining processes Part 1: Laser drilling. *Journal of materials processing technology*. 1994 Jun 1;43(2-4):125-44.
- [55] Tunna L, Kearns A, O'Neill W, Sutcliffe CJ. Micromachining of copper using Nd: YAG laser radiation at 1064, 532, and 355 nm wavelengths. *Optics & Laser Technology*. 2001 Apr 1;33(3):135-43.
- [56] Sanikommu N, Bathe R, Joshi AS. Detection of Breakthrough in Laser Percussion Drilling. *Lasers in Engineering* (Old City Publishing). 2007 Oct 1;17.
- [57] Moslehpour S, Kondo J, Alnajjar H. Analog Breakthrough Detection using laser-Induced, Thermal Diffusion Shock Waves.
- [58] Ho CC, Hsu JC, Chang YJ, Kuo CL, He JJ. Real-time Breakthrough Detection for Laser Drilling Based on Coaxial Visual Sensing Technology. In *Applied Mechanics and Materials 2013* (Vol. 284, pp. 2281-2285). Trans Tech Publications Ltd.
- [59] Ho CC, Chang YJ, Hsu JC, Kuo CL, He JJ. Monitoring and Breakthrough Control of Laser Drilled Holes by Means of Machine Vision. *Transactions of the Canadian Society for Mechanical Engineering*. 2013;37(3):355-63.
- [60] Taylor GW. Liquid optical fibers. *Applied Optics*. 1972 Apr 1;11(4):786-90.
- [61] Richerzhagen B, inventor; Synova SA, assignee. Method and apparatus for machining material with a liquid-guided laser beam. United States patent US 5,902,499. 1999 May 11.
- [62] Dushkina NM, Wagner FR, Boillat C, Buchilly JM, Richerzhagen B. Water jet guided laser versus saw dicing. In *Photon Processing in Microelectronics and Photonics II 2003 Oct 17* (Vol. 4977, pp. 75-85). SPIE.
- [63] Madhukar YK, Mullick S, Nath AK. A study on co-axial water-jet assisted fiber laser grooving of silicon. *Journal of Materials Processing Technology*. 2016 Jan 1;227:200-15.
- [64] Bruckert F, Pilat E, Piron P, Torres P, Carron B, Richerzhagen B, Pirot M, Monna R. Tailor cutting of crystalline solar cells by laser micro jet. In *High Power Laser Materials Processing: Lasers, Beam Delivery, Diagnostics, and Applications 2012 Feb 6* (Vol. 8239, pp. 191-197). SPIE.
- [65] Hock K, Adelmann B, Hellmann R. Comparative study of remote fiber laser and water-jet guided laser cutting of thin metal sheets. *Physics Procedia*. 2012 Jan 1;39:225-31.
- [66] Richmann A, Kurzen S, Carron B, Richerzhagen B. Cutting diamond tools using the Laser MicroJet® technology on a 5-axis machine. In *Proceedings of Lasers in Manufacturing Conference 2015, Munich, Germany, June 22–25 2015 Jun*.
- [67] Sun D, Han F, Ying W, Jin C. Surface integrity of water jet guided laser machining of CFRP. *Procedia CIRP*. 2018 Jan 1;71:71-4.
- [68] Diboine J, Martin R, Bruckert F, Diehl H, Richerzhagen B. Towards near-net shape micro-machining of aerospace materials by means of a water

- jet-guided laser beam. In Lasers in Manufacturing Conference, Munich, Germany, June 26–29 2017 Jun.
- [69] Rashed CA, Romoli L, Tantussi F, Fuso F, Burgener M, Cusanelli G, Allegrini M, Dini G. Water jet guided laser as an alternative to EDM for micro-drilling of fuel injector nozzles: A comparison of machined surfaces. *Journal of Manufacturing Processes*. 2013 Oct 1;15(4):524-32.
 - [70] Gurav MM, Gupta U, Dabade UA. Quality evaluation of precision micro holes drilled using pulsed Nd: YAG laser on aerospace nickel-based superalloy. *Materials Today: Proceedings*. 2019 Jan 1;19:575-82.
 - [71] Li CF, Johnson DB, Kovacevic R. Modeling of waterjet guided laser grooving of silicon. *International Journal of Machine Tools and Manufacture*. 2003 Jul 1;43(9):925-36.
 - [72] Yang LJ, Wang ML, Wang Y, Tang J, Chen YB. Numerical and experimental research on water-jet guided laser micromachining. In *Materials Science Forum 2009* (Vol. 626, pp. 297-302). Trans Tech Publications Ltd.
 - [73] Adelmann B, Ngo C, Hellmann R. High aspect ratio cutting of metals using water jet guided laser. *The International Journal of Advanced Manufacturing Technology*. 2015 Oct;80(9):2053-60.
 - [74] Kruusing A. Underwater and water-assisted laser processing: Part 1—general features, steam cleaning and shock processing. *Optics and lasers in engineering*. 2004 Feb 1;41(2):307-27.
 - [75] Kruusing A. Underwater and water-assisted laser processing: Part 2—Etching, cutting and rarely used methods. *Optics and Lasers in Engineering*. 2004 Feb 1;41(2):329-52.
 - [76] Tsai CH, Li CC. Investigation of underwater laser drilling for brittle substrates. *Journal of materials processing technology*. 2009 Mar 19;209(6):2838-46.
 - [77] Iwatani N, Doan HD, Fushinobu K. Optimization of near-infrared laser drilling of silicon carbide under water. *International Journal of Heat and Mass Transfer*. 2014 Apr 1;71:515-20.
 - [78] Chen Q, Wang HJ, Lin DT, Zuo F, Zhao ZX, Lin HT. Characterization of hole taper in laser drilling of silicon nitride ceramic under water. *Ceramics International*. 2018 Aug 1;44(11):13449-52.
 - [79] Liu Z, Gao Y, Wu B, Shen N, Ding H. Ultrasound-assisted water-confined laser micromachining: A novel machining process. *Manufacturing Letters*. 2014 Oct 1;2(4):87-90.
 - [80] Liu Z, Wu B, Samanta A, Shen N, Ding H, Xu R, Zhao K. Ultrasound-assisted water-confined laser micromachining (UWLM) of metals: Experimental study and time-resolved observation. *Journal of Materials Processing Technology*. 2017 Jul 1;245:259-69.
 - [81] Wang H, Zhu S, Xu G, Zhou W, Li L, Zhang DH, Ren N, Xia K, Shi C. Influence of ultrasonic vibration on percussion drilling performance for millisecond pulsed Nd: YAG laser. *Optics & Laser Technology*. 2018 Aug 1;104:133-9.

- [82] Shi C, Ren N, Wang H, Xia K, Wang L. Effects of ultrasonic assistance on microhole drilling based on Nd: YAG laser trepanning. *Optics & Laser Technology*. 2018 Oct 1;106:451-60.
- [83] Xia K, Ren N, Wang H, Shi C. Analysis for effects of ultrasonic power on ultrasonic vibration-assisted single-pulse laser drilling. *Optics and Lasers in Engineering*. 2018 Nov 1;110:279-87.
- [84] Wang H, Zhu S, Asundi A, Xu Y. Experimental characterization of laser trepanning performance enhanced by water-based ultrasonic assistance. *Optics & Laser Technology*. 2019 Jan 1;109:547-60.
- [85] Kaakkunen JJ, Silvennoinen M, Paivasaari K, Vahimaa P. Water-assisted femtosecond laser pulse ablation of high aspect ratio holes. *Physics Procedia*. 2011 Jan 1;12:89-93.
- [86] López JM, Bakrania A, Coupland J, Marimuthu S. Droplet assisted laser micromachining of hard ceramics. *Journal of the European Ceramic Society*. 2016 Sep 1;36(11):2689-94.
- [87] Migliore LR. *Laser materials processing*. Marcel Dekker; 1996 Apr 2.
- [88] Ready JF. *LIA-Handbook of Laser Materials Processing*. Magnolia Publishing; 2001 May 1.
- [89] Steen WM, Mazumder J. *Laser material processing*. Springer science & business media; 2010 Nov 30.
- [90] Majumdar JD, Manna I, editors. *Laser-assisted fabrication of materials*. Springer Science & Business Media; 2012 Nov 3.
- [91] Stafe M, Marcu A, Puscas NN. *Pulsed laser ablation of solids: basics, theory and applications*. Springer Science & Business Media; 2013 Nov 9.
- [92] Bass M. *Laser Materials Processing*. Elsevier Science Ltd; 1983 Jan 1.
- [93] Ready JF. *Industrial Applications of Lasers*. Academic Press; 1997 Apr 16.
- [94] Ion J. *Laser processing of engineering materials: principles, procedure and industrial application*. Elsevier; 2005 Mar 22.
- [95] Svelto O. *Principles of Lasers*. Springer; 2010
- [96] Kannatey-Asibu Jr E. *Principles of laser materials processing*. John Wiley & Sons; 2009 Apr 22.
- [97] Bäuerle D. *Laser Processing and Chemistry*. Springer; 2011 Aug 28.
- [98] Gladush GG, Smurov I. *Physics of laser materials processing: theory and experiment*. Springer Science & Business Media; 2011 Aug 5.
- [99] Metev SM, Veiko VP. *Laser-Assisted Microtechnology (Series in Materials Science vol 19)*.
- [100] Darwish SM, Ahmed N, Al-Ahmari AM, editors. *Laser beam micro-milling of micro-channels in aerospace alloys*. Berlin, Germany: Springer; 2017 Jan 31.
- [101] Richerzhagen B, House R, Wagner F, Manley J. *Water jet guided laser cutting: A powerful hybrid technology for fine cutting and grooving*, ALAC. Ann Arbor, Michigan, USA. 2004.

- [102] Mai TA, Richerzhagen B. 53.3: Manufacturing of 4th generation OLED masks with the Laser MicroJet® Technology. InSID Symposium Digest of Technical Papers 2007 May (Vol. 38, No. 1, pp. 1596-1598). Oxford, UK: Blackwell Publishing Ltd.
- [103] Jablonski R, Turkowski M, Szewczyk R, editors. Recent advances in mechatronics. Springer Science & Business Media; 2007 Sep 19.
- [104] Wagner FR, Boillat C, Buchilly JM, Spiegel A, Vago N, Richerzhagen B. High-speed cutting of thin materials with a Q-switched laser in a water-jet versus conventional laser cutting with a free running laser. InPhoton Processing in Microelectronics and Photonics II 2003 Oct 17 (Vol. 4977, pp. 70-74). SPIE.
- [105] Liu Y, Wei M, Zhang T, Qiao H, Li H. Overview on the development and critical issues of water jet guided laser machining technology. Optics & Laser Technology. 2021 May 1;137:106820.
- [106] Nilsson T, Wagner F, Housh R, Richerzhagen B. Scribing of GaN wafer for white LED by water-jet-guided laser. InLight-Emitting Diodes: Research, Manufacturing, and Applications VIII 2004 Jun 21 (Vol. 5366, pp. 200-206). SPIE.
- [107] Pauchard A, Gobet M, Juvet F, Schreiner A. Metal and stent cutting using water jet-guided laser technology. InInternational Congress on Applications of Lasers & Electro-Optics 2010 Sep (Vol. 2010, No. 1, pp. 1139-1145). Laser Institute of America.
- [108] Kruusing A. Handbook of liquids-assisted laser processing. Elsevier; 2010 Jul 7.
- [109] Couty P, Spiegel A, Vágó N, Ugurtas BI, Hoffmann P. Laser-induced break-up of water jet waveguide. Experiments in fluids. 2004 Jun;36(6):919-27.
- [110] Sun D, Han F, Ying W. The experimental investigation of water jet-guided laser cutting of CFRP. The International Journal of Advanced Manufacturing Technology. 2019 May;102(1):719-29.
- [111] Vágó N, Spiegel A, Couty P, Wagner FR, Richerzhagen B. New technique for high-speed microjet breakup analysis. Experiments in fluids. 2003 Oct;35(4):303-9.
- [112] Brecher C, Janssen H, Eckert M, Schmidt F. Thermal investigation of interaction between high-power CW-laser radiation and a water-jet. Physics Procedia. 2016 Jan 1;83:317-27.
- [113] Cadavid R, Wüstenberg D, Louis H, Pude F, Senne T. Effect of helium atmospheres on abrasive suspension water jets. The International Journal of Advanced Manufacturing Technology. 2005 Nov;26(11):1246-54.
- [114] Gaebele J, Hribar J, Avonisys AG. Pushing the envelope of liquid-jet guided laser machining applying modern IR fiber lasers.
- [115] Yang L, Wang M, Wang Y. Research on water-jet guided laser micromachining of 65-Mn steel. International Journal of Abrasive Technology. 2010 Jan 1;3(4):338-53.

- [116] Wang Y, Yang LJ, Tang J, Li L, Chen YB. Laser and water-jet fiber coupling technology for water-jet guided laser micromachining. In *Advanced Materials Research 2009* (Vol. 69, pp. 29-33). Trans Tech Publications Ltd.
- [117] Battaglia J, Mai TA, Perrottet D, Richerzhagen B. Waterjet as a multimode waveguide-theoretical and experimental investigation of modal noise and beam propagation in material processing with lasermicrojet. In *International Congress on Applications of Lasers & Electro-Optics 2006 Oct* (Vol. 2006, No. 1, p. M605). Laser Institute of America.
- [118] Boyd RW. *Nonlinear Optics*. Elsevier; 2008 Mar 28.
- [119] Bai Y. Reducing the Roughness of the Kerf for Brass Sheet Cutting with the Laser MicroJet® by a Systematic Parameter Study. In *Proceedings Lasers in Manufacturing Conference 2015* 2015.
- [120] Wang Z. Investigation of the Water Guided Laser Micro-Jet Machining of Aero Engine Components. In *International Manufacturing Science and Engineering Conference 2017 Jun 4* (Vol. 50725, p. V001T02A044). American Society of Mechanical Engineers.
- [121] Bektas E, Subasi L, Gunaydin A, Diboine J, Can Ozaner O, Canadinc D. Water Jet Guided Laser vs. Conventional Laser: Experimental Comparison of Surface Integrity for Different Aerospace Alloys. *Journal of Laser Micro/Nanoengineering*. 2021 Apr 1;16(1).
- [122] Richerzhagen B, Plankensteiner M, Kling NU, Stay K, Brulé A. Saw+ LMJ: A hybrid semiconductor dicing solution. In *Laser-based Micro-and Nanopackaging and Assembly II 2008 Feb 22* (Vol. 6880, pp. 57-62). SPIE.
- [123] Tabie VM, Koranteng MO, Yunus A, Kuuyine F. Water-jet guided laser cutting technology-an overview. *Lasers in Manufacturing and Materials Processing*. 2019 Jun;6(2):189-203.
- [124] Roy RK. *A primer on the Taguchi method*. Society of Manufacturing Engineers; 2010.
- [125] Casalino G. Computational intelligence for smart laser materials processing. *Optics & Laser Technology*. 2018 Mar 1;100:165-75.
- [126] Sharma A, Yadava V. Experimental analysis of Nd-YAG laser cutting of sheet materials—A review. *Optics & Laser Technology*. 2018 Jan 1;98:264-80.
- [127] Parandoush P, Hossain A. A review of modeling and simulation of laser beam machining. *International journal of machine tools and manufacture*. 2014 Oct 1;85:135-45.
- [128] Mishra S, Yadava V. Laser beam micromachining (LBMM)—a review. *Optics and lasers in engineering*. 2015 Oct 1;73:89-122.
- [129] Csáji BC. Approximation with artificial neural networks. *Faculty of Sciences, Eötvös Loránd University, Hungary*. 2001 Jun;24(48):7.
- [130] Claesen M, De Moor B. Hyperparameter search in machine learning. *arXiv preprint arXiv:1502.02127*. 2015 Feb 7.

- [131] Brown MS, Arnold CB. Fundamentals of laser-material interaction and application to multiscale surface modification. In *Laser precision microfabrication 2010* (pp. 91-120). Springer, Berlin, Heidelberg.
- [132] Subasi L, Diboine J, Gunaydin A, Tuzemen C, Ozaner OC, Martin R. Water jet guided laser microdrilling of aerospace alloys: Correlation of material properties to process time and quality. *Journal of Laser Applications*. 2021 Feb 22;33(1):012015.
- [133] Lauer B, Jäggi B, Neuenschwander B. Influence of the pulse duration onto the material removal rate and machining quality for different types of steel. *Physics Procedia*. 2014 Jan 1;56:963-72.
- [134] Subasi L, Gokler MI, Yaman U. Multi objective optimization of water Jet guided laser micro drilling on Inconel 718 using Taguchi method. *Procedia CIRP*. 2020 Jan 1;94:505-10.
- [135] Subasi L, Gokler MI, Yaman U. A process modeling approach for micro drilling of aerospace alloys with a waterjet guided laser system. *Optics & Laser Technology*. 2022 Apr 1;148:107682.
- [136] Chapman PW. *Sensor Selection Guide: Optimizing Manufacturing and Processes*. ISA; 2006
- [137] Dornfeld D, Lee DE. *Sensors for precision manufacturing*. Springer US; 2008.
- [138] Fischer B, Rohringer W, Panzer N, Hecker S. Acoustic Process Control for Laser Material Processing: Optical microphone as a novel “ear” for industrial manufacturing. *Laser Technik Journal*. 2017 Nov;14(5):21-5.
- [139] Prietoa C, Fernandez R, Gonzaleza C, Dieza M, Ariasa J, Sommerhuber R, Lückingb F. In situ process monitoring by optical microphone for crack detection in Laser Metal Deposition applications. In *11th CIRP Conference on Photonic Technologies [LANE 2020]* 2020.
- [140] Gutknecht K, Cloots M, Sommerhuber R, Wegener K. Mutual comparison of acoustic, pyrometric and thermographic laser powder bed fusion monitoring. *Materials & Design*. 2021 Nov 15;210:110036.
- [141] Pan Y, Cai T, Ma F, Qiu L, Cui L. Self-resonating frequency and cavitation noise of organ-pipe water jet. In *FIV Conference 2018* Apr 15.
- [142] Del Grosso VA, Mader CW. Speed of sound in pure water. *the Journal of the Acoustical Society of America*. 1972 Nov;52(5B):1442-6.
- [143] Stournaras A, Chrysosolouris G. On acoustic emissions in percussion laser drilling. *The International Journal of Advanced Manufacturing Technology*. 2010 Jan;46(5):611-20.
- [144] Fischer B. Optical microphone hears ultrasound. *Nature Photonics*. 2016 Jun;10(6):356-8.
- [145] Bass HE, Sutherland LC, Zuckerwar AJ. Atmospheric absorption of sound: Update. *The Journal of the Acoustical Society of America*. 1990 Oct;88(4):2019-21.
- [146] Peng, C. *Acousto-optical Process Control for Laser Ablation and Laser Welding*. Bachelor Thesis, University Ravensburg-Weingarten, 2019.

- [147] Subasi L, Gokler MI, Yaman U. Real-Time Measurement of Laser Beam Characteristics for a Waterjet Guided Laser Machine. *Int J Adv Manuf Technol*. 2022 Aug 3.

APPENDICES

A. Nominal Compositions of the Alloys

In order to predict drilling time for a material, workpiece material properties should be known. The properties are closely related with the chemical compositions of the materials. The nominal compositions of some of the most commonly used nickel-based aerospace alloys are given in Table A.1.

Table A.1 Nominal Compositions of the Alloys

Element	Inconel 625	Inconel 718	Rene 41	CMSX-4
Al	0.20	0.50	1.50	5.60
C	0.05	0.08	0.06	-
Co	0.50	1.00	11.00	9.00
Cr	21.50	19.00	19.00	6.50
Cu	-	0.30	0.25	-
Fe	2.50	16.70	2.50	-
Hf	-	-	-	0.10
Mn	0.25	0.35	0.05	-
Mo	9.00	3.10	9.75	0.60
Nb	3.65	5.20	-	-
Ni	Bal.	52.50	Bal.	Bal.
Si	0.25	0.35	0.25	-
Re	-	-	-	3.00
Ta	-	-	-	6.50
Ti	0.20	0.90	3.15	1.00
W	-	-	-	6.00

B. Python Code for Image Processing

The Python code shown below automatically calculates the effective cutting length and the average power in the water jet by taking a screenshot from the camera and making the necessary calculations. The code is devised as part of the work presented in Chapter 7 for the purpose of real-time measurement of the laser beam characteristics with image processing. The developed code can be seen in Table B.1. A screenshot from the working code is shown in Figure B.1.

Table B.1 Python code for image processing

```
# Import necessary libraries
import tkinter as tk
import pyautogui
from skimage import io
from skimage.util import img_as_uint
import numpy as np

# Create a canvas
root= tk.Tk()
canvas1 = tk.Canvas(root, width = 600, height = 250)
root.resizable(width=False, height=False)
canvas1.pack()

def takeScreenshot ():
    # Take the screenshot from the camera screen
    myScreenshot = pyautogui.screenshot()
    # Save the screenshot as an image file
    myScreenshot.save(r'screenshot.png')
    # Make the screenshot grayscale
    img = io.imread(r'screenshot.png', as_gray=True)
    # Crop the area of interest
    cropped = img[360:460,20:600]
    # Save the cropped image file
    io.imsave(r'image.png', cropped)
    # Load the image
    photo_image = tk.PhotoImage(file='image.png')
    # Show the image on the canvas
    canvas1.create_image(300, 110, image=photo_image)

    # Convert an image to unsigned integer format, with values in
    # [0, 65535]
    image = img_as_uint(cropped)
    # Transform the image to an array
    x = np.array(image)
```

```

# A new array is made up of the brightest pixels for each
column. This array is used for length measurement.
y = np.max(x, axis=0)
# Variable to count the bright pixels
a = 0
for i in y:
    # This value (10000) represents the threshold value to see
    the visible laser light. The value may change depending on
    the camera setup
    if i > 10000:
        # Count the number of bright pixels, when their value is
        above the threshold
        a = a + 1
# The number of bright pixels are converted to length. The
coefficient may change depending on the camera setup
a = 0.154*a
# The value is rounded
a = round(a,1)
# The value is transformed to a string
a = str(a)
# Show the length value on the previously created canvas
canvas1.create_text(300, 200, fill='red', text='Laser Length =
'+a+' mm')

# A new array is made up of the average brightness of the
cropped area. This array is used for estimating the laser
power
z = np.average(x)
# Brightness is converted into laser power. The coefficient
may change depending on the camera setup
z = 0.0006*z
# The value is rounded
z = round(z,1)
# The value is transformed to a string
z = str(z)
# Show the laser power value on the previously created canvas
canvas1.create_text(300, 220, fill='red', text='Average Power
in Water = '+z+' W')

# Create a button on the canvas to perform the screen capture
myButton = tk.Button(text='Measure', command=takeScreenshot,
bg='green', fg='white', font= 10)
canvas1.create_window(300, 20, window=myButton)

root.mainloop()

```

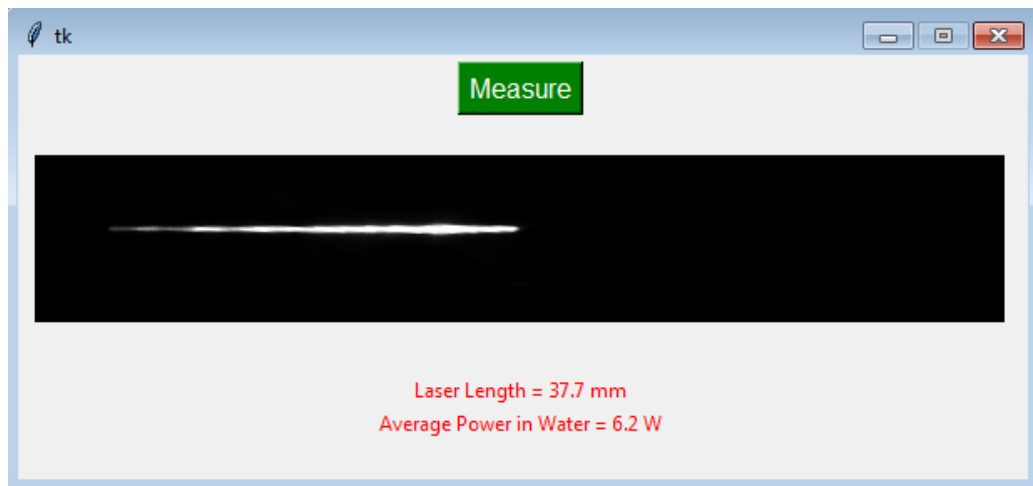


Figure B.1. A screenshot from the working code

CURRICULUM VITAE

Surname, Name: Subaşı, Levent

EDUCATION

Degree	Institution	Year of Graduation
MS	METU Mechanical Engineering	2005
BS	METU Mechanical Engineering	2002
High School	Cankaya M.P. Anatolian High School	1997

WORK EXPERIENCE

Year	Place	Enrollment
2016-Present	Tusas Engine Industries, TEI	Senior Engineer
2015-2016	Aironn Ventilation	Plant Manager
2015-2015	Torun Copper	Machining Supervisor
2013-2015	Polat Machinery	Manufacturing Manager
2006-2013	Tusas Engine Industries, TEI	Process Engineer
2004-2006	Arcelik Dishwasher Plant	Quality&Production Engineer
2001 August	Tusas Aerospace, TAI	Intern Eng. Student
2000 August	Nurol Machinery	Intern Eng. Student

FOREIGN LANGUAGES

Advanced English

PUBLICATIONS

1. Subasi, L., Gokler, M. I., Yaman, U. "A Comprehensive Study on Water Jet Guided Laser Micro Hole Drilling of an Aerospace Alloy", Optics & Laser Technology (2022) (Being revised for publication)
2. Subasi, L., Gokler, M. I., Yaman, U. "Real-Time Measurement of Laser Beam Characteristics for a Waterjet Guided Laser Machine", Int J Adv Manuf Technol (2022) - doi.org/10.1007/s00170-022-09885-8

3. Subasi, L., Gokler, M. I., Yaman, U. "Real-Time Measurement of Laser Beam Characteristics for a Waterjet Guided Laser Machine", 31st International Conference on Flexible Automation and Intelligent Manufacturing, FAIM, Detroit, MI, USA (2022)
4. Subasi, L., Gokler, M. I., Yaman, U. "A process modeling approach for micro drilling of aerospace alloys with a waterjet guided laser system", Optics & Laser Technology, 148, 107682 (2022) - doi.org/10.1016/j.optlastec.2021.107682
5. Subasi, L., Gokler, M. I., Yaman, U. "Multi objective optimization of water Jet guided laser micro drilling on Inconel 718 using Taguchi method", Procedia CIRP 94, 505-510 (2020) - doi.org/10.1016/j.procir.2020.09.172
6. Subasi, L., Gokler, M. I., Yaman, U. "Predicting the Effective Cutting Length of Laser Micro Jet Process Using Machine Learning", International Conference and Exhibition on Digital Transformation and Smart Systems, DTSS, Ankara, Turkey (2019)

PATENTS

1. Subasi, L., "A Real-Time Acoustic Identification System and Method for Jet-Guided Laser Processing Devices", Türk Patent ve Marka Kurumu, Grant Number: 2021-GE-607125, (2021) (Patent Pending)
2. Subasi, L., "A Real-Time Raman Length Measurement System and Method for Jet-Guided Laser Processing Devices", Türk Patent ve Marka Kurumu, Grant Number: 2021-GE-506185, (2021) (Patent Pending)